

ARPA-E Award No: DE-AR0000874

Title: HIGH QUALITY DOPING OF GAN THROUGH TRANSMUTATION PROCESSING

University of Missouri

PI: Jae W. Kwon

Project period: September 2017 – September 2022

Report period: September 2017 – September 2022

Report date: 22 November, 2023

I. Executive Summary

This project led to several outstanding achievements:

- Computational modeling of nuclear reactions, including estimates of the production ratio and doping concentration using TALYS 1.96 based on nuclear reactions in GaN induced by gamma-ray and protons. For photonuclear transmutation doping, simulations proved that Zn/Ge ratio with 40 MeV is higher than the other energies.
- Proton transmutation doping was shown to be a potential nuclear source to fabricate p-type gallium-based semiconductor materials, examined during new irradiations with Oak Ridge National Laboratory and Brookhaven National Laboratory (in 200 MeV H⁻-Linac).
- Patent disclosure to the University of Missouri-Columbia about healing effects in GaN by radiations.
- Zn-doped p-type GaN through photonuclear transmutation doping process.
- The PIs made an oral presentation on the p-type characteristics of Zn-doped GaN at the Materials Research Society Fall meeting in Boston.
- The last irradiation process was in progress in collaboration with Argonne National Laboratory.

II Bulleted list summarizing milestones due:

Milestones DUE Q1FY22

2.7 Doping of mono-isotope GaN

- **[Complete to collaborator: Due 12/19/21]** ^{69}GaN material was shipped to UCSB in August 2021. UCSB worked to fabricate ^{69}GaN .

3.3.3 Q11: Consistent p-type behavior

- **[Complete: Due 6/19/21]** The p-type characteristics of Zn-doped GaN were successfully confirmed.

M5.2.1 Q13: Creation of doped layers for FinFET Devices

- **[Completion extent unknown: Due 12/19/21]** Due to the lack of time and funding, the fabrication of FinFET devices on the irradiated GaN is pending.

Correspondence with collaborators at UCSB and MIT could provide continuation of this effort.

Total project milestones and progress are shown sequentially in the following pages.

Photonuclear transmutation doping concentrations

It is very important to characterize the transmutation doping concentration in terms of the nuclear transmutation doping methods. There are some ways to characterize the concentration. On the assumption that one of the n- or p-type dopants are overwhelmingly great than the other, the concentration can be calculated from measured C-V curves. Through the C-V measurements, the overall carrier concentration can be characterized although metal depositions are inevitable and even can affect the final results. That is both a big advantage and a big disadvantage of this method at the same time. It is necessary to check the total charge carrier concentration, but there is no way to check the individual doping concentration if various dopants are in the samples. Instead of the C-V measurements, the SIMS (Secondary Ion-Mass Spectroscopy) technique is used more often to characterize the doping concentration. SIMS technique also has some limitations because the dopants are measured from secondary ions extracted during the sputtering process. Therefore, the error increases when the mass of the target ions increases due to mass interferences. For the measurements of the isotopes of Zn, Ga, and Ge, the error is $\pm 10\%$. Additionally, the SIMS technique measures the total doping concentration on the samples. In a case like nuclear transmutation doping methods, it needs to distinguish the concentration present in the sample and the concentration produced during the transmutation doping processes. The way to only measure the transmutation doping concentration is gamma-ray spectroscopy counting. Transmutation doping is the transformation of native atoms in the target into dopants. During the transformation process, most atoms become radioactive for a moment and decay for a stable state. Theoretically, the gamma-ray spectroscopy technique is counting the radioactivity before all the radioactivity decays. By using the mechanism, the following equations were used to calculate the transmutation doping concentration through gamma-ray spectroscopy:

$$N_{T[\text{Ga-67}]} = \frac{C_{\text{Ga-67}} \lambda_{\text{Ga-67}} [t_i + \frac{1}{\lambda_{\text{Ga-67}}} e^{(-\lambda_{\text{Ga-67}} \times t_i)}]}{E_e \varepsilon_e [1 - e^{(-\lambda_{\text{Ga-67}} \times t_i)}] e^{(-\lambda_{\text{Ga-67}} \times t_{\text{decay}})} [1 - e^{(-\lambda_{\text{Ga-67}} \times t_i)}]}$$

where $C_{\text{Ga-67}}$ is the measured count rate for ^{67}Ga at 93, 185, and 300 KeV peak [cps], $\lambda_{\text{Ga-67}}$ is a decay constant of ^{67}Ga from the end of irradiation to infinity [$1.253 \times 10^{-7} \text{ s}^{-1}$], t_i is irradiation time [s], E_e is a branching ratio of ^{67}Ga at the 93, 185, and 300 KeV peak (0.39, 0.21, and 0.17), ε_e is energy-dependent detector efficiency at the 93, 185, and 300 KeV peak, t_{decay} is decay time from the end of irradiation to gamma-ray spectroscopy measurement [s], t_i is live time, or counting time, the chosen period to count the sample [s].

^{67}Ga in GaN has a fairly long lifetime and is produced sufficiently during the PNTD process. The ^{67}Zn concentration ($N_{T[\text{Ga-67}]}$) transmuted by ^{67}Ga is calculated by the equation above.

This technique also has some limitations. Some radioactive isotopes have too short a half-lifetime to measure the radioactivity. In other words, it is possible to count the radioactivity with a not-too-short-half-lifetime although all the transmutation doping concentrations can be measured theoretically.

To overcome the barriers, we devised a technique that combines the advantages of the SIMS and gamma-ray spectroscopy counting in collaboration with Argonne National Laboratory (ANL). By using the technique, the improved transmutation doping concentrations are determined by four steps:

1. Through secondary ion-mass spectroscopy (SIMS), the concentration of ^{68}Zn is measured
2. The concentration of ^{67}Ga is measured through gamma-ray spectroscopy counting

3. Based on the measured beam profile and energy spectrum, the simulations were programmed and performed.
4. The concentrations calculated by the simulations are corrected by the concentrations measured from the SIMS.

Since the γ counting for other radionuclide isotopes was not accurate since radioactive isotopes are produced very little and/or have short half-lives except for ^{67}Ga , the result of SIMS measurements was used as a correction factor. The concentration becomes much more accurate. The concentration estimation of the other isotopes is calculated by the following equation:

$$N_{T[\text{Ga a}]} = PR_{\text{Ga}} A_{\text{Ga}} \rho_{\text{GaN}} \left[t_i + \frac{1}{\lambda_{\text{Ga-70}}} \{ e^{(-\lambda_{\text{Ga}} \times t_i)} - 1 \} \right] R_{\text{Ga-67}}$$

where PR_{Ga} is the production rate of Ga calculated by the product of the energy-integrated γ flux and cross-section for the production of isotopes, A_{Ga} is Ga atoms per GaN mass, ρ_{GaN} is a GaN density [6.15 g/cm³], t_i is irradiation time [s], λ_{Ga} is a decay constant of produced isotopes from the end of irradiation to infinity, and $R_{\text{Ga-67}}$ is the ratio of measured ^{67}Ga activity to estimated ^{67}Ga activity through the production rate of ^{67}Ga and accounts for γ spectroscopy counting corrections.

The production concentrations of zinc (Zn), germanium (Ge), and carbon (C) were calculated more accurately through Monte Carlo-based transport simulation program (FLUKA), nuclear data library (TENDL-2019), and gamma-ray spectroscopy counting. N-type Hyper Pure Germanium detector from ORTEC Model GMX30P4-76 with a useful energy range from 3keV to 10 MeV was used. This technique enhanced the accuracy to measure the transmutation doping concentration, having an error of $\pm 3\%$.

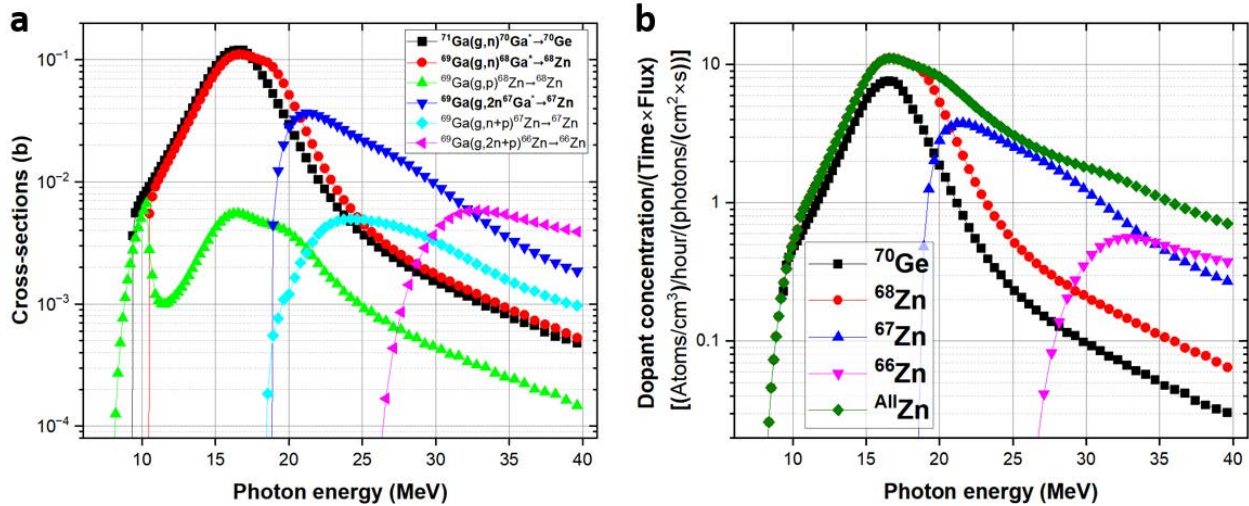


Fig. 1 Dopant production depends on the photon energy. **a** Cross-sections and nuclear reactions of ^{69}Ga and ^{71}Ga induced photons. Nuclear reactions accounting for more than 1% of the total doping concentration generated by the PNTD process were included. **b** Doping concentration per time of ^{70}Ge and Zn isotopes. All Zn is the sum of the concentration per time of ^{68}Zn , ^{67}Zn , and ^{66}Zn .

Fig. 1a shows the cross-sections and photon-induced nuclear reactions of ^{69}Ga and ^{71}Ga depending on the energy. Fig. 1b shows Ge and Zn isotopes have the largest cross-sections

around 16 MeV, but their ratio is almost the same. After 16.5 MeV, the cross-sections of Ge production drastically reduce. The ratio of Zn/Ge steadily increases as the photon energy increases, but the total cross-sections of Zn production are also significantly reduced, requiring longer irradiation and a higher power beam for suitable doping concentration. It needs an appropriate balance among the better ratio of Zn/Ge, Zn production, and experimental conditions.

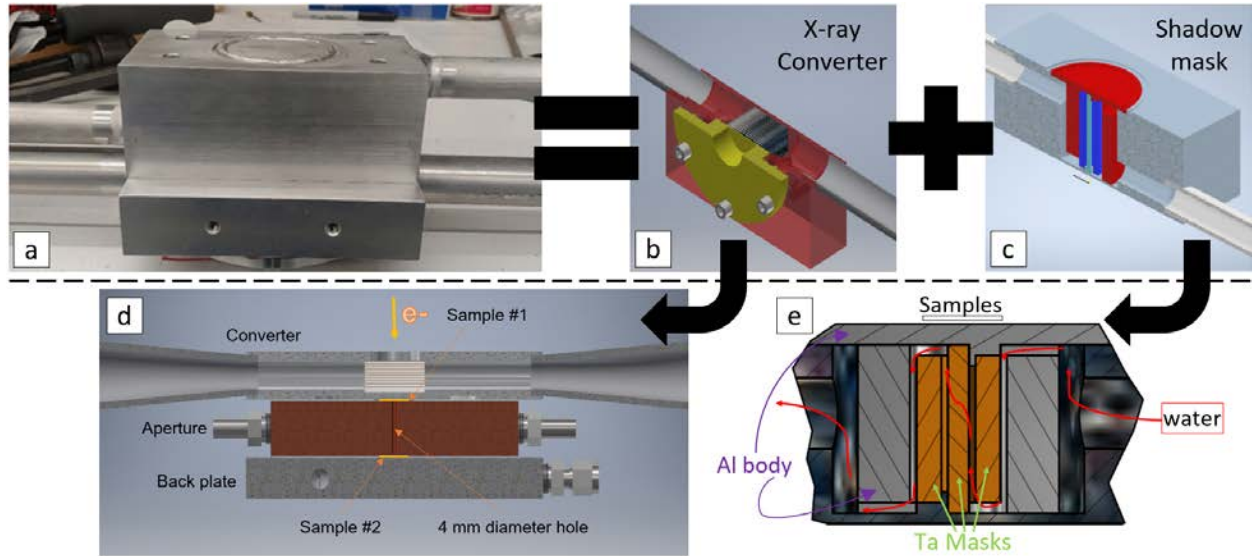


Fig. 2. Schematic diagrams of the experimental setup. **a** Image of combined full assembly. **b** Geometry of a high-power x-ray converter. **c** Geometry of a shadow mask. **d** Composition of the converter. **e** Composition of the mask

The photonuclear reaction can be driven by particle accelerators in a two-step process. First, primary particles are converted into photons via the bremsstrahlung process, and then the photons interact with the target nucleus, driving the desired nuclear reactions. Electrons are mainly used as the primary particles to trigger the photonuclear reaction. In collaborating with ANL, an electron linear accelerator in the low-energy accelerator facility was utilized. Furthermore, an x-ray converter for high-power photonuclear irradiations and a shadow mask for selective doping were customized and fabricated, as shown in Fig. 2. The x-ray converter was made of high-Z materials, Tantalum (Ta) and Molybdenum, to maximize bremsstrahlung photon production and power density. The shadow mask was made of Ta with a thickness of 5cm and had a ring shape. The outer diameter, inner diameter, and ring gap are 7 mm, 3 mm, and 2 mm, respectively. In the irradiation setup, 40 MeV is the ideal beam energy, having a satisfactory balance between the Zn production rate and Zn/Ge ratio.

Based on the technique that combines the advantages of SIMS and gamma-ray spectroscopy counting, the transmutation doping concentration was characterized. Through simulations modeled by gamma-ray spectroscopy counting, a more accurate transmutation doping concentration for Zn and Ge isotopes was determined first. SIMS measurements show similar transmutation doping concentrations and also confirm the uniformity of the depth doping profiles, as shown in Fig. 3a.

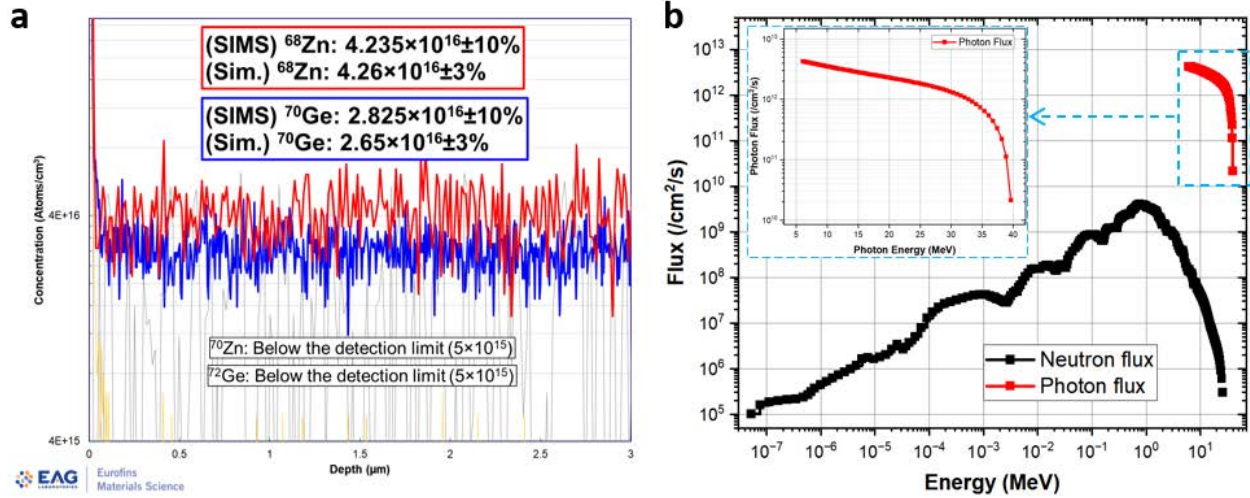


Fig. 3. Transmutation doping. **a** Transmutation doping profiles of Zn and Ge isotopes measured by secondary ion mass spectroscopy (SIMS) and gamma-ray spectroscopy counting with Monte Carlo-based simulations (Sim.). Only ^{68}Zn and ^{70}Ge were measured since other isotopes have concentrations below the detection limit. **b** Flux spectra of photon and neutron in the second photonuclear irradiation. In the left top, photon flux was plotted in a linear scale due to the narrow spectrum. In contrast, neutron flux had a broad and weak spectrum. Based on (a) and (b), more accurate transmutation doping concentrations were calculated in Table 1.

Table 1. Comparison of the first, second, and selective irradiation.

At T = 300K	Photon fluence [photons/ cm^2]	Concentration of ^{68}Zn [atoms/ cm^3]	Concentration of ^{70}Ge [atoms/ cm^3]	$^{68}\text{Zn} - ^{70}\text{Ge}$ concentration [atoms/ cm^3]	Charge carrier concentration [atoms/ cm^3]
1 st irradiation	6.559×10^{19}	5.268×10^{16}	2.579×10^{16}	2.689×10^{16}	Unstable
2 nd irradiation	2.663×10^{20}	2.125×10^{17}	1.043×10^{17}	1.081×10^{17}	+ 8.802×10^{16}
Selective irradiation	3.728×10^{19}	8.743×10^{16}	4.2048×10^{16}	4.538×10^{16}	+ 2.438×10^{16}

P-type electrical characteristics

Undoped GaN samples from MSE Supplies LLC were used in this irradiation and originally had n-type properties. By using C-V measurements with a mercury probe, the initial charge carrier concentration (CCC) of the undoped GaN was measured to be $-2 \times 10^{16}/\text{cm}^3$. The doping concentration compensated from initial CCC and dopants produced by the PNTD process is almost the same, leading to the unreliable CCC measured by Hall effect measurements. Zn isotopes were successfully generated during the first irradiation, but Zn concentration in GaN samples of the first irradiation had insufficient Zn concentration to show p-type properties. For solid p-type characterization, second irradiation was performed at the same beam energy (40 MeV) with higher fluence and achieved a compensated dopant concentration of a positive $10^{17}/\text{cm}^3$. Through the hall effect measurements at 300K, the CCC of the second irradiation GaN samples was measured to be $8.802 \times 10^{16}/\text{cm}^3$ and is reliable considering the initial CCC. The hole mobility and sheet resistance are $2.59 \text{ cm}^2/\text{V}\cdot\text{s}$ and $831.1 \ \Omega/\square$, respectively.

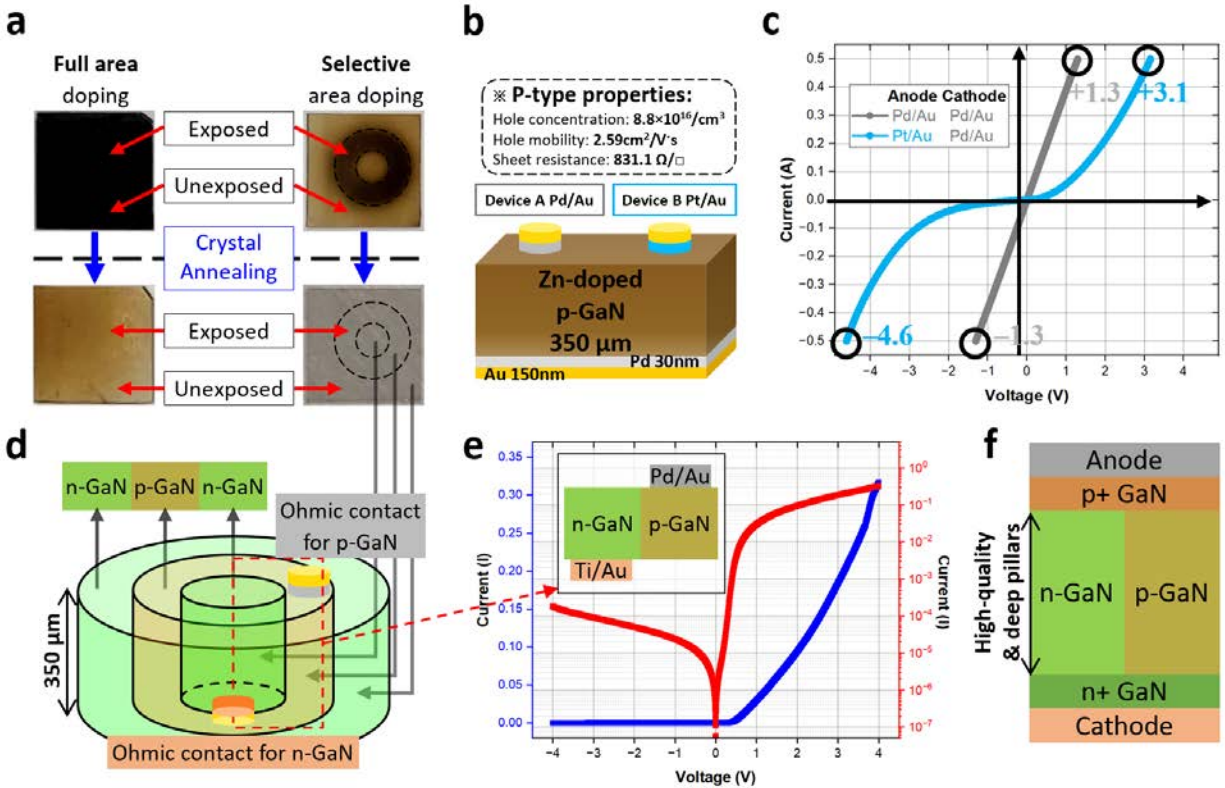


Fig. 4. Schematic diagram of the device and vertical transport measurements with Zn-doped GaN diode. a Optical images of GaN samples irradiated fully or selectively. Damages in exposed areas generated by irradiation are reversed by crystal annealing. **b** Schematic representation of two devices using the second irradiation samples. Pd/Au (30/150 nm) was deposited on both devices as an ohmic contact. Pd/Au (30/150 nm) and Pt/Au (80/40 nm) were deposited on Device A and Device B, respectively. **c** Room-temperature linear-scale I-V curves of the devices in (b). Gray and blue curves present the I-V characteristics of Device A and Device B, respectively. Voltages at ± 0.5 A of the two devices were measured. **d** Schematic representation of PN junction diode using selectively doped samples. Pd/Au (30/150 nm) as an ohmic contact for p-GaN was deposited on the top side of selectively Zn-doped p-GaN. Ti/Au (30/150 nm) as an ohmic contact for n-GaN was deposited on the bottom side of the inside n-GaN. **e** Room-temperature I-V curves of the PN junction diode of (d). **f** conceivable structure of a super junction GaN utilizing selective PNTD process.

Figure 4b shows the 3D cross-sectional image of two representative metal-semiconductor junction diodes deposited by two contacts: Pd/Au is one of the ohmic contacts for p-type GaN. Pt/Au is also one of the ohmic contacts for p-type GaN although the contact resistance of Pt/Au is larger than that of Pd/Au and a well-known Schottky contact for n-type GaN. Device A deposited on both sides by Pd/Au shows very straight linear I-V curves, confirming the p-type properties of Zn-doped GaN. In addition, Device B deposited on Anode by Pt/Au supports the p-type characteristics. Pt/Au contact caused the turn-on voltage and voltage at +0.5 A to be larger values and asymmetric I-V characteristics. Due to the role of Schottky contact for electrons in GaN, the electron flow was suppressed at reverse bias voltage. However, the rectification effect for electrons was not good, leading to the fact that the majority carrier in Zn-doped GaN is holes. To confirm the rectification effect of Zn-doped p-type GaN and the feasibility of applications for the two-dimensional electric field, selective photonuclear transmutation doping was performed through high-Z shadow masks. The optical images of GaN in Fig. 4a clearly shows the

difference between exposed and unexposed area. The elastic scattering of photons dislocating Ga and N atoms could damage the GaN lattice and result in a discoloration of GaN. Only the dark area had no optical and electrical characteristics until the samples were annealed. Comparing the dimension of the shadow masks, the discolored area shows the selective doping ability of the PNTD process. In contrast to fully irradiated GaN, selectively irradiated GaN was lightly doped by weak gamma-ray, resulting in weak irradiation damage. This leads to perfect restoration after the crystal annealing. By using the selectively doped and annealed GaN, the PN junction diode was fabricated, as shown in Fig. 4d. Figure 4e shows the I-V characteristics of the PN junction diode with more than 10^3 rectification of rectification ratio. Interestingly, the rectification effect of the PN junction diode is good although each electrode is very far from the other due to the deep n-/p-pillars ($\sim 350 \mu\text{m}$). We have not only confirmed the p-type characteristics of Zn-doped GaN but also come up with a potential super junction structure as shown in Fig. 4f.

Publications from this Quarter

- J. Kim, A.S. Patapenka, S.D. Chemerisov, and J.W. Kwon, “P-type Gallium Nitride doped by Zinc through Photo-nuclear Transmutation Doping (PNTD) process”, in 2022 MRS Fall meeting & exhibit, Accepted for oral presentation.
- J. Kim, M.D. Frontzek, L. Crow, and J.W. Kwon, “Selective thermal neutron transmutation doping with Gd masks in GaN semiconductors”, *Solid State Electronics*, In print.
- J. Kim, Q. Nguyen, R. Barbera, J. Brockman, J. Gahl, and J.W. Kwon, “Effects of ^{14}C doped by neutron transmutation on n-GaN Schottky barrier diodes”, *Materials Today Communications*, In review.
- J. Kim, B. Raghobhamachar, Y. Liu, M. Dudley, and J.W. Kwon, “Defect curing for GaN through short-time fast neutron irradiation”, *Applied Physics Letters*, In preparation.
- J. Kim, A.S. Patapenka, S.D. Chemerisov, and J.W. Kwon, “Fabrication of p-type GaN doped by Zn through Photonuclear Transmutation doping (PNTD) and selective PNTD process”, *Nature Communications*, In preparation.

Summary of all work in the last three quarters is provided sequentially in the following pages.

II Bulleted list summarizing milestones due:

Milestones DUE Q1FY22

2.7 Doping of mono-isotope GaN

- **[In Progress: Due 12/19/21]** ^{69}GaN material was shipped to UCSB in August 2021. UCSB is working on fabricating ^{69}GaN .

3.3.3 Q11: Consistent p-type behavior

- **[In Progress: Due 6/19/21]** We are working on increasing the irradiation time for more Zn production.

5.4 Determine irradiation parameters for carbon behavior study

- **[In progress: Due 3/19/21]** Recently, Low doped GaN and GaN with epilayers from manufacture 3 were taken out from the reactors. The characteristics of the new irradiated samples will be studied very soon.

M5.2.1 Q13: Creation of doped layers for FinFET Devices

- **[In Progress: Due 12/19/21]** Shadow mask to shield gamma-ray was finally fabricated this quarter. In the new irradiation, the masks were used and showed a clear difference. After confirming the p-type properties of Zn-doped GaN, we will develop FinFET devices on the GaN in collaboration with the Massachusetts Institute of Technology.

M5.6.1 Q10: Characterization of C doping in GaN

- **[In Progress: Due 3/19/21]** The ^{14}C behavior is indirectly studied by various measurements such as the analysis of electrical characteristics.

III Major risks to future milestones

A) ISSUES, RISKS, AND MITIGATION

The main issue this quarter came from setting up new irradiations with protons. It is not easy to find the appropriate nuclear research reactors and start new collaborations with them due to insufficient time and funding. The cryostat of our DLTS equipment has some problems, so it was shipped to the manufacturer for repair. This leads to a setback for studying carbon behavior and defects induced by neutrons.

B) CHANGES IN APPROACH

We are verifying the irradiation conditions through the simulations clearly and thinking of applying for new funding opportunities with the results.

Simulation of nuclear reactions for photonuclear transmutation doping

In collaboration with Argonne National Laboratory (ANL), the production of zinc (Zn), germanium (Ge), and carbon (C) was calculated by FLUKA (FLUKtuierende KAskade: fully integrated Monte Carlo simulation package for the interaction and transport of particles and nuclei in matter. In the simulation, the simulation condition is as follows:

- Beam energy: 15, 25, and 40 MeV
- Beam power: 3 kW
- Beam FWHM: 0.6 cm
- Thickness and number of Ta plates in X-ray converter: 9 and 0.25 mm
- Irradiation time: 160 hours
- Sample density: 6.15 g/cm³ (GaN) and 6.44 g/cm³ (Ga₂O₃)
- Sample size (WDH): 0.65 cm × 0.65 cm × 0.033 cm

Figure 1 shows the diagram of the irradiation model and the cross-sections of ⁶⁹Ga & ⁷¹Ga induced by gamma-ray. In the simulations, the irradiation model consists of an x-ray converter, water cooling channels with 0.5 mm of thickness, Ta plates with 0.25 mm, and GaN or Ga₂O₃ samples. In the middle of the model, there are 9 Ta plates and 10 water cooling channels. The production concentration of Zn, Ge, and C was tabulated in Table 1.

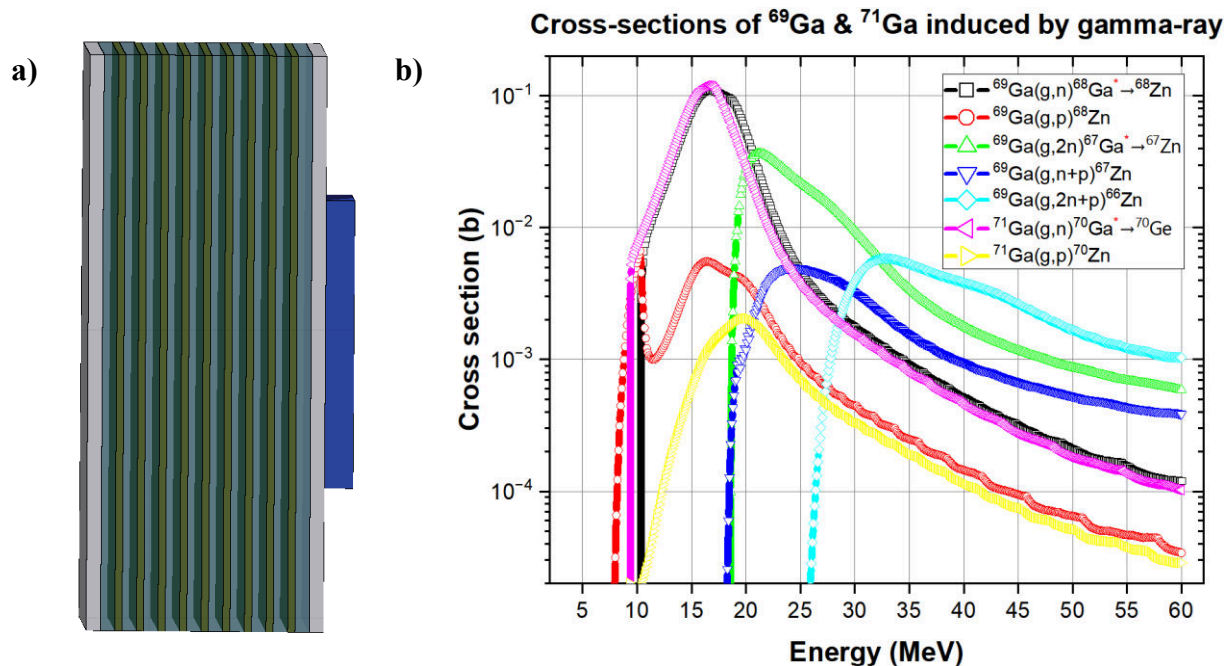


Figure 1. a) Diagram of the irradiation model. From left to right, silver is the body of the X-ray converter, light blue is the water cooling channel (0.5 mm), dark green is a Ta plate (0.25 mm), and blue is GaN or Ga₂O₃ samples. b) Cross-sections of ⁶⁹Ga & ⁷¹Ga induced by gamma-ray.

Table 1. Production concentration and Zn/Ge ratio at 15, 20, and 40 MeV

GaN:					Ga2O3 :					
		Volume [cm ³]	0.0139425			Volume [cm ³]	0.0139425			
40 MeV	Zn production	1.77E+15	1.27E+17	p-type dopant	40 MeV	Zn production	1.65E+15	1.19E+17	p-type dopant	
	Ge production	9.13E+14	6.55E+16	n-type dopant		Ge production	8.54E+14	6.12E+16	n-type dopant	
	C production	2.35E+14	1.68E+16	p-type dopant		N production	3.54E+14	2.54E+16	p-type dopant	
	C production w/o 14C	1.30E+14	9.30E+15	p-type dopant		C production	1.24E+14	8.90E+15		
	14C production	1.05E+14	7.53E+15	p-type dopant		14C production	1.19E+13	8.54E+14		
	Zn/Ge ratio	1.942661043				Zn/Ge ratio	1.935850568			
20 MeV	Zn production	2.89E+14	2.07E+16	p-type dopant	20 MeV	Zn production	2.70E+14	1.94E+16	p-type dopant	
	Ge production	2.14E+14	1.53E+16	n-type dopant		Ge production	2.01E+14	1.44E+16	n-type dopant	
	C production	4.93E+13	3.54E+15	p-type dopant		N production	7.41E+12	5.31E+14	p-type dopant	
	C production w/o 14C	9.82E+12	7.04E+14	p-type dopant		C production	8.78E+12	6.30E+14		
	14C production	3.95E+13	2.83E+15	p-type dopant		14C production	0.00E+00	0.00E+00		
	Zn/Ge ratio	1.35E+00				Zn/Ge ratio	1.35E+00			
15 MeV	Zn production	2.46E+15	1.76E+17	p-type dopant	15 MeV	Zn production	3.21E+13	2.30E+15	p-type dopant	
	Ge production	2.16E+15	1.55E+17	n-type dopant		Ge production	2.82E+13	2.02E+15	n-type dopant	
	C production	1.56E+13	1.12E+15	p-type dopant		N production	4.18E+11	3.00E+13	p-type dopant	
	C production w/o 14C	2.58E+12	1.85E+14	p-type dopant		C production	2.10E+12	1.51E+14		
	14C production	1.30E+13	9.32E+14	p-type dopant		14C production	0.00E+00	0.00E+00		
	Zn/Ge ratio	1.135323383				Zn/Ge ratio	1.137588652			

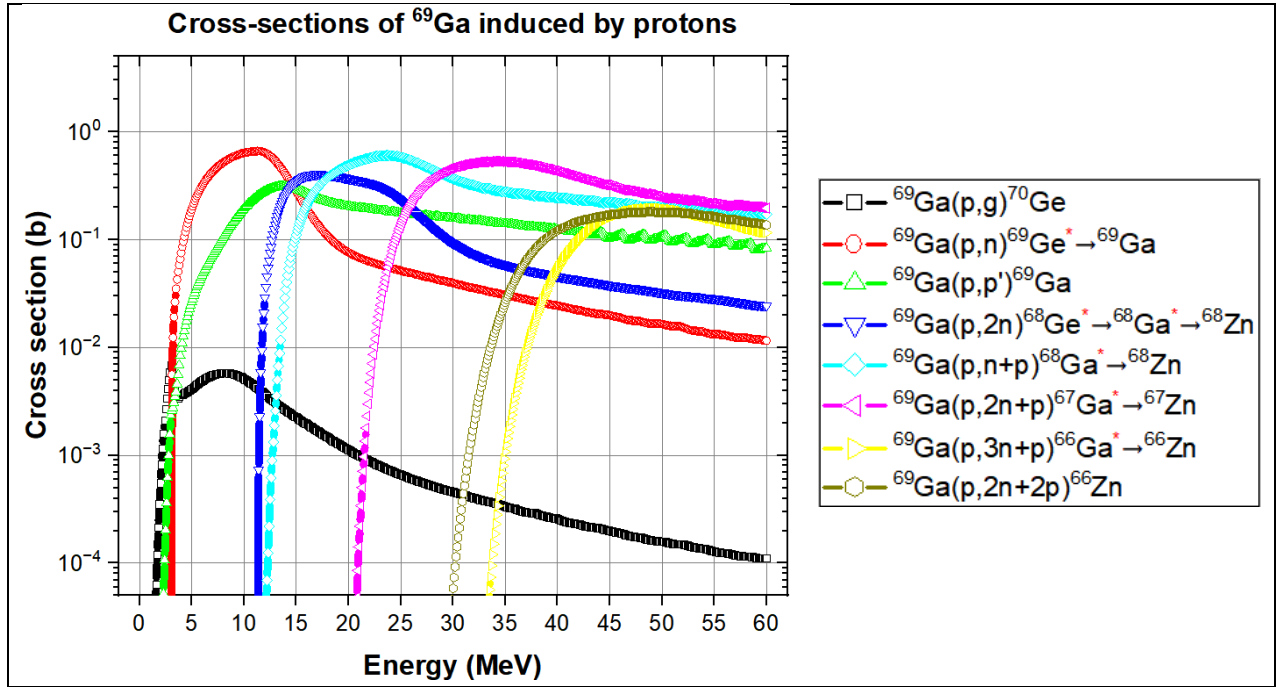
The cross-sections of Ga have a peak around 15 ~ 20 MeV, especially for the production of ⁷⁰Ge and ⁶⁸Zn. As more Zn is generated, more Ge is also generated. As a result, the Zn/Ge ratio is poor. At the high energy (40 MeV), the cross-sections for the production ⁷⁰Ge and ⁶⁸Zn significantly decrease, but the cross-sections of other Zn production increase. So, the Zn/Ge ratio improves and is better than low energy.

Simulation of nuclear reactions for proton transmutation doping

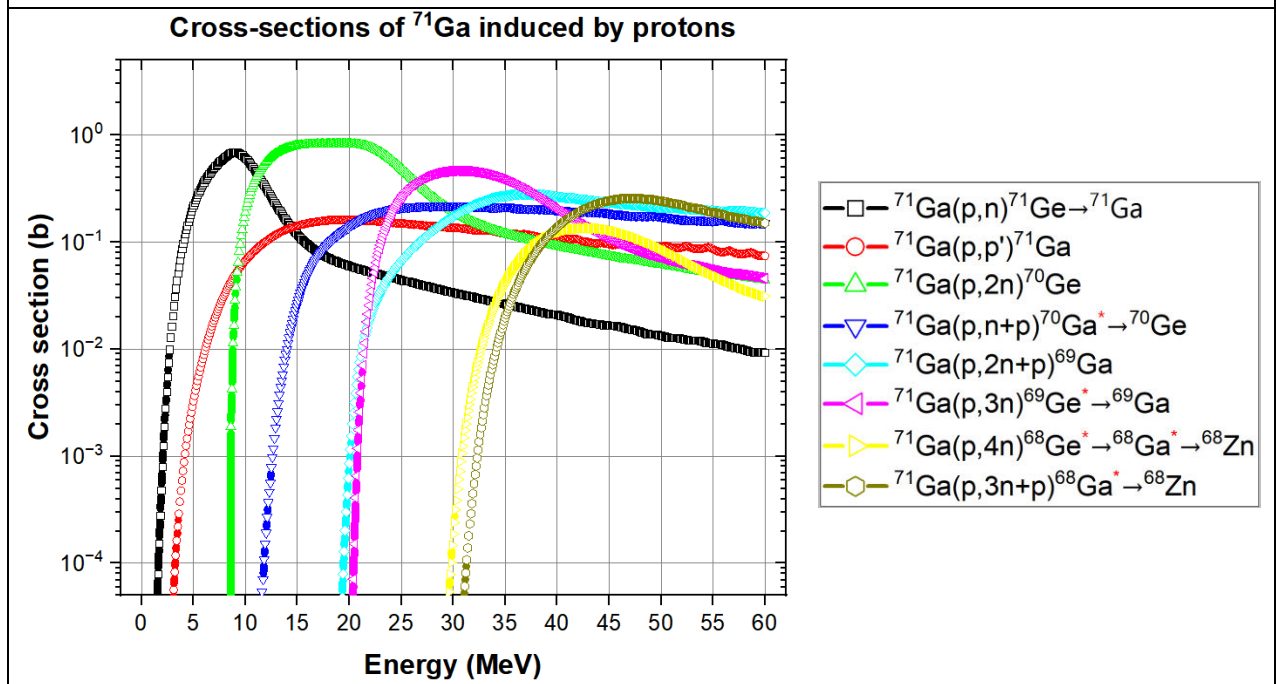
We have tried to find a new p-type dopant in GaN through the neutron transmutation doping (NTD) process and photonuclear transmutation doping (PNTD) process. Theoretically, it is impossible to generate more p-type dopants than n-type dopants through the NTD. The reactions for the Ge, a well-known n-type dopant in GaN, production have very high cross-sections for neutrons. Experimentally, it was demonstrated that Ge is the largest by-product. Carbon, especially carbon-14, was considered a p-type dopant although it is a radioactive material. Unfortunately, it is also very difficult to produce more carbon than Ge. Instead of the NTD, we tried the PNTD process for p-type GaN and focused on Zn production, which is believed to be a candidate for a p-type dopant. Nicely, we successfully produced more Zn than Ge and have been demonstrating the p-type properties of Zn-doped GaN. The PNTD is a good technique for Zn production although Ge is also produced a lot always. ⁶⁹GaN can be a good solution, but it is costly and requires some time.

We think proton transmutation doping is another interesting nuclear source to fabricate p-type gallium-based semiconductor materials. Using TALYS 1.96, we checked the possibility of the

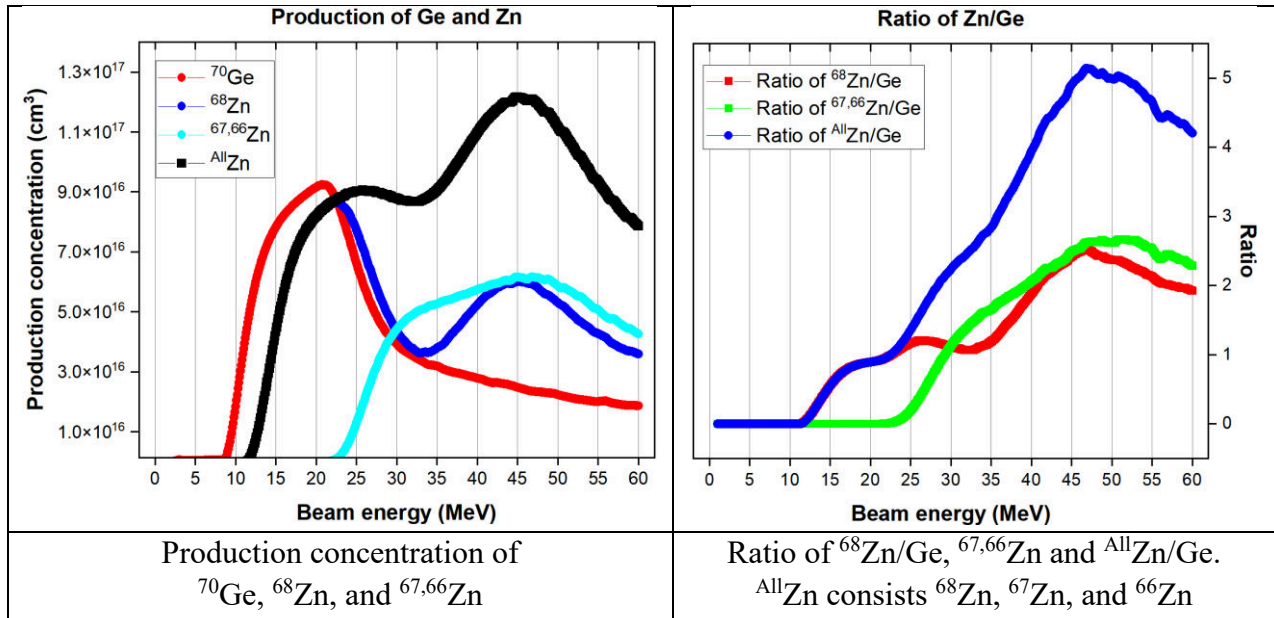
new technique for Zn production and a higher Zn/Ge ratio. Cross-sections and by-products after proton irradiations were estimated at the various energies and shown in Figure 2.



Cross-sections of ^{69}Ga induced by protons and daughters generated by the reactions



Cross-sections of ^{71}Ga induced by protons and daughters generated by the reactions



* Reactions induced by other sources except for proton were ignored.

The cross-sections of Ga induced by protons are much higher than that induced by gamma-ray, and even more reactions contribute to Zn production (same reactions occur during the PTND, but the reactions rarely occur and can be negligible). Around 45 MeV, the ratio of Zn/Ge has a peak value (~5). Assuming that the proton flux is 1×10^{14} protons/cm²/s, the difference in production concentration between Zn and Ge can be 10^{17} /cm³ only after 15 hour irradiation. For the PNTD, we are planning 160 hour irradiation, but the concentration difference would be 6×10^{16} /cm³. The proton transmutation doping is much more efficient and cost-effective. It can be expected that irradiation damage decreases, and fewer defects are generated.

We are working on setting up the new irradiations with Oak Ridge National Laboratory (in Spallation Neutron Source) and Brookhaven National Laboratory (in 200 MeV H⁻-Linac).

High energy radiations in collaboration with MURR

Gallium nitride (GaN) samples, grown by Adroit, were doped by neutron transmutation doping (NTD) process in the position of the Missouri university research reactor (MURR), where the fast neutron flux is high. The GaN samples were irradiated for 5, 25, 75, and 100 hours, so-called GR5, GR25, GR75, and GR100. The properties of the irradiated GaN samples with untreated GaN were studied in terms of optical characteristics, electrical characteristics, and surface topography.

The optical properties were studied through optical images and photoluminescence spectra of untreated and irradiated GaN samples. Fabricating Schottky barrier diodes (SBDs) with the GaN samples, the electrical properties were studied through Schottky barrier height, ideality factor, shunt resistance, and series resistance. The surface properties were studied with two x-ray topography (XRT) techniques: SMBXT (synchrotron monochromatic beam x-ray topography) and SXRCT (synchrotron x-ray rocking curve topography).

Crystal annealing

Conventional, high-temperature annealing is used in semiconductor manufacturing to relieve stress in the crystal; to activate ion-implanted dopants and to reduce structural defects and stress; and to reduce interfacial charge at the interface. However, the high-temperature annealing sometimes causes damage to the semiconductor wafers like material decomposition, leading to poor surface morphology with a high degree of roughness. Especially certain methods like ion implantation require an extremely high temperature (≥ 1200 °C) annealing process. To prevent the material decomposition caused by high temperature, GaN should be thermally annealed under an extremely overpressure nitrogen (N_2) gas ($> 1,000$ bar), as shown on the left of Figure 1.

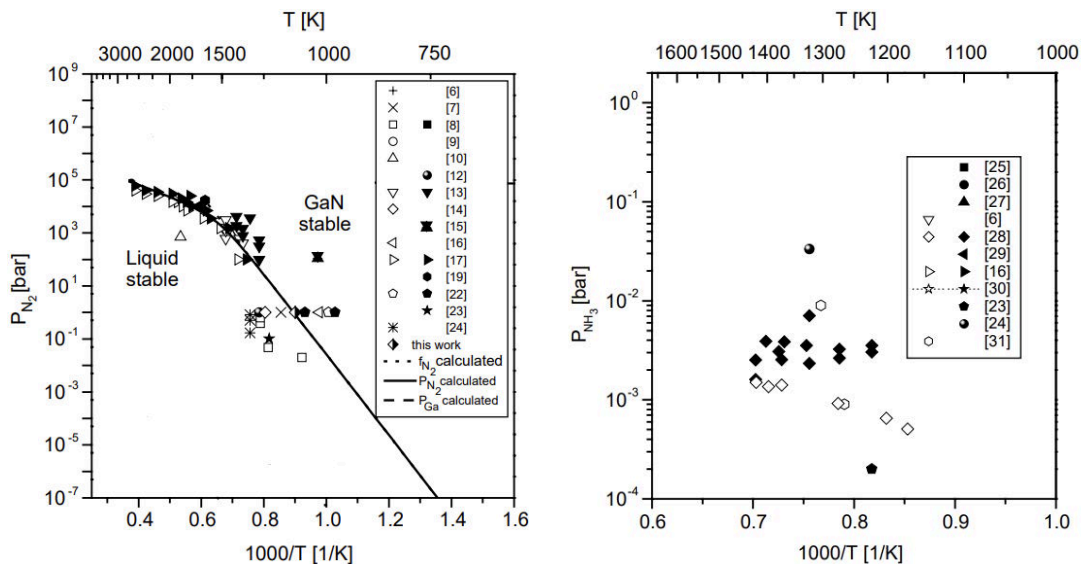


Figure 2. Stability of GaN under N_2 and NH_3 [2]. In the left diagram, the right part of the solid line denotes a stable GaN area, and the left part of the solid line denotes decomposed GaN.

This is very costly inefficient and environmentally destructive. However, the decomposition of GaN occurs at a much lower pressure Ammonia (NH₃) gas according to the right diagram in Figure 1.

All samples irradiated in the position of MURR where the fast neutron is high have no optical and electrical properties after irradiation and need the crystal annealing process in order to heal the damage caused by neutron fluxes. To recover the optical and electrical properties, the GaN samples irradiated in MURR were annealed for 10 minutes at 935 °C (1208.15 K) with NH₃ ambient. The annealing condition was chosen with the reference above and our experiences.

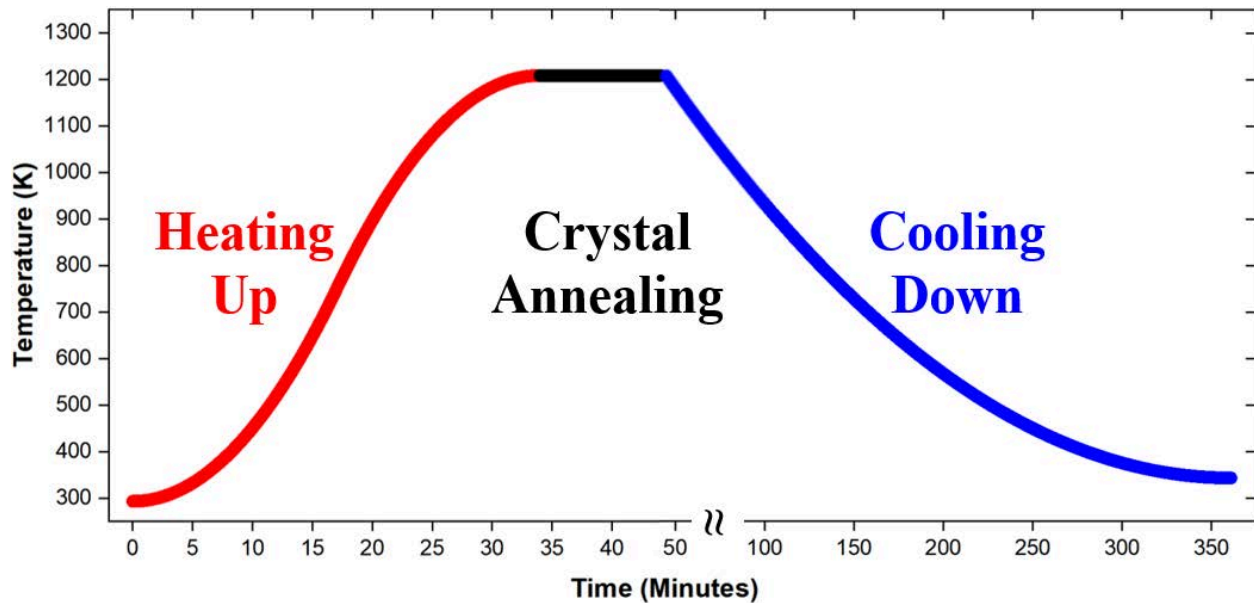


Figure 3. Crystal thermal annealing program, which consists of three steps: Heating up, Crystal annealing, and Cooling down.

Figure 2 shows the annealing program. Before the Heating up section, GaN samples were put in the annealing chamber, vacuuming down until 10 μ bar. In the vacuum state, the chamber was filled with NH₃ ambient. In 34 minutes, the chamber was raised to the desired temperature (935 °C). The GaN samples were annealed for 10 minutes at 935 °C with NH₃ ambient. In the Cooling down step, the chamber was cooled down naturally (for about 5 hours). The optical images of untreated and irradiated GaN before and after crystal thermal annealing are shown in Figure 3 and Figure 4.



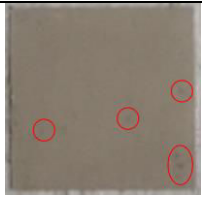
Before annealing		After annealing	
	→		
Untreated GaN		Untreated GaN	Red circles: Annealing defects

Figure 4. Optical images of Untreated GaN, GR5, and GR25 before and after annealing

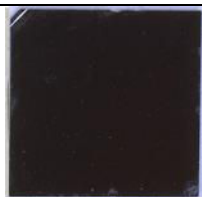


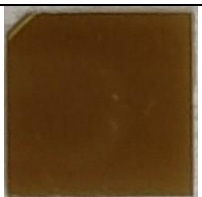
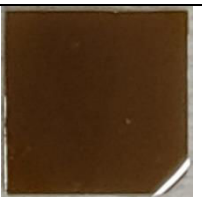
Before annealing		After annealing			
	→				
GR samples		GR5	GR25	GR75	GR100

Figure 5. Optical images of GR5, GR25, GR75, and GR100 before and after annealing

All the samples brightened after annealing. For the untreated GaN sample, some annealing defects were caused by high temperatures, which looked like a burn mark. However, no additional defects on the GR samples were caused by the annealing process. Depending on the irradiation time, the level of color discoloration was different. The sample irradiated for a longer time was darker as the irradiation time increased. We guess the discoloration can result from irradiation damage by the ejected proton generated during the $^{14}\text{N}(n,p)^{14}\text{C}$ reaction and elastic scattering of neutrons dislocating Ga and N atoms.

Interestingly, the appearance of GR5 is almost the same as untreated GaN before annealing and does not have annealing defects unlike untreated GaN after annealing. However, the discoloration of GR25 did not recover discoloration as much as GR5.

Optical characteristics: Photoluminescence (PL) spectroscopy

For the study of optical properties, photoluminescence (PL) measurements were performed on the untreated and irradiated GaN samples. 235 nm excitation laser source was used at room temperature. The optical images irradiated by PL excitation laser sources are shown in Figure 5.

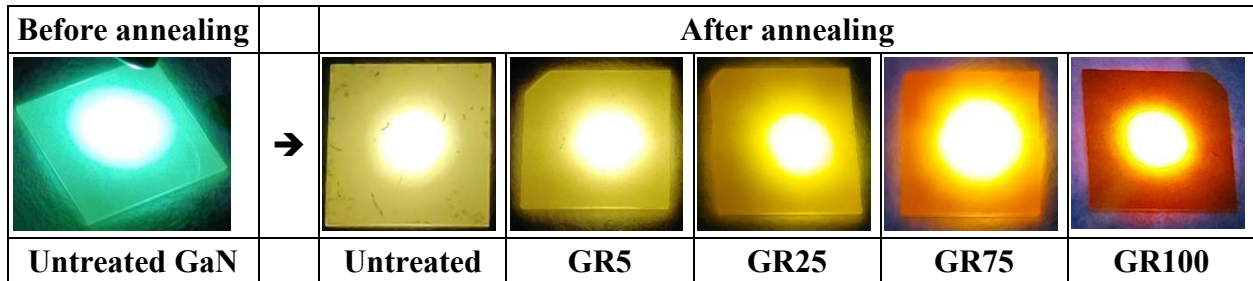


Figure 6. Color of untreated GaN, GR5, GR25, GR75, and GR100 before and after annealing.

For untreated GaN, it took on a green color when exposed to the laser source before annealing and a light-yellow color after annealing with some annealing defects. The annealing defects of the untreated GaN cause weaker intensity and unstable peak position in the PL spectrum, as shown in Figure 6. The defects were not found in the annealed GR samples.

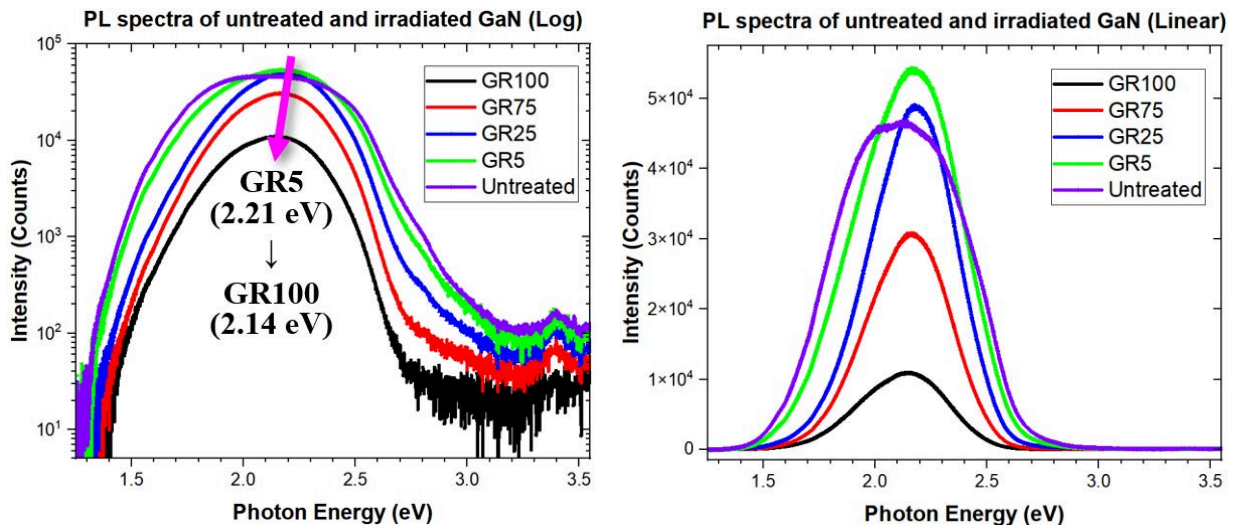


Figure 7. PL spectra of untreated GaN, GR5, GR25, GR75, and GR100 after annealing. The left is log-scale PL spectra, and the right is linear-scale PL spectra.

For GR samples, the intensity decreased as the irradiation time increased. The peak position of GR samples moved from 2.21 eV (GR5) to 2.18 eV (GR25), 2.16 eV (GR75), 2.14 eV (GR100). The reduced intensity and shifted peak position resulted from the increased amount of ^{14}C as the irradiation time increased. Compared with the intensity of the untreated GaN, GR5 and GR25 are better than the untreated one. Assuming that the untreated GaN has no annealing defects, the intensity would be between GR5 and GR25. From here, we have suspected that the GaN quality

could be improved after radiation under appropriate conditions. To get more supportive data, the electrical properties were studied.

Electrical Characteristics: Fabrication of Schottky barrier diodes (SBDs)

For the measurements of the electrical characteristics, we fabricated the Schottky barrier diodes by depositing metals on the untreated and irradiated GaN samples, as shown in Figure 7. Circles with a diameter of 800 μm were deposited by Pt/Au (80 nm/40 nm) on the polished side of samples for Schottky contact. Ti/Au (30 nm/150 nm) were uniformly deposited on the unpolished side of samples for Ohmic contact. To improve the metal contacts, the SBDs were rapidly annealed for 1 minute at 650 $^{\circ}\text{C}$ with N_2 ambient.

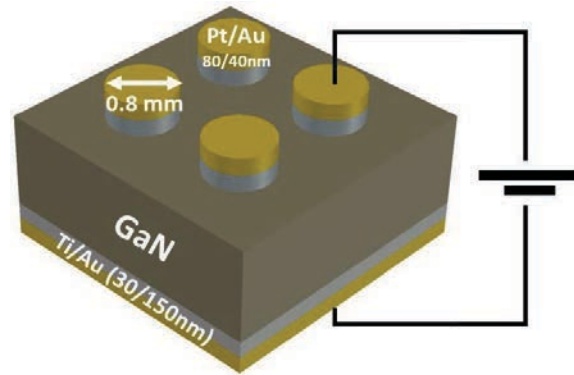


Figure 8. Diagram of metal depositions. The circles deposited by Pt/Au on the polished side are Schottky contact. The bottom deposited by Ti/Au on the unpolished side is Ohmic contact.

Electrical Characteristics: Electrical properties of SBDs by various methods (I-V characteristics, Cheung's method, and C-V characteristics)

The I-V characteristics of untreated, GR5, GR25, GR75, and GR100 were measured on a log scale and linear scale respectively, as shown in Figure 8. In the log scale plot, each sample has a different rectification ratio. As the irradiation time increases, the rectification ratio and leakage current also increase although all GaN samples show nice I-V curves in the linear scale plot.

The current through the SBDs at a forward bias ($V \geq 3kT/q$) follows the thermionic emission theory [3] and can be expressed as:

$$I = I_0 e^{\frac{qV}{nkT}}$$

$$I_0 = AA^{**} T^2 e^{-\frac{q}{kT} \Phi_b}$$

Here, A is the diode area ($5.027 \times 10^{-3} \text{ cm}^2$), A^{**} is the effective Richardson constant ($35 \text{ A}/(\text{cm}^2 \cdot \text{K}^2)$) [4], T is the absolute room temperature (300 K), q is the charge of an electron ($1.6 \times 10^{-19} \text{ C}$), k is the Boltzmann's constant ($1.381 \times 10^{-23} \text{ J/K}$), Φ_b is the measured barrier height, n is the ideality factor.

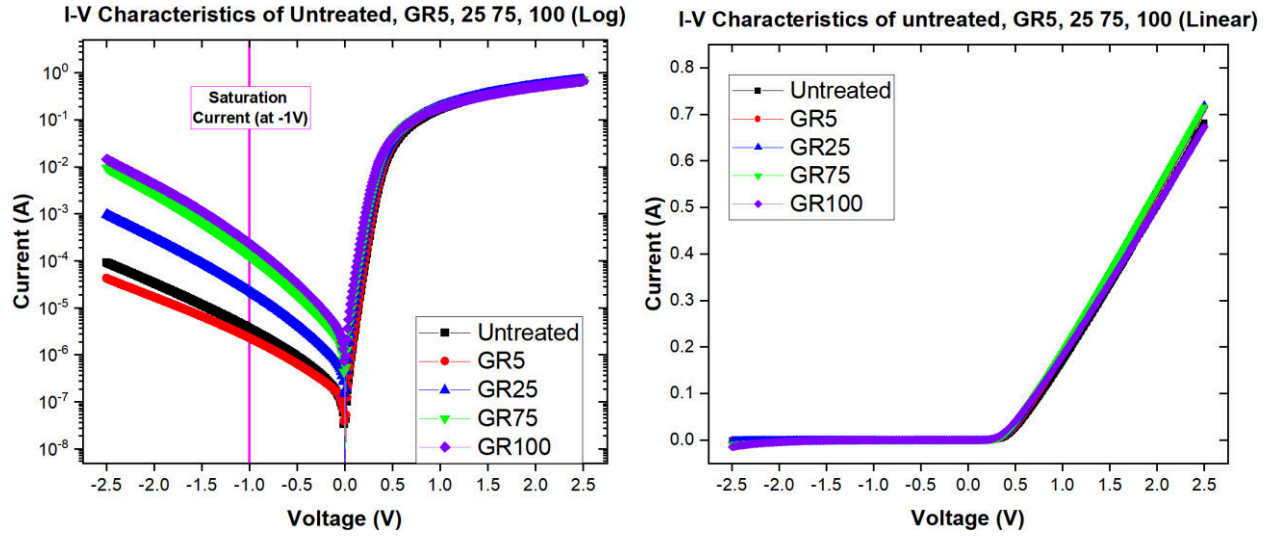


Figure 9. I-V curves of untreated, GR5, GR25, GR75, and GR100. The left is a log scale I-V curve, and the right is a linear scale I-V curve,

The measured ϕ_b and n are calculated by using the reverse leakage current at -1 V. Shunt resistance (R_{sh}) and series resistance (R_s) of each SBD in Figure 9 were estimated from the junction resistance obtained by $R_j = \frac{\partial V}{\partial i}$ from the I-V characteristics.

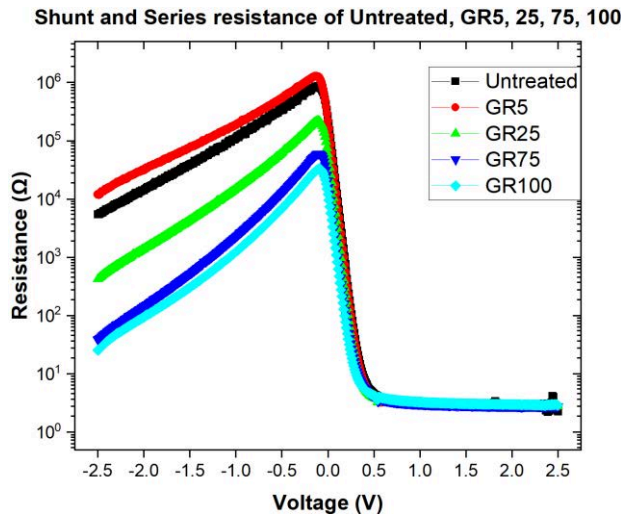


Figure 10. Resistance curves of untreated, GR5, GR25, GR75, and GR100.

The electrical parameters are tabulated in Table I. The ϕ_b , n , R_{sh} , and R_s deteriorated as the irradiation time increased. The long irradiation produced more ^{14}C . It is believed that the ^{14}C acts as acceptors and hole traps, which attributes to the increased trap-assisted recombination and the accumulation of holes causing the increased space charge near the junction. The behavior leads to a decrease in ϕ_b , R_{sh} , and R_s , and an increase in n .

Table II. Electrical parameters measured or calculated by I-V Characteristics, Cheung's Method, and C-V Characteristics.

	I-V Characteristics				Cheung's Method		
	Barrier height ϕ_b [eV]	Ideality factor n	Shunt resistance R_{Sh}	Series resistance R_S	Barrier height ϕ_b [eV]	Ideality factor n	Series resistance R_S
Untreated	0.584	1.496	1.59 M Ω	2.793 Ω	0.646	1.389	3.703 Ω
GR5	0.614	1.466	3.88 M Ω	2.761 Ω	0.669	1.367	6.169 Ω
GR25	0.527	1.744	219 k Ω	2.803 Ω	0.612	1.400	3.567 Ω
GR75	0.488	2.066	65.4 k Ω	2.845 Ω	0.584	1.433	3.383 Ω
GR100	0.474	2.162	37.6 k Ω	2.936 Ω	0.573	1.524	3.293 Ω

Cheung's method was used to determine the ϕ_b , n , and R_S of the SBDs. The electrical parameters obtained by Cheung's method are tabulated in Table I.

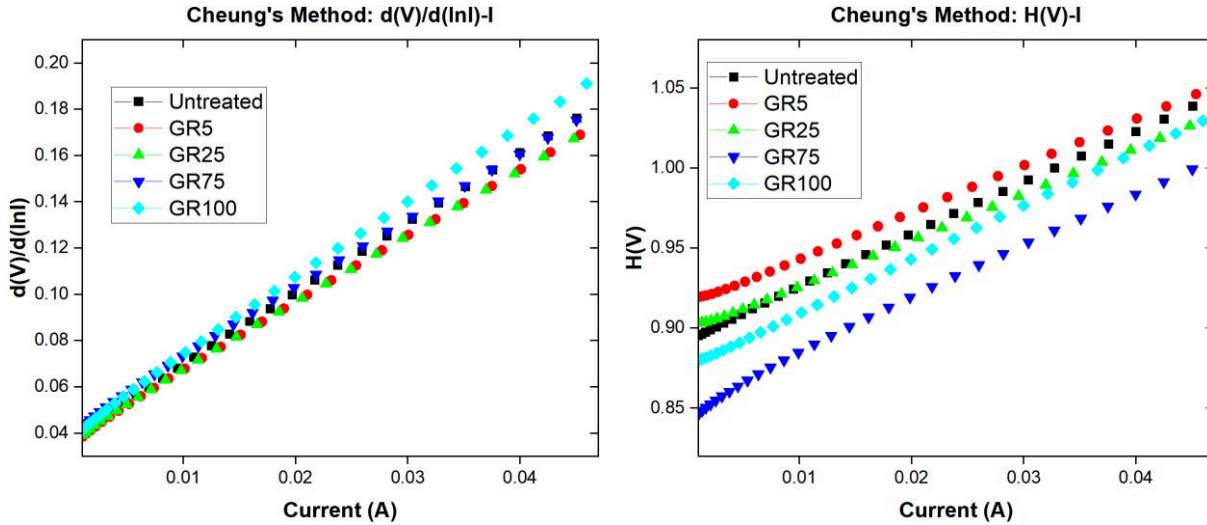


Figure 11. Curves obtained from Cheung's method for untreated GaN, GR5, GR25, GR75, and GR100. The left is a curve of $d(V)/d(\ln I)$ versus I , and the right is a curve of $H(I)$ versus I .

The values of series resistance from both curves are closely matched, implying the consistency and validity of the resistance. The values obtained by Cheung's method are in reasonably good agreement with those obtained by I-V characteristics. The existence of series resistance is considered the main reason. The barrier height and ideality factor obtained by I-V characteristics did not take into account the series resistance. Due to the series resistance, the barrier height and ideality factor calculated by Cheung's functions slightly changed. However, the overall increase or decrease flow of electrical parameters did not change. Like I-V characteristics, the behavior of ^{14}C leads to a higher barrier height and a lower ideality factor. It is speculated that ^{14}C can interfere with the flow of electrons through the recombination of the electron-hole pair.

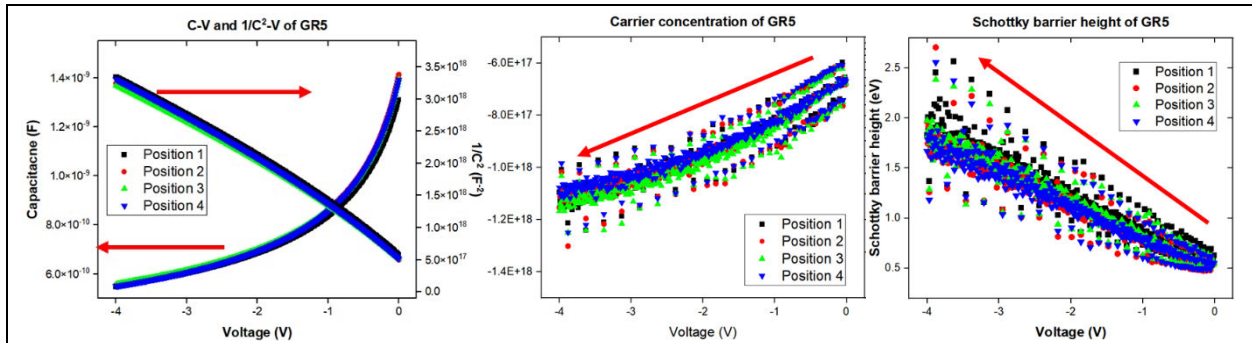
The capacitance-voltage (C-V) characteristics of the SBDs were measured at a frequency of 1 MHz for barrier height and carrier concentration. Figure 4 shows the C-V, $1/C^2$ -V, barrier height (ϕ_b), and carrier concentration (CCC), from which the ϕ_b and CCC are determined based on the following equations [5]:

$$\phi_b = V_{bi} + V_P$$

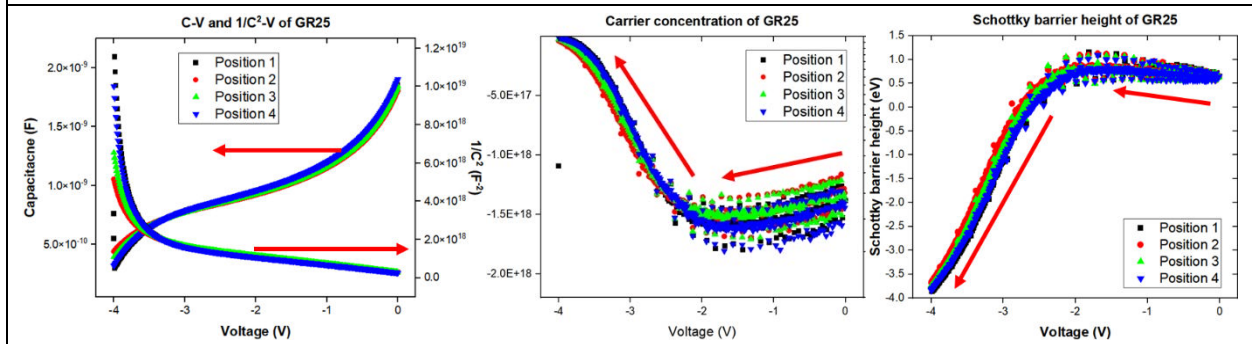
$$\frac{1}{C^2} = \frac{2(V_{bi} - \frac{kT}{q} - V)}{A^2 \times q \times N \times \epsilon_s}$$

$$V_P = \frac{kT}{q} \ln\left(\frac{N_C}{N}\right)$$

where V_{bi} is the built-in potential ($V_{bi} = V_0 + \frac{kT}{q}$), N is the carrier concentration, ϵ_s is the dielectric constant of GaN ($\epsilon_s = 8.9 \epsilon_0 = 7.88 \times 10^{-11} \text{ F} \cdot \text{m}^{-1}$), N_C is the effective conduction band density of states in GaN ($2.3 \times 10^{18} \text{ cm}^{-3}$). V_0 is determined by the x-intercept of the $1/C^2$ versus V curve. Unlike the I-V characteristics and Cheung's method, electrical parameters change with the supplied voltage.



(a) Curves of C-V, $1/C^2$ -V, CCC, and ϕ_b of GR5



(b) Curves of C-V, $1/C^2$ -V, CCC, and ϕ_b of GR25

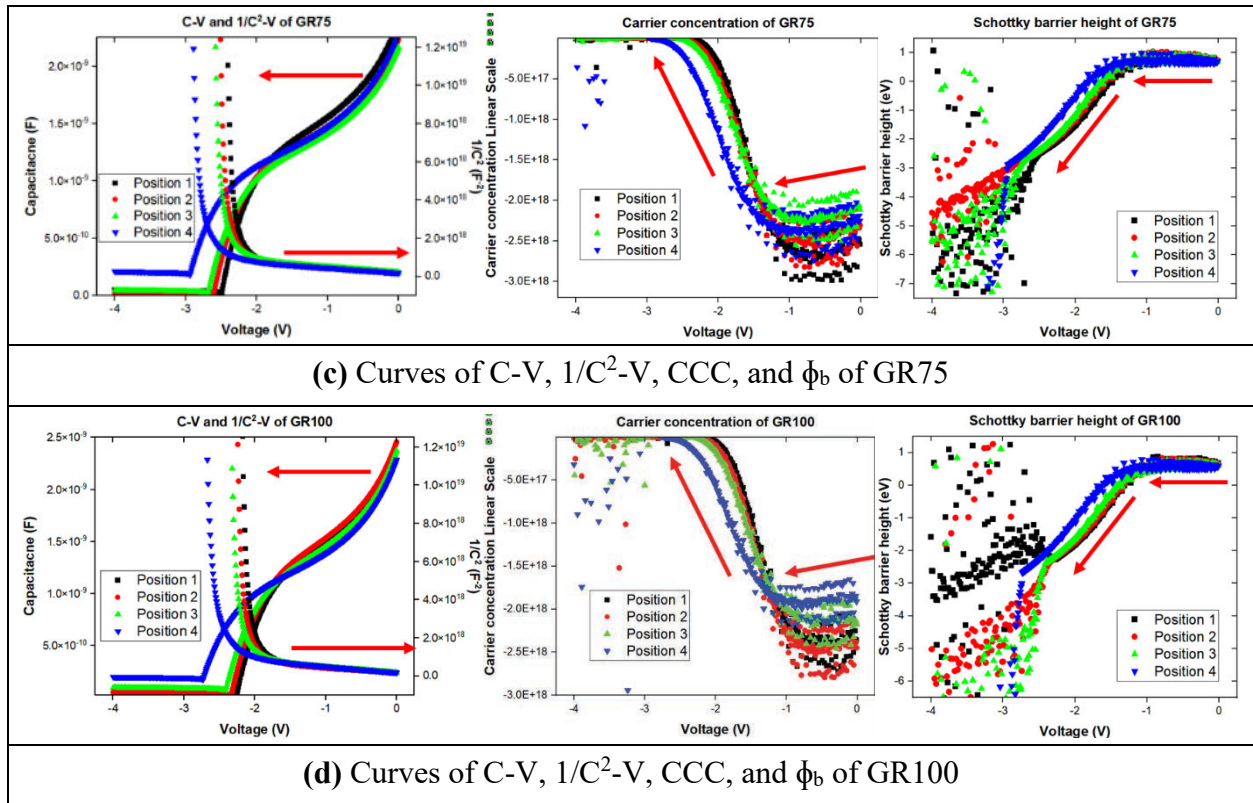


Figure 12. Curves of C-V, $1/C^2$ -V, carrier concentration, and barrier height of GR5, 25, 75, 100.

Except for GR5, the other samples have nonlinear $1/C^2$ -V curves. We guess that ^{14}C acts as an acceptor and cannot be negligible to calculating the doping concentration and barrier height at a high negative voltage. Furthermore, ^{14}C is a radioactive material and is steadily emitting beta particles, especially electrons. The emitted electrons also have a broad energy spectrum. So, it is sure that the behavior of the electrons gets bigger and bigger when the supplied negative voltage increases, resulting in the high leakage current and nonlinear properties of $1/C^2$ -V curves.

If low negative voltage (from 0 to -1V) is only considered, roughly linear $1/C^2$ -V curves can be gained. Within the area, the barrier height values are larger than those calculated by I-V characteristics and Cheung's functions. Some structural, line, or point defects may be produced during neutron irradiation, contributing to lateral inhomogeneity at the metal/semiconductor interface.

X-Ray Topography in collaboration with SBU

To study the crystallographic defects produced during neutron irradiations, X-Ray Topography (XRT) measurements were performed on the GaN with Professor Dudley's team at Stony Brook University (SBU). The two XRT techniques were used: Synchrotron X-Ray Rocking Curve Topography (SXRCT) and Synchrotron Monochromatic Beam X-ray Topography (SMBXT).

Synchrotron X-Ray Rocking Curve Topography (SXRCT)

Lattice strain is a key factor affecting the performance of electronic devices fabricated on GaN. Lattice strain is often observed in GaN after treatments like heat. The lattice strain caused by the residual stress can significantly affect the homogeneity of GaN wafers, leading that the performance of the devices can be potentially influenced. Moreover, stacked topograph with contour flow information, strain, and tilt can be obtained through the SXRCT technique.

To measure each GaN through the SXRCT technique, Si (331) beam conditioner was used with d-spacing close to (0004) spacing in GaN to maximize angular resolution, as shown in Figure 12. The stacked topographs of GR samples from SXRCT are shown in Figure 13 to Figure 16. The strain and tilt of GR samples before and after irradiation is shown in Figure 17. The range of strain and tilt is tabulated in II.

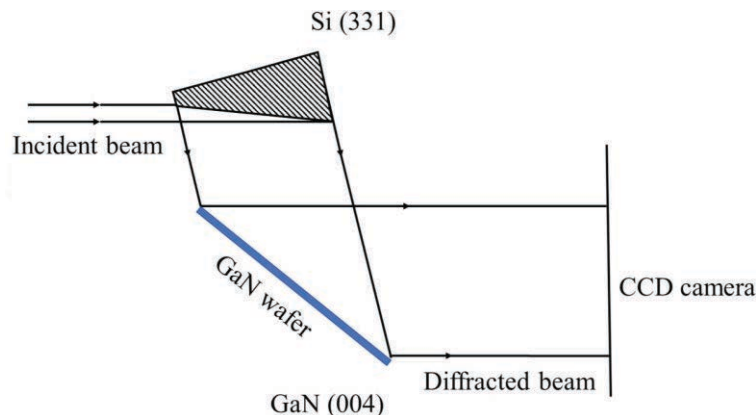


Figure 13. Experimental setup for synchrotron X-ray rocking curve topography [6].

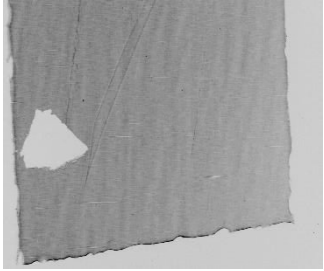
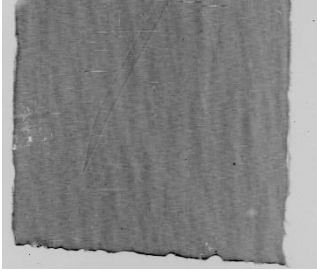
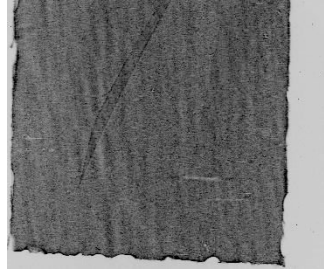
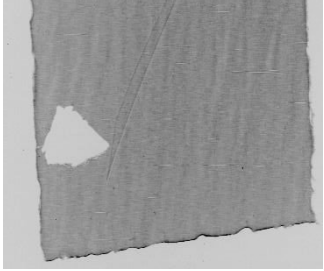
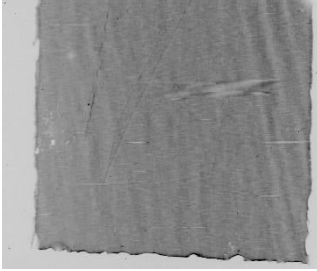
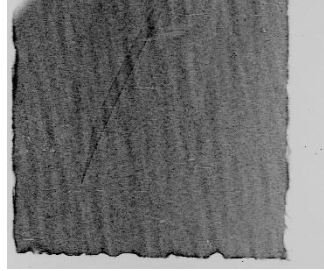
GR5	Before irradiation	After irradiation	After irradiation and annealing
+g geometry			
-g geometry			

Figure 14. Stacked topographs of GR5.

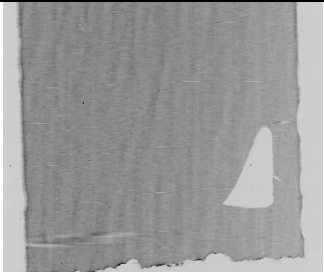

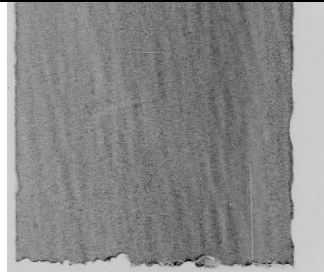
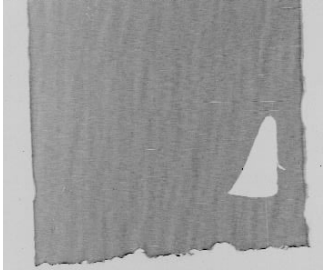


GR25	Before irradiation	After irradiation	After irradiation and annealing
+g geometry			
-g geometry			

Figure 15. Stacked topographs of GR25.


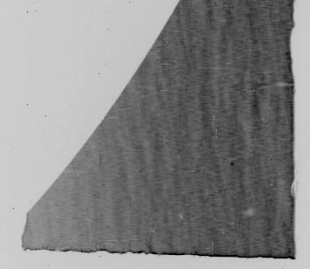
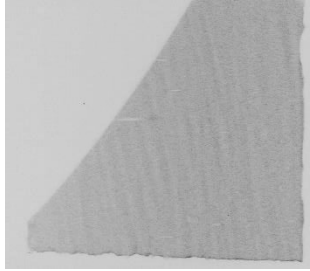
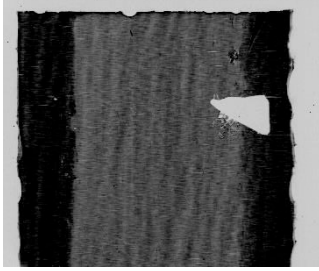
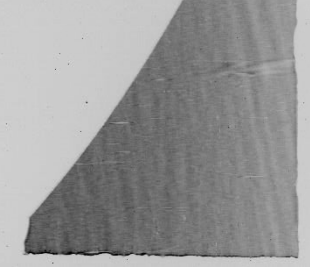
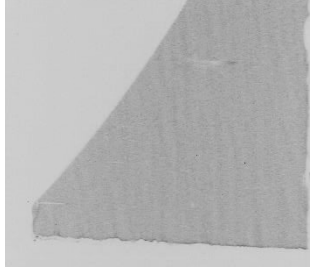
GR75	Before irradiation	After irradiation	After irradiation and annealing
+g geometry			
-g geometry			

Figure 16. Stacked topographs of GR75. GR75 sample was broken during the first measurement – before irradiation.

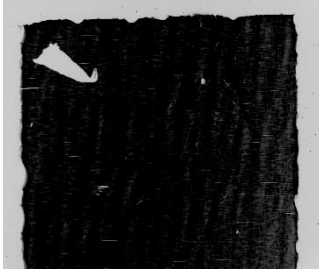
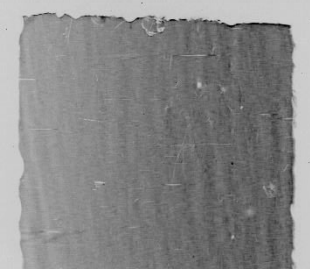
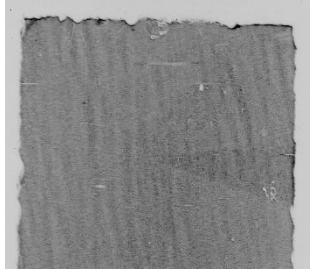
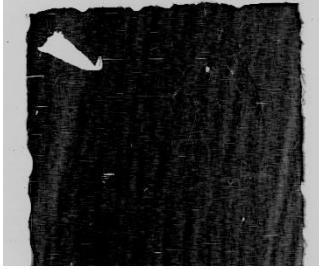
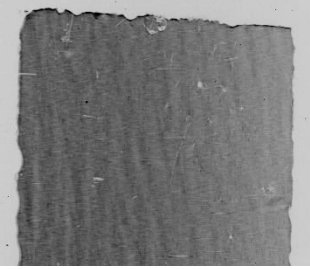
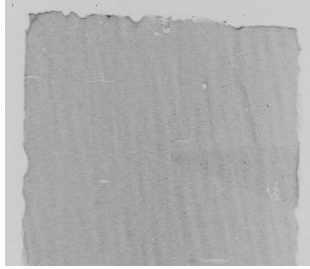
GR100	Before irradiation	After irradiation	After irradiation and annealing
+g geometry			
-g geometry			

Figure 17. Stacked topographs of GR100

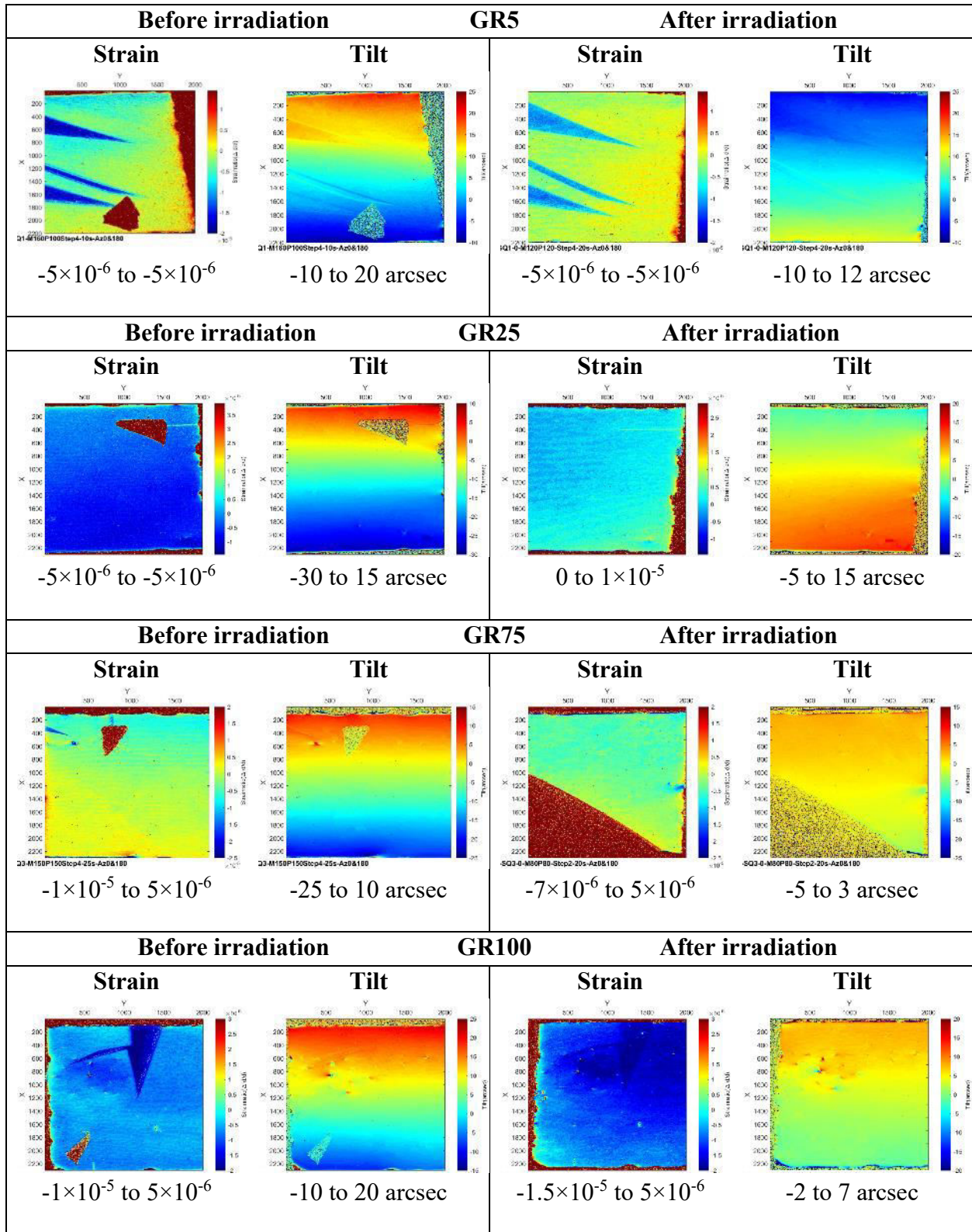


Figure 18. Strain and tilt of GR5, GR25, GR75, and GR100 before and after irradiation. The values of strain and tilt increase when the color changes from blue to red.

Table III. The range of strain and tilt of GR5, GR25, GR75, and GR100 before and after irradiation.

	Strain ratio range [10^{-5}]		Tilt ratio range [arcsec]	
	Before	After	Before	After
GR5	10 (-5 to 5)	10 (-5 to 5)	30 (-10 to 20)	22 (-10 to 12)
GR25	10 (-5 to 5)	10 (0 to 10)	40 (-30 to 10)	20 (-5 to 15)
GR75	15 (-10 to 5)	12 (-7 to 5)	35 (-10 to 25)	8 (-5 to 3)
GR100	15 (-10 to 5)	20 (-15 to 5)	30 (-20 to 10)	9 (-2 to 7)

Strain ranges are not changed by irradiation, but tilt ranges reduce after irradiation. Longer irradiation times give a more significant decrease in tilt ranges. It is guessed that neutrons uniformly hit the GaN from all directions, which helps tilts decrease.

To recover the optical and electrical properties of the irradiated GaN, high temperature annealing (935 °C) was used. Naturally, the material loss occurred and resulted in a rough surface. For that reason, strain and tilt maps were generated for the annealed GR samples.

Synchrotron Monochromatic Beam X-ray Topography (SMBXT)

The SMBXT technique is used to image the dislocations in GaN. In this study, monochromatic beam X-ray is adopted in the grazing incidence geometry, as shown in Figure 18. In grazing-incidence reflection, a very small incident angle is used (typically 2°) and the $11\bar{2}4$ reflection is recorded (39.13° to (0001) surface). The incident beam energy is 9.37 keV. The orientation of $+g$ geometry collected by samples about the $[11\bar{2}4]$ axis is from left to right.

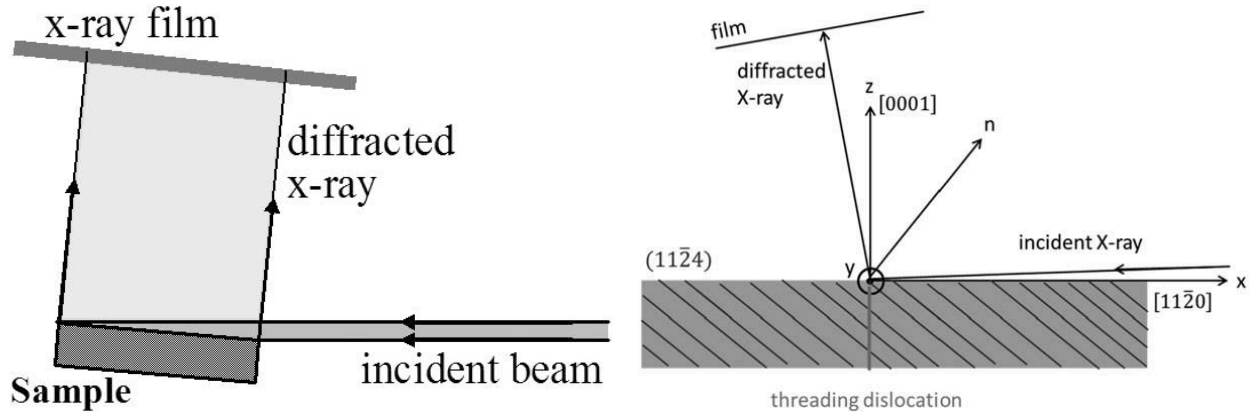


Figure 19. Schematic of the grazing incidence geometry using the synchrotron monochromatic X-ray beam [7].

The topographs and magnified topographs of GaN measured with the SMBXT technique are shown in Figure 19 to Figure 26. Furthermore, defects in GaN were analyzed by categorizing the type of defects: same, disappeared, new, moved, and turned contrast defects. The result from each batch GaN before and after irradiation is tabulated in Table III to Table VI.

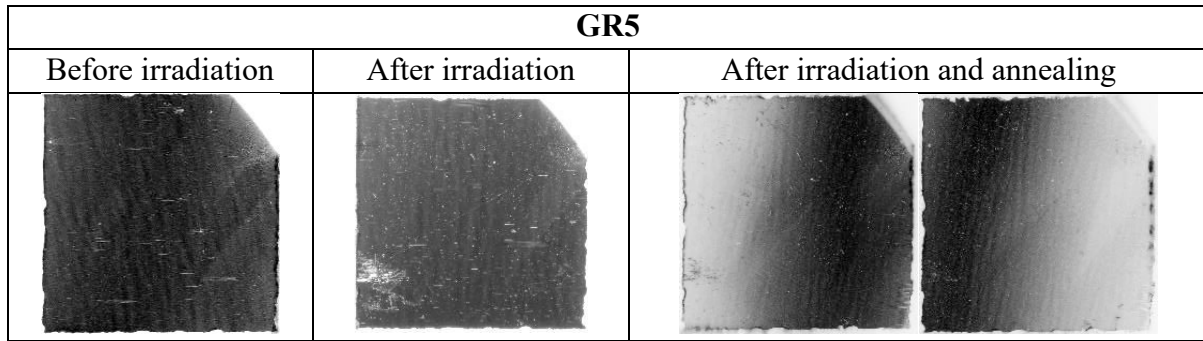


Figure 20. Topographs of GR5: before irradiation, after irradiation, and after irradiation and annealing. Twice measurements were performed to cover the entire surface of GR5 after irradiation and annealing.

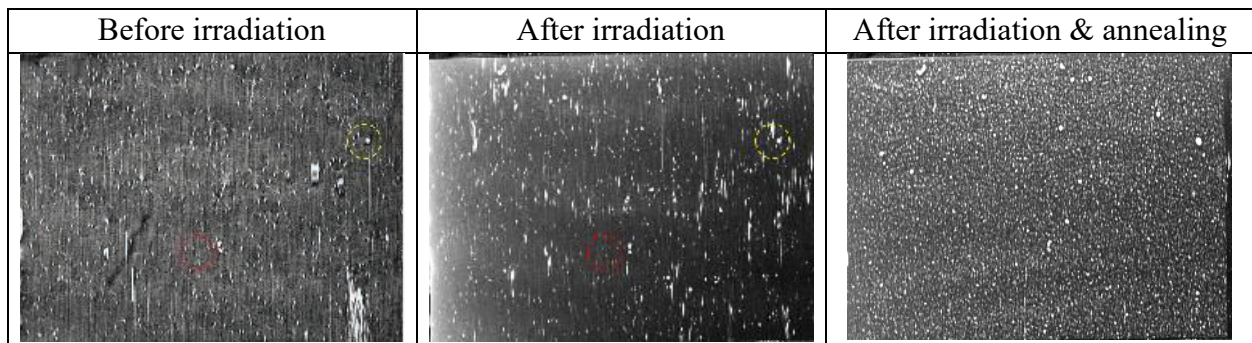


Figure 21. High magnification x-ray grazing incidence topograph of each figure in Figure 19 showing threading dislocation contrasts as bright or dark dot shapes of various dimensions.

Table IV. Defects analysis of GR5 before and after irradiation. The number of same, disappeared, new, moved, and turned contrast dislocations were counted and converted into a percentage.

	Type	Count	Percentage
	Same	450	35.97 %
	Disappeared	371	29.66 %
	New	25	2.00 %
	Moved	37	2.96 %
	Turned contrast	368	29.42 %
	Total	1251	100 %

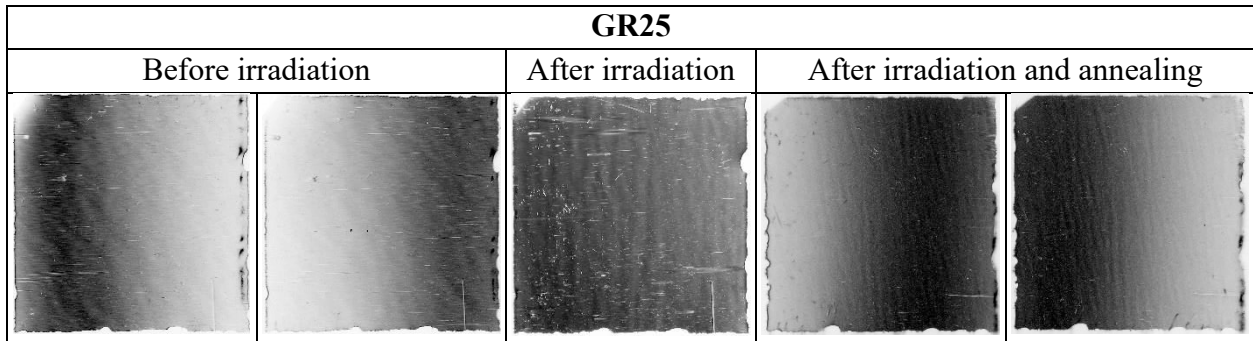


Figure 22. Topographs of GR25: before irradiation, after irradiation, and after irradiation and annealing. Twice measurements were performed each to cover the entire surface of GR25 before irradiation and GR25 after irradiation and annealing.

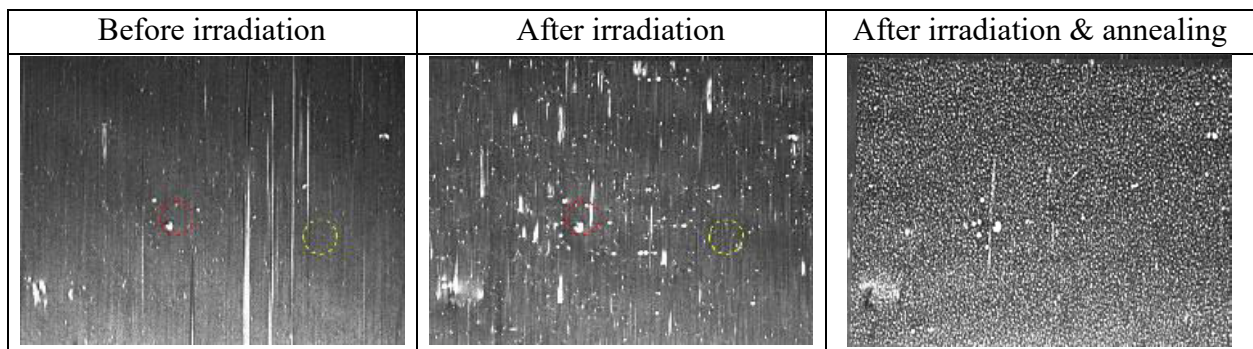
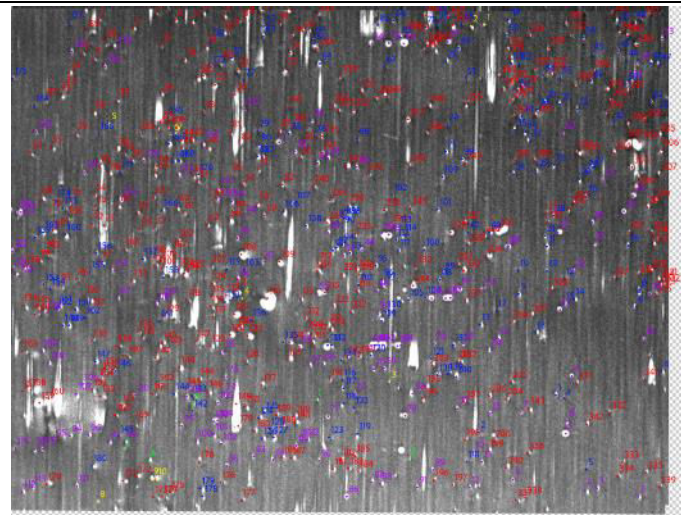


Figure 23. High magnification x-ray grazing incidence topograph of each figure in Figure 21 showing threading dislocation contrasts as bright or dark dot shapes of various dimensions.

Table V. Defects analysis of GR25 before and after irradiation. The number of same, disappeared, new, moved, and turned contrast dislocations were counted and converted into a percentage.

	Type	Count	Percentage
	Same	345	50.81 %
	Disappeared	4	0.59 %
	New	144	21.21 %
	Moved	5	0.74 %
	Turned contrast	181	26.66 %
	Total	679	100 %

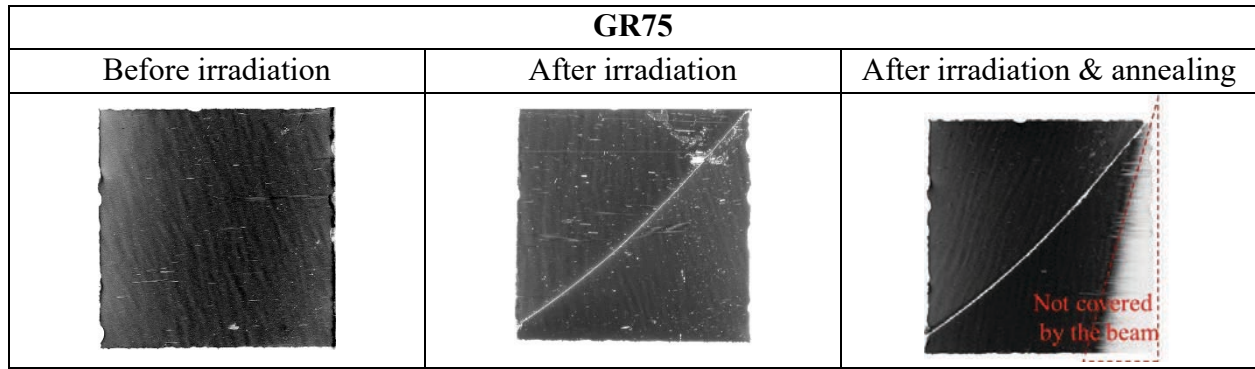


Figure 24. Topographs of GR75: before irradiation, after irradiation, and after irradiation and annealing. GR75 sample was broken during the first measurement – before irradiation.

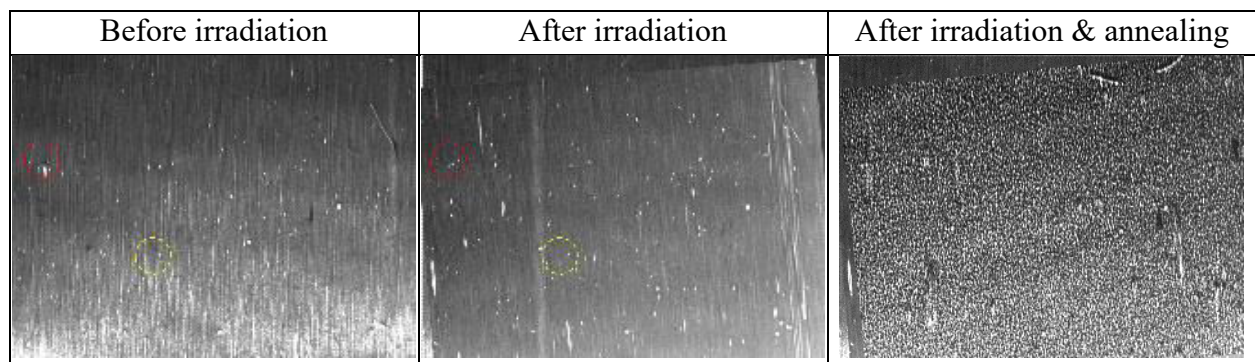
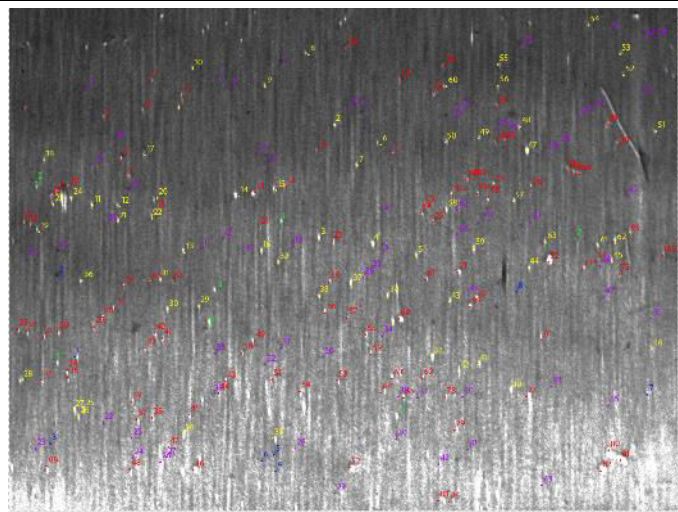


Figure 25. High magnification x-ray grazing incidence topograph of each figure in Figure 23 showing threading dislocation contrasts as bright or dark dot shapes of various dimensions.

Table VI. Defects analysis of GR75 before and after irradiation. The number of same, disappeared, new, moved, and turned contrast dislocations were counted and converted into a percentage.

	Type	Count	Percentage
	Same	103	41.37 %
	Disappeared	63	25.30 %
	New	68	27.30 %
	Moved	7	2.81 %
	Turned contrast	8	3.21 %
	Total	249	100 %

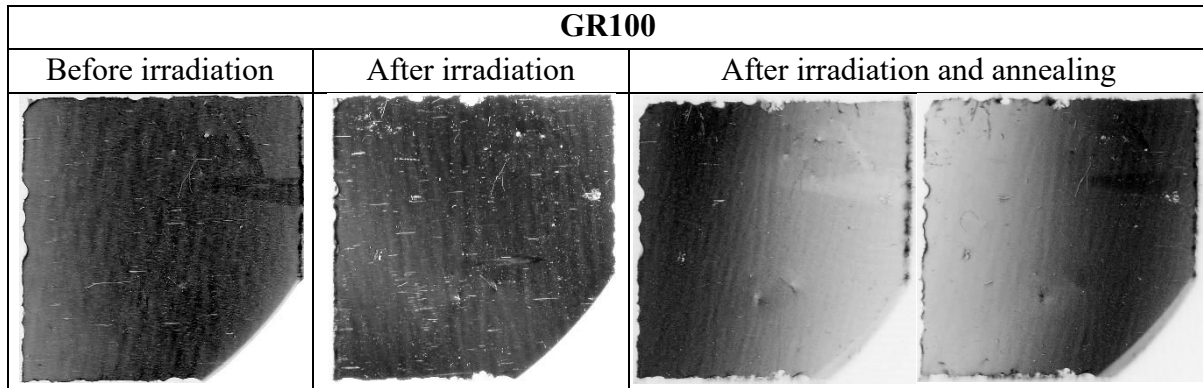


Figure 26. Topographs of GR100: before irradiation, after irradiation, and after irradiation and annealing. Twice measurements were performed to cover the entire surface of GR100 after irradiation and annealing.

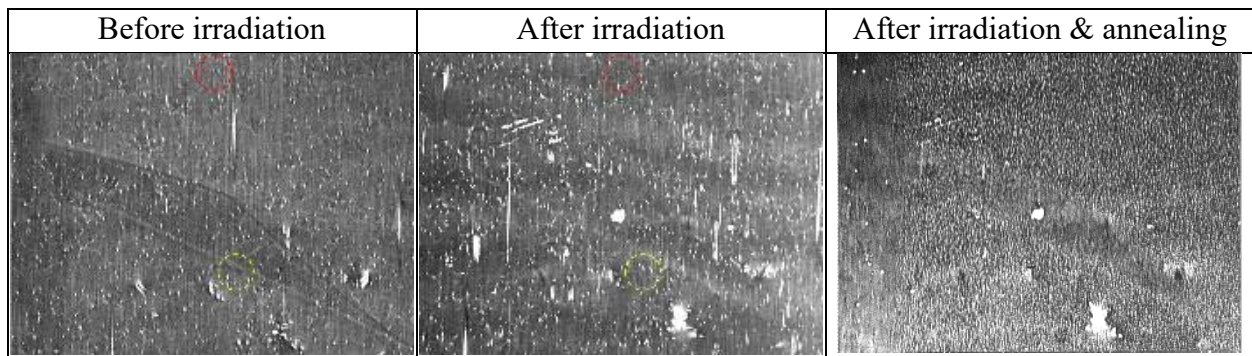
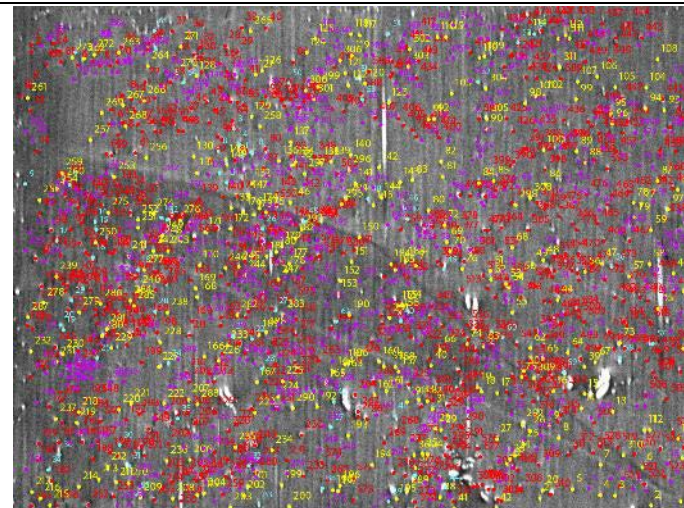


Figure 27. High magnification x-ray grazing incidence topograph of each figure in Figure 25 showing threading dislocation contrasts as bright or dark dot shapes of various dimensions.

Table VII. Defects analysis of GR100 before and after irradiation. The number of same, disappeared, new, and moved dislocations were counted and converted into a percentage.

	Type	Count	Percentage
	Same	595	44.64 %
	Disappeared	311	23.33 %
	New	362	27.16 %
	Moved	65	4.87 %
	Total	1333	100 %

Interestingly, some defects disappeared after irradiation in the GR5 sample. The number of disappeared defects is much more than that of new defects. However, in the GR25 sample, the number of new defects is much more than that of disappeared defects. In GR 75 sample and GR100 sample, the number of new defects is more than that of disappeared defects, but the numbers are similar. Overall, half of the total defects did not change. Dislocation density is estimated to be $10^4/\text{cm}^2$ and not changed after irradiation. For the reason that the strain and tilt maps were not made, dislocation contrast could no longer be distinguished from the surface morphology.

Based on the fact that only some of the dislocations can be correlated to irradiation defects and the number of new defects is not proportional to the irradiation time, it is plausible that there would be a certain irradiation time to generate new defects and remove the existing defects, making our argument more convincing. Around 5-hour irradiation could be a certain irradiation time. With the optical and electrical characteristics of GR5 and GR25, we strongly suspect that defects in GaN can be reduced to a maximum at a certain irradiation time by neutrons. In other words, GaN can be healed by neutron irradiations and improve its quality.

References

- [1] J. Karpiński, S. Porowski, "High pressure thermodynamics of GaN", Journal of Crystal Growth 66 (1984) 11-20, [https://doi.org/10.1016/0022-0248\(84\)90071-X](https://doi.org/10.1016/0022-0248(84)90071-X).
- [2] J. Unland, B. Onderka, A. Davydov, R. Schmid-Fetzer, "Thermodynamics and Phase Stability in the Ga-N System", Journal of Crystal Growth 256 (2003) 33-51, [https://doi.org/10.1016/S0022-0248\(03\)01352-6](https://doi.org/10.1016/S0022-0248(03)01352-6).
- [3] E.H. Rhoderick and R.H. Williams, "Metal-Semiconductor Contacts" (Clarendon: Oxford, 1988), p. 121.
- [4] Kumar, A., Arafin, S., Amann, M.C. et al, "Temperature dependence of electrical characteristics of Pt/GaN Schottky diode fabricated by UHV e-beam evaporation", Nanoscale Res Lett 8 (2013) 481, <https://doi.org/10.1186/1556-276X-8-481>.
- [5] R.T. Tung, "Electron transport at metal-semiconductor interfaces: General theory", Phys. Rev. B 45 (1992) 13502, <https://doi.org/10.1103/PhysRevB.45.13509>.
- [6] Yafei Liu et al, "Microstructure Analysis of GaN Epitaxial Layers During Ion Implantation Using Synchrotron X-Ray Topography", 2021 ECS Trans. 104 (2021) 113, <https://doi.org/10.1149/10407.0113ecst>.
- [7] Yafei Liu, Balaji Raghobhamachar, Hongyu Peng, Tuerxun Ailihumaer, Michael Dudley, Ramon Collazo, James Tweedie, Zlatko Sitar, F. Shadi Shahedipour-Sandvik, Kenneth A. Jones, Andrew Armstrong, Andrew A. Allerman, Karolina Grabianska, Robert Kucharski, Michal Bockowski, "Synchrotron X-ray topography characterization of high quality ammonothermal-grown gallium nitride substrates", Journal of Crystal Growth 551 (2020), <https://doi.org/10.1016/j.jcrysgro.2020.125903>.

High dose GaN sample irradiation at 40 MeV

Andrei Patapenka, Roman Gromov, and Sergey Chemerisov
Argonne National Laboratory
Experimental Operations and Facilities Division

1. Irradiation of the samples 40 MeV

First of high-power irradiation was conducted on June 22, 2022. Total time of irradiation was 100 hours and average beam power on the target was 15 kW. Total accumulated beam power on the target was 1500 kW*h

1.1. Irradiation setup

We have utilized the same irradiation setup as described in quarterly report from October 2021. The high-power converter was designed to accommodate up to 20 kW beam power at 40 MeV. Three GaN samples were separated thin soft aluminum foils and whole assembly was wrapped in another aluminum foil. Total of two assemblies (6 samples) were irradiated in this experiment. First assembly was placed between x-ray converter and ring mask, and second assembly was placed between ring mask and aluminum cooling plate. The purpose of the foils is to provide good thermal contact between the sample and cooled surfaces of the x-ray converter, mask and the cooling plate. Four bolts connect x-ray converter and backplate holding sample assembly in place and applying pressure to GaN sample/aluminum foil sandwich ensuring good contact facilitating thermal transfer. We used grafoil washers that act as a spring allowing more gradual application of pressure on the samples.

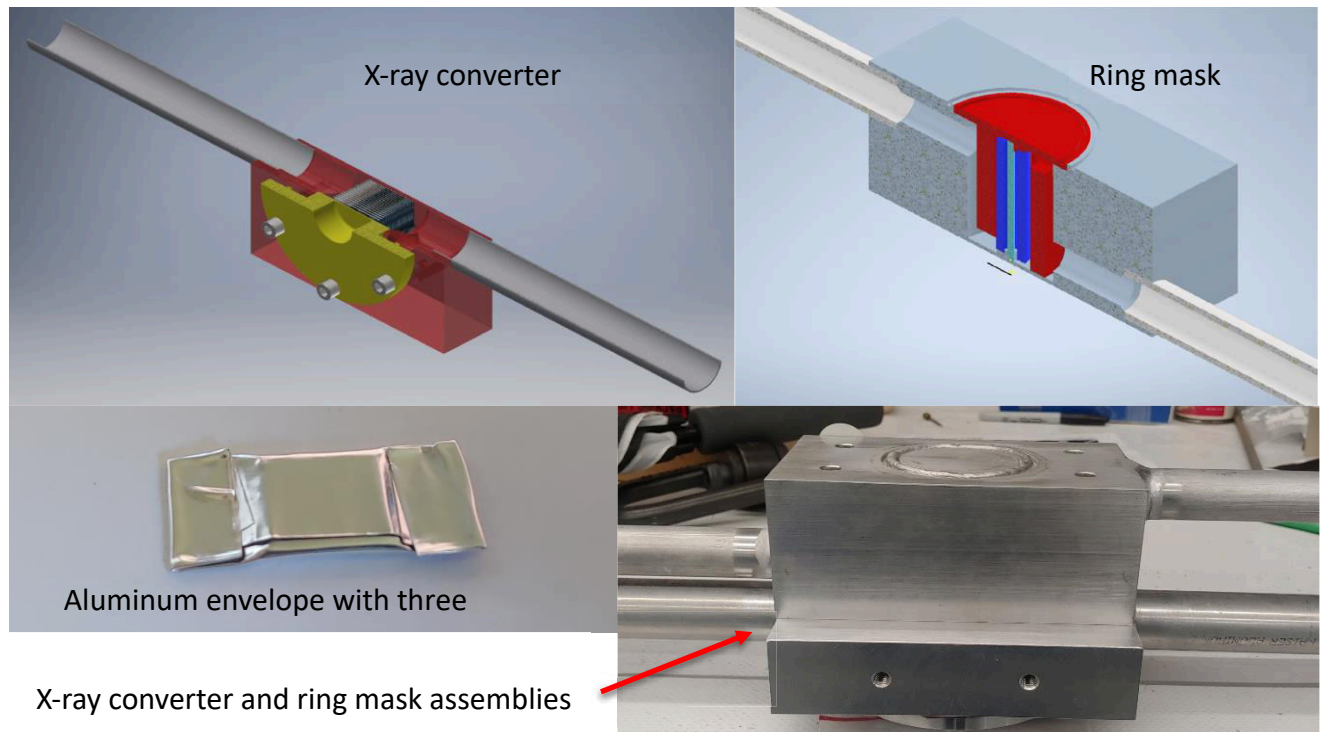


Figure 1. Experimental setup used for the irradiation. X-ray converter (top right), Ring mask (top left), aluminum envelope with three GaN samples, and x-ray converter with the ring mask before GaN samples are inserted.

1.2. Irradiation parameters

The energy spectrum of the electron beam used in this irradiation is shown in Figure 2. The magnetic energy analyzer currently used in the facility is limited to 40 MeV due to water cooling limitations for the magnet. So, we initially tune the spectrum at slightly lower energy and then lower the peak beam current according to the beam load line developed for our accelerator. Figure 2 shows energy spectrum with the peak at 35.5 MeV at 0.46A peak injector current; for irradiation injector current was lowered to 0.38 A that corresponds to 40 MeV beam energy.

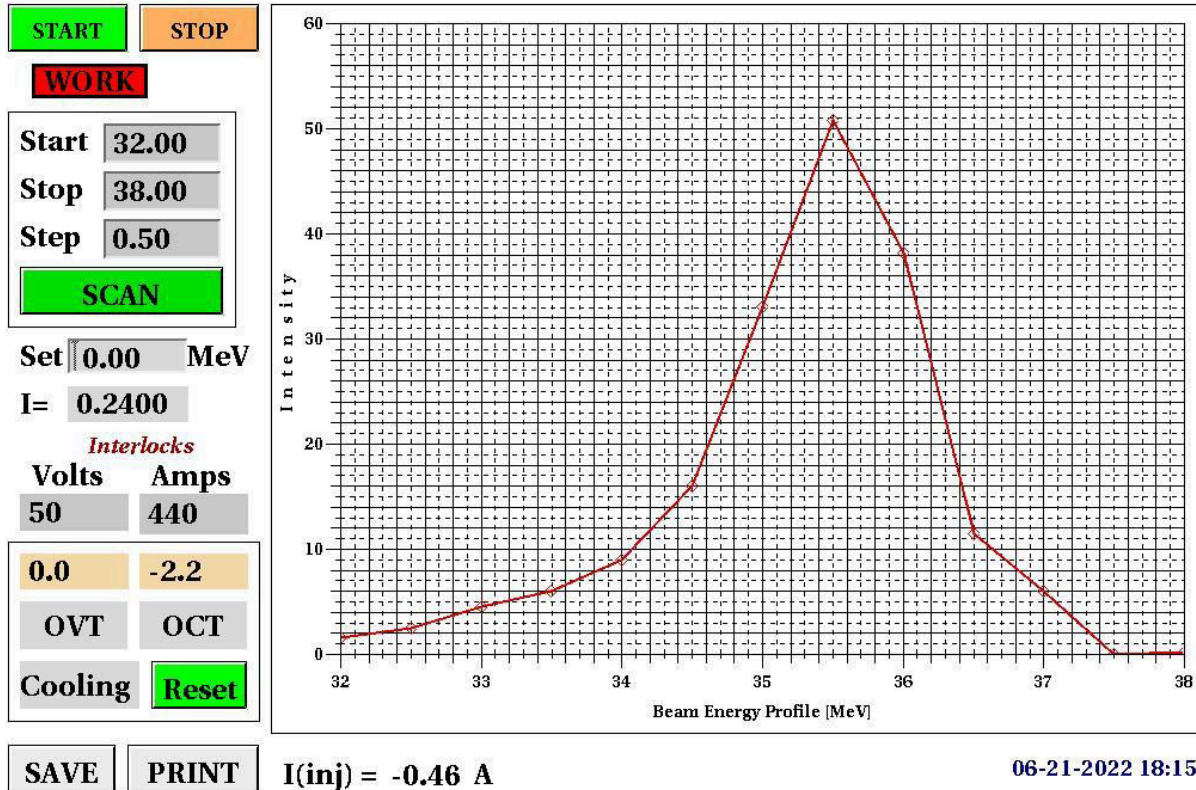


Figure 2. Energy spectrum electron beam used to GaN sample irradiation at 40 MeV.

Beam profile on the target was measured using optical emission from optical transmission radiation (OTR). The beam profiles for irradiation at 40 MeV is shown on Figure 3. Gaussian approximation gives 11.0 mm by 10.8 mm Full Width at Half Maximum (FWHM). After recording of the beam profile, the sample and irradiation apparatus was placed at the beam port and the center of the sample was aligned with the center of the beam.

Beam current and energy were continually recorded during irradiation. Beam current history is shown on Figure 4. There were several short interruptions of the irradiation due to arcing in the accelerator structures.

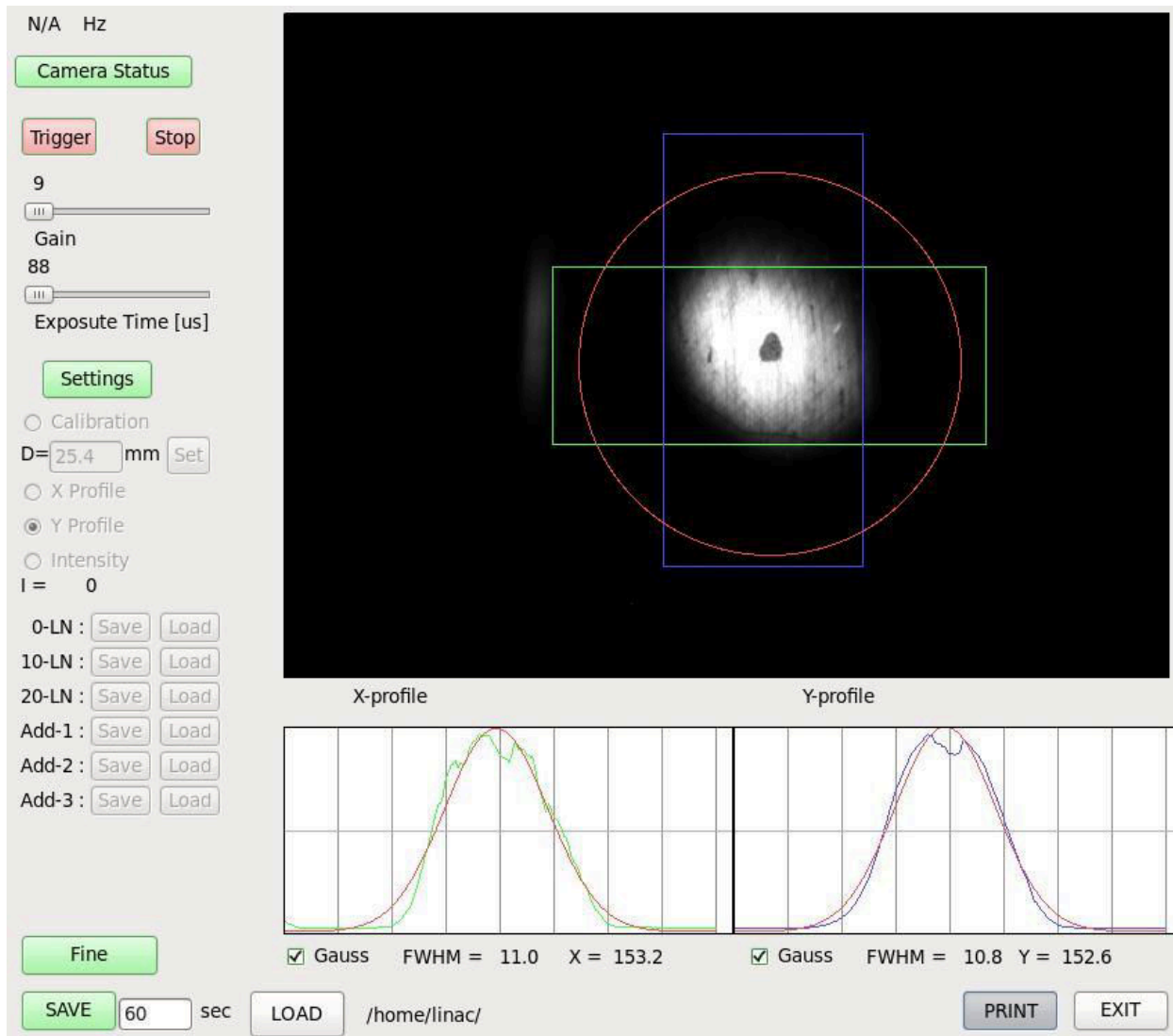


Figure 3. Beam profile at the sample location recorded at 40 MeV beam energy prior to irradiation. 11.0 mm by 10.8 mm FWHM gaussian beam profile is necessary to provide homogeneous, within ~25%, x-ray field across the sample.

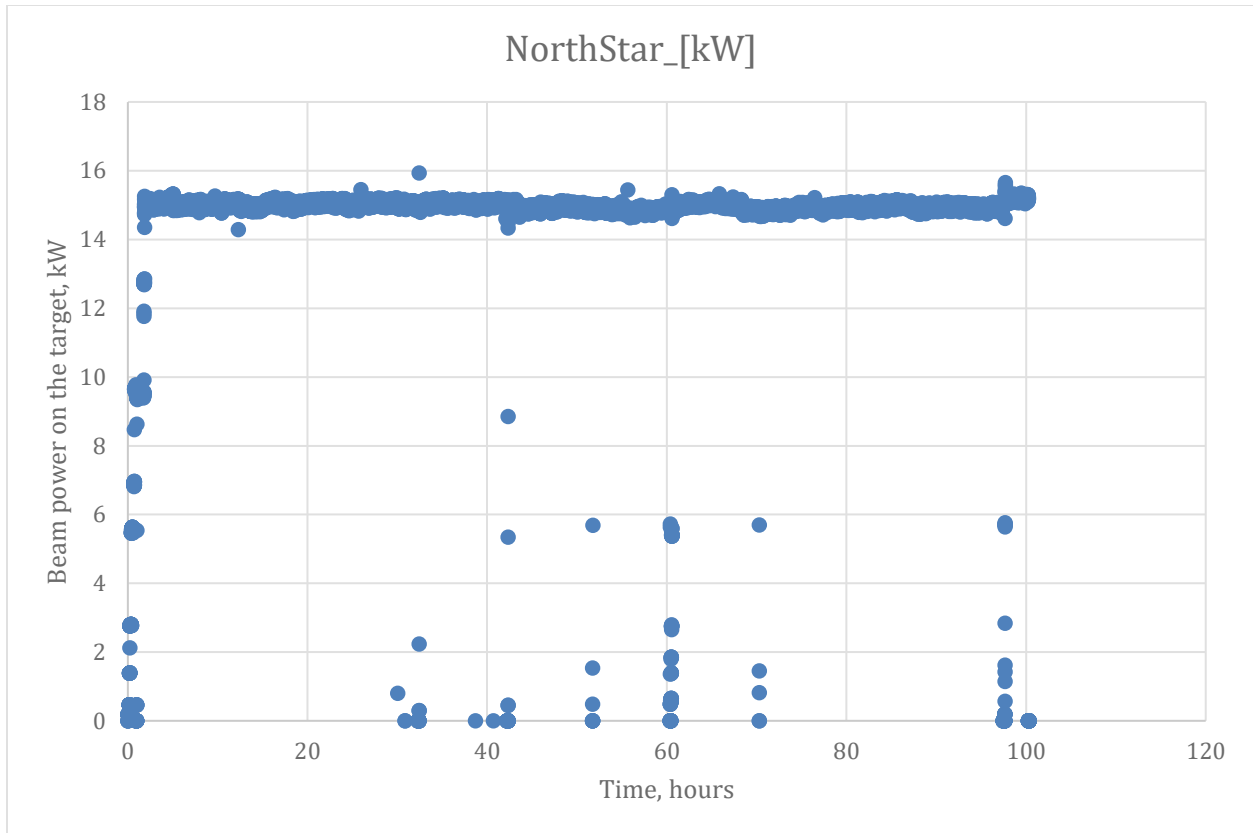


Figure 4. Beam current history for 100 hour irradiation of GaN samples.

2. Gamma counting of the samples

For gamma-counting we used N-type Hyper Pure Germanium detector (HPGe) from ORTEC Model GMX30P4-76 with useful energy range from 3keV to 10 MeV. Detector is equipped with integrated cryocooling system. Samples were placed at 44 inches from the detector cap; no collimator or shielding were used. Results of the measurements are summarized in Table 1 and 2. Gamma counting was conducted on July 22, 26 days after end of irradiation.

Table 1. Activities in all GaN samples after four weeks cool down.

Isotope	Half-life, s	Lambda	A, Bq	A, microCi	Error
Ga67	2.82E+05	2.46E-06	1.09E+07	294.6	7%
Cu67	2.23E+05	3.11E-06	5.50E+05	14.9	>50%
Ga72	5.08E+04	1.37E-05	1.70E+03	0.046	20%

3. Simulations of isotopes production in GaN/Ga₂O₃ samples

This chapter includes Monte-Carlo simulations results on isotopes production in GaN and Ga₂O₃ samples irradiated by 15, 20 and 40 MeV electron beams. The sample's dimension was taken as 0.65x0.65x0.033 cm³. The irradiation geometry is shown in Figure 5. It consists of Tantalum water cooled converter with Al envelope and the sample.

The optimization studies were performed using FLUKA [1] code to estimate optimal number of Tantalum plates (0.25 mm each + 0.5 mm for water-coolant channel) to maximize Zn production rate. The optimal number of Ta-plates for 0.6x0.6 cm FWHM beams were the following: 40 MeV – 9-10 plates; 20 MeV 5-6 plates; 15 MeV 3-4 plates.

Reaction cross section were calculated with TALYS code [2] and listed in appendix 1. Stable isotopes yield also given for each reaction. Cross-sections for reactions with the most significant impact are shown in Figure 6.

Production of stable isotopes in GaN and Ga₂O₃ samples are given in Table 2. The number of atoms were calculated for 160 hours of continuous irradiation at 3kW beam power, and in the assumption that radioactive parent nuclides decayed into target isotope. The irradiated geometry was the same for the data consistency – 9 Ta plates in the converter.

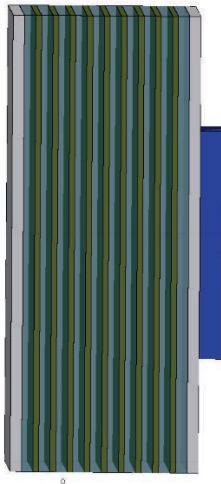


Figure 5 – Irradiated geometry, ZY section.

In the figure:

Dark Blue – irradiated sample (1 mm thick)

Dark Green – Ta plates (0.25 mm thick)

Blue – Water cooling channels (0.5 mm)

Silver – Al converter's body

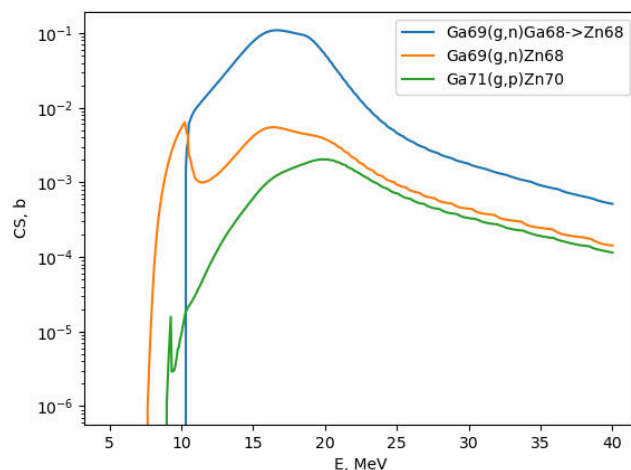


Figure 6 – Reaction cross-sections obtained with TALYS code.

Table 2. Nuclei production

40 MeV beam, 3kW × 160 hours		
Stable isotopes	Sample:	
	GaN	Ga ₂ O ₃
Zn	2.67E+15	2.50E+15
Ge	1.53E+13	1.43E+13
C	2.34E+14	1.25E+14
N	N/A	3.54E+14
20 MeV beam, 3kW × 160 hours		
Stable isotopes	Sample:	
	GaN	Ga ₂ O ₃
Zn	4.97E+14	4.65E+14
Ge	5.84E+12	5.47E+12
C	4.94E+13	8.77E+12
N	N/A	7.41E+12
15 MeV beam, 3kW × 160 hours		
Stable isotopes	Sample:	
	GaN	Ga ₂ O ₃
Zn	6.25E+13	5.85E+13
Ge	1.94E+12	1.82E+12
C	1.56E+13	2.10E+12
N	N/A	4.18E+11

Appendix 1

Production reactions with quantum yield (of stable atom)

Zn production:

Photo-induced on ^{69}Ga :

' $^{69}\text{Ga}(\text{g},2\text{n})^{67}\text{Ga}$ ': 1,
' $^{69}\text{Ga}(\text{g},1\text{p}2\text{n})^{66}\text{Zn}$ ': 1,
' $^{69}\text{Ga}(\text{g},2\text{p})^{67}\text{Cu}$ ': 1,
' $^{69}\text{Ga}(\text{g},2\text{p}3\text{n})^{64}\text{Cu}$ ': 1,
' $^{69}\text{Ga}(\text{g},3\text{n})^{66}\text{Ga}$ ': 1,
' $^{69}\text{Ga}(\text{g},2\text{p}1\text{n})^{66}\text{Cu}$ ': 1,
' $^{69}\text{Ga}(\text{g},1\text{n})^{68}\text{Ga}$ ': 1,
' $^{69}\text{Ga}(\text{g},1\text{p}1\text{n})^{67}\text{Zn}$ ': 1,
' $^{69}\text{Ga}(\text{g},1\text{p})^{68}\text{Zn}$ ': 1,

Neutron-induced on ^{69}Ga :

' $^{69}\text{Ga}(\text{n},2\text{p}2\text{n})^{66}\text{Cu}$ ': 1,
' $^{69}\text{Ga}(\text{n},2\text{n})^{68}\text{Ga}$ ': 1,
' $^{69}\text{Ga}(\text{n},1\text{p}2\text{n})^{67}\text{Zn}$ ': 1,
' $^{69}\text{Ga}(\text{n},2\text{p})^{68}\text{Cu}$ ': 1,
' $^{69}\text{Ga}(\text{n},3\text{n})^{67}\text{Ga}$ ': 1,
' $^{69}\text{Ga}(\text{n},1\text{p}3\text{n})^{66}\text{Zn}$ ': 1,
' $^{69}\text{Ga}(\text{n},3\text{p})^{67}\text{Ni}$ ': 1,
' $^{69}\text{Ga}(\text{n},2\text{p}4\text{n})^{64}\text{Cu}$ ': 1,
' $^{69}\text{Ga}(\text{n},4\text{n})^{66}\text{Ga}$ ': 1,
' $^{69}\text{Ga}(\text{n},\text{g})^{70}\text{Ga}$ ': 1,
' $^{69}\text{Ga}(\text{n},2\text{p}1\text{n})^{67}\text{Cu}$ ': 1,
' $^{69}\text{Ga}(\text{n},3\text{p}1\text{n})^{66}\text{Ni}$ ': 1,
' $^{69}\text{Ga}(\text{n},1\text{p}1\text{n})^{68}\text{Zn}$ ': 1,

Photo-induced on ^{71}Ga :

' $^{71}\text{Ga}(\text{g},2\text{p}2\text{n})^{67}\text{Cu}$ ': 1,
' $^{71}\text{Ga}(\text{g},3\text{p}2\text{n})^{66}\text{Ni}$ ': 1,
' $^{71}\text{Ga}(\text{g},1\text{p}2\text{n})^{68}\text{Zn}$ ': 1,
' $^{71}\text{Ga}(\text{g},2\text{p}3\text{n})^{66}\text{Cu}$ ': 1,
' $^{71}\text{Ga}(\text{g},3\text{n})^{68}\text{Ga}$ ': 1,
' $^{71}\text{Ga}(\text{g},1\text{p}3\text{n})^{67}\text{Zn}$ ': 1,
' $^{71}\text{Ga}(\text{g},4\text{n})^{67}\text{Ga}$ ': 1,
' $^{71}\text{Ga}(\text{g},1\text{p}4\text{n})^{66}\text{Zn}$ ': 1,
' $^{71}\text{Ga}(\text{g},2\text{p}5\text{n})^{64}\text{Cu}$ ': 0.385,
' $^{71}\text{Ga}(\text{g},2\text{p}1\text{n})^{68}\text{Cu}$ ': 1,
' $^{71}\text{Ga}(\text{g},1\text{n})^{70}\text{Ga}$ ': 0.0041,
' $^{71}\text{Ga}(\text{g},1\text{p})^{70}\text{Zn}$ ': 1,

Neutron-induced on ^{71}Ga :

' $^{71}\text{Ga}(\text{n},2\text{p}2\text{n})^{68}\text{Cu}$ ': 1,
' $^{71}\text{Ga}(\text{n},3\text{p}2\text{n})^{67}\text{Ni}$ ': 1,
' $^{71}\text{Ga}(\text{n},2\text{n})^{70}\text{Ga}$ ': 0.0041,
' $^{71}\text{Ga}(\text{n},2\text{p})^{70}\text{Cu}$ ': 1,

$^{71}\text{Ga}(n,2p3n)^{67}\text{Cu}$:1,
 $^{71}\text{Ga}(n,3p3n)^{66}\text{Ni}$:1,
 $^{71}\text{Ga}(n,1p3n)^{68}\text{Zn}$:1,
 $^{71}\text{Ga}(n,2p4n)^{66}\text{Cu}$:1,
 $^{71}\text{Ga}(n,4n)^{68}\text{Ga}$:1,
 $^{71}\text{Ga}(n,1p4n)^{67}\text{Zn}$:1,
 $^{71}\text{Ga}(n,5n)^{67}\text{Ga}$:1,
 $^{71}\text{Ga}(n,1p5n)^{66}\text{Zn}$:1,
 $^{71}\text{Ga}(n,2p6n)^{64}\text{Cu}$:0.385

Ge production:

$^{69}\text{Ga}(n,g)^{70}\text{Ga}$: 1-0.0041,
 $^{71}\text{Ga}(n,g)^{72}\text{Ga}$: 1,
 $^{71}\text{Ga}(g,1n)^{70}\text{Ga}$: 1-0.0041

C production:

$^{14}\text{N}(g,1p1n)^{12}\text{C}$: 1,
 $^{14}\text{N}(n,1p2n)^{12}\text{C}$: 1,
 $^{16}\text{O}(g,2p2n)^{12}\text{C}$: 1,
 $^{16}\text{O}(n,2p3n)^{12}\text{C}$: 1,
 $^{14}\text{N}(g,1p)^{13}\text{C}$: 1,
 $^{14}\text{N}(n,1p1n)^{13}\text{C}$: 1,
 $^{16}\text{O}(g,2p1n)^{13}\text{C}$: 1,
 $^{16}\text{O}(n,2p2n)^{13}\text{C}$: 1,
 $^{14}\text{N}(n,1p)^{14}\text{C}$: 1,
 $^{16}\text{O}(g,2p)^{14}\text{C}$: 1,
 $^{16}\text{O}(n,2p1n)^{14}\text{C}$: 1

N production:

$^{16}\text{O}(g,1n)^{15}\text{O}$: 1,
 $^{16}\text{O}(g,1p)^{15}\text{N}$: 1,
 $^{16}\text{O}(g,1p1n)^{14}\text{N}$: 1

References:

1. <http://www.fluka.org/fluka.php>
2. https://www-nds.iaea.org/talys/tutorials/talys_v1.96.pdf

ARPA-E PNDIODES

GaN vertical power FinFETs

Period covered by report:

May1, 2022 – July 31, 2022

Principal Investigator:

Prof. Tomás Palacios

Email: tpalacios@mit.edu

Phone: (617) 324-2395 Fax: (617) 258-7393

Institution: Massachusetts Institute of Technology

Department: Electrical Engineering and Computer Science

Institution Address:

77 Massachusetts Avenue, Cambridge, MA 02139

July 31, 2022

Executive Summary

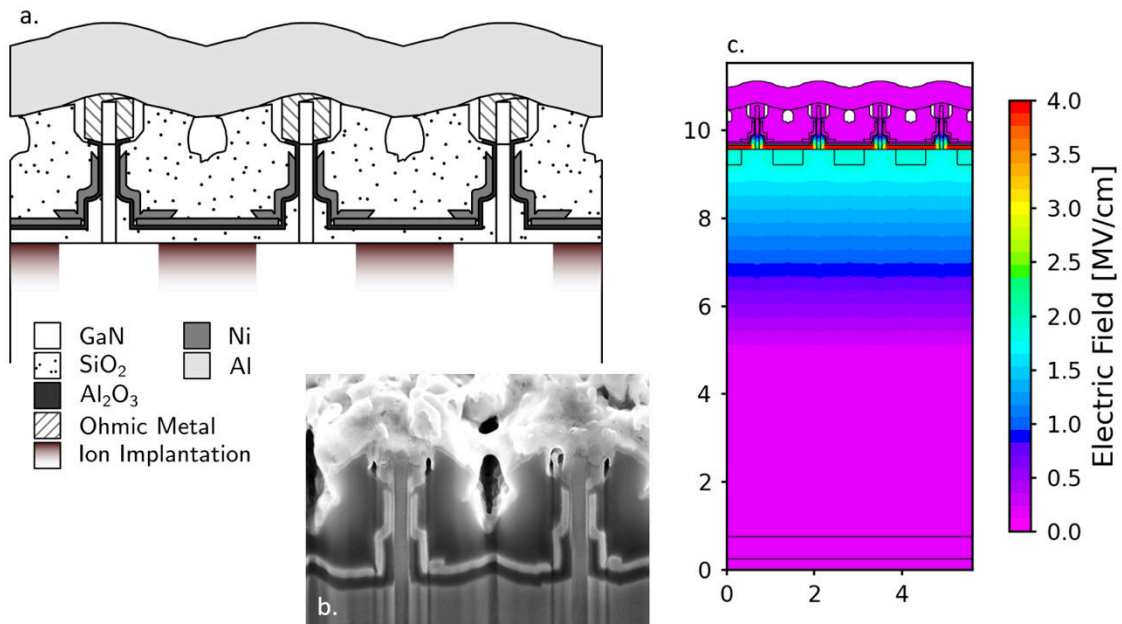
Vertical GaN power transistors offer improved performance over lateral GaN transistors in terms of current rating per unit area, thermal management, and reliability. Thanks to the generous support of ARPA-E SWITCHES, we have demonstrated GaN Power FinFETs with record 5 A current rating and 1200V BV with a device footprint of 0.45 mm². Under the PNDIODES program, we have focused on pushing the performance limits (current rating of 50A and breakdown voltage of 3000V) of vertical GaN power FinFETs.

This quarter, we have continued testing the finFETs presented in Quarter 9. Full on-state IV characterization is complete, and CV measurements are underway. Additionally, we have completed version 2 of our in-house process simulator that provides substantial performance improvements with far fewer bugs.

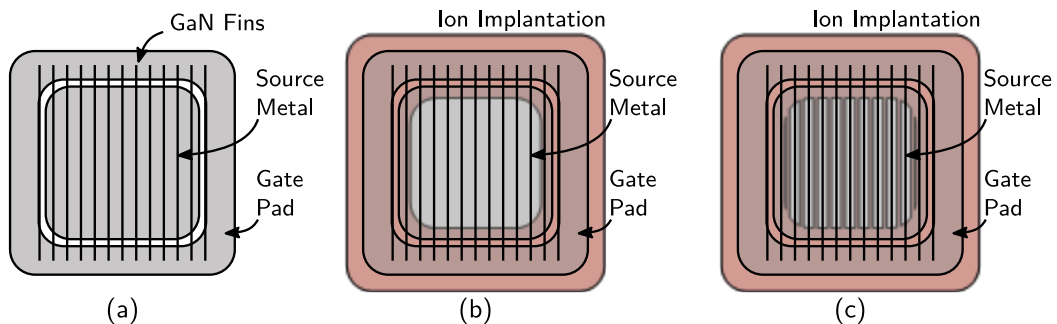
1 Vertical GaN FinFET Characterization

1.1 IV Characterization

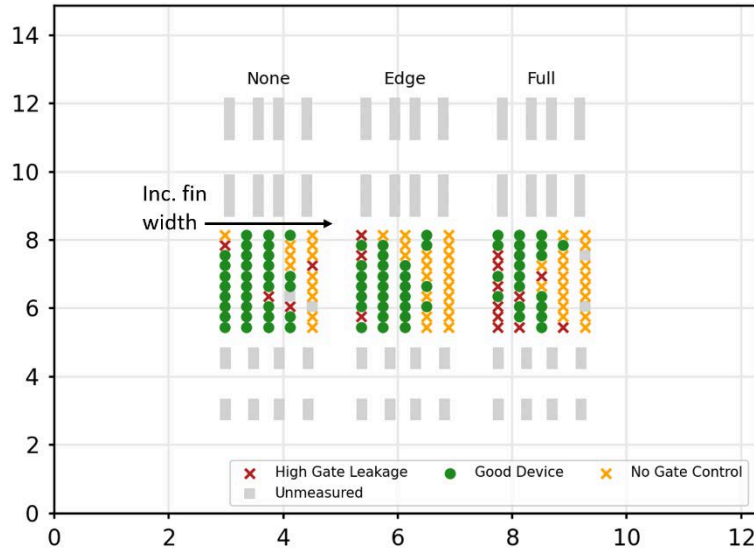
As reported in the previous quarter, full on-state IV characterization has been performed of the devices shown in Fig. 1 with edge termination schemes shown in Fig. 2. A yield map is shown in Fig. 3 and plots of the threshold voltage and maximum drain current are shown in Fig. 4. To date, we are still awaiting breakdown measurements, which will occur after full CV characterization.



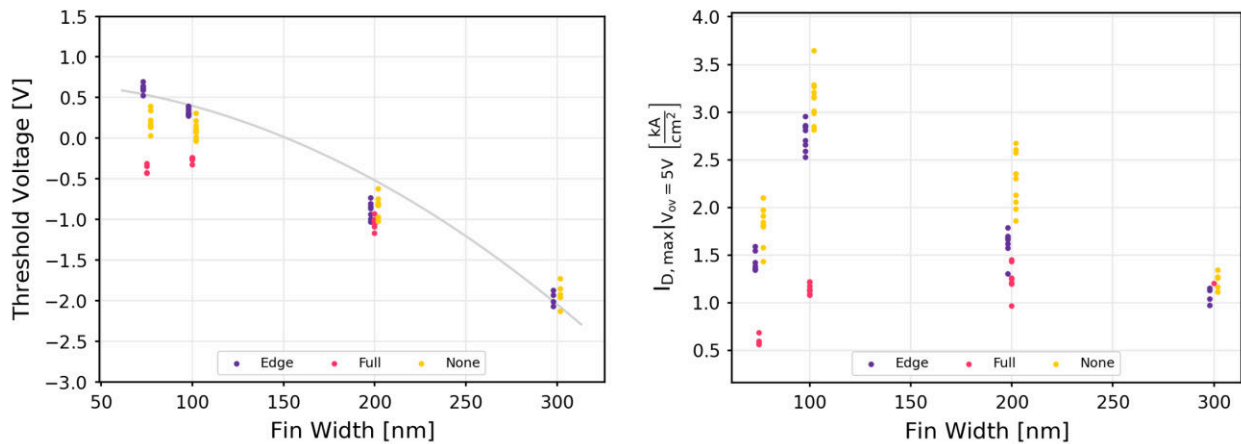
28. (a) Process simulation results of a vertical GaN finFET. (b) Actual fabrication results using the simulated process. (c) TCAD simulations from Atlas using the exact simulated structure for devices in the off-state.



29. Implantation patterns for FinFETs with (a) no edge termination, denoted as “None”, (b) implantation along the device periphery (shown in red), denoted as “Edge”, and (c) implantation along the device periphery and self-aligned implantation between fins, denoted as “Full”.



30. Yield map for finFETs for ion implantation tests. Within each vertical die, device columns from left to right are for 75, 100, 200, 300, and 400 nm fins.



31. (left) Threshold voltage versus fin width distribution. The gray line indicates the theoretical threshold voltage for a channel doping of $1.2 \times 10^{17} \text{ cm}^{-3}$. (right) Drain current extracted from an overdrive voltage of 5 V and drain bias of 5 V versus fin w

1.2 CV Characterization

We are currently working with an undergraduate student in MIT's Undergraduate Research Opportunities Program to perform full CV characterization of our devices. This includes setup of the semi-automatic probestation to automate the extraction of C_{rss} , C_{oss} , and C_{iss} . Since our devices have a negative or near-zero threshold (depending on fin width), it is not possible to use our standard measurement setup to simultaneously bias the gate while measuring capacitance. Following the methodology presented in [1], we have purchased AC shorting capacitors and blocking resistors to make proper measurement circuits. After CV characterization, destructive breakdown measurements will be

performed. We will then use this data to model the transistors in circuit simulations to demonstrate power conversion systems with vertical GaN finFETs.

2 Process Simulation

In the previous quarter, we reported an in-house process simulator developed with Python for aiding in the design of complex 3-D transistors. This simulator is capable of accurately replicating the following processes:

1. Arbitrary angle deposition with shadow masking
2. Anisotropic dry etching
3. Isotropic wet etching
4. Ion implantation
5. Liftoff
6. Crystallographic wet etching
7. Conformal and asymmetric depositions with keyhole voiding
8. Physical vapor deposition based on iterative line-of-sight techniques
9. Back side deposition
10. Process flow export to various image types including GDS for easy dimensioning
11. Animated process flow export
12. Export to Atlas for electrical simulations

Since last quarter, we have developed version 2. With the new release, many bugs have been removed to improve reliability and performance. The previous generation relied entirely on Python for complex polygon operations, which becomes cumbersome, particularly for the ray-tracing techniques needed for physical vapor deposition. To perform the polygon operations, we initially used the open-source Python package, `gdspy`. However, as of Spring 2022, a new package, `gdstk`, offers 5-100× speedup in polygon operations. Additionally, we have implemented our own C library for complex operations that offers a ~100× speedup and enables far more accurate algorithms to simulate sputtering and PVD processes.

References

- [1] *The Parametric Measurement Handbook*, 4th ed. Keysight Technologies.

DE-AR0000874 : University of Missouri - Kwon
Q3 of FY 2022: April 1, 2022 - June 30, 2022

Schedule - Updates

WBS	Task Name	Mile-stone	Baseline Start	Baseline End	Actual Start	Actual End	% Comp
1	Development of work plan		9/20/2017	12/19/2017			100%
└ M1.1	Q1: Work plan finalized	▼	12/19/2017	12/19/2017			100%
2	Neutron activation of Ge dopants in GaN wafers		9/20/2017	6/19/2018	9/20/2017	4/30/2019	100%
└ 2.1	Establish irradiation protocol		9/20/2017	12/19/2017	9/20/2017	12/31/2017	100%
└ 2.2	Scoping experiments		9/20/2017	6/19/2018	11/12/2017	6/30/2018	100%
└ 2.3	C14 reduction scoping experiments		3/20/2019	12/19/2019	3/20/2019	12/19/2019	100%
└ 2.4	PhotonuclearScopingexperiments		3/20/2019	12/19/2020	10/17/2019		90%
└ 2.5	Development of masks for transmutation doping		9/20/2019	6/19/2020	10/2/2019		80%
└ 2.6	Masking Scoping Experiments		12/20/2019	9/19/2020	12/20/2019		70%
└ 2.7	Doping of mono-isotope GaN		9/20/2019	12/19/2020	8/15/2019		25%
└ M2.1.1	Q1: Establish wafer supply chain	▼	12/19/2017	12/19/2017	9/20/2017	11/30/2017	100%
└ M2.2.1	Q3: Consistent doping concentration	▼	6/19/2018	6/19/2018	1/2/2018	6/30/2018	100%
└ M2.3.1	Q9: Consistent doping concentration	▼	12/19/2019	12/19/2019	8/20/2019	12/19/2019	100%
└ M2.4.1	Q10: Consistent doping concentration	▼	6/19/2020	6/19/2020	6/8/2020		90%
└ M2.5.1	Q10: Masking material for transmutation doping.	▼	3/19/2020	3/19/2020	6/8/2020		90%
└ M2.6.1	Q12: Linear selective doped GaN	▼	3/19/2020	9/19/2020	10/8/2019		90%
3	Characterization of GaN wafers doped by neutron transmutation		12/20/2017	12/19/2020	12/11/2017	4/30/2019	100%
└ 3.1	Impurity analysis		12/20/2017	3/19/2020	1/8/2018	12/31/2018	100%
└ 3.2	Crystallinity analysis		12/20/2017	6/19/2020	2/6/2018	12/31/2018	100%
└ 3.3	Electrical analysis		12/20/2017	12/19/2020	12/11/2017	6/30/2019	100%
└ 3.4	Electrical analysis of selective doping		12/20/2019	12/19/2020	10/8/2019		60%
└ M3.3.1	Q4: Consistent carrier concentration	▼	9/19/2018	9/19/2018			100%
└ M3.3.2	Q10: Consistent n-type carrier concentration	▼	3/19/2020	3/19/2020	10/2/2019	6/30/2020	100%
└ M3.3.3	Q11: Consistent p-type behavior	▼	6/19/2020	6/19/2020	6/1/2020		85%
└ M3.4.1	Q13: Consistent vertical doping	▼	12/19/2020	12/19/2020	6/1/2020		100%
4	Technology To Market		9/20/2017	12/19/2020	10/2/2017	6/30/2019	100%
└ 4.1	Invention disclosures and patent applications		9/20/2017	12/19/2020	10/2/2017	6/30/2019	100%
└ 4.2	Publications and Presentations		3/20/2018	12/19/2020		6/30/2019	90%

DE-AR0000874 : University of Missouri - Kwon
Q3 of FY 2022: April 1, 2022 - June 30, 2022

WBS	Task Name	Mile- stone	Baseline Start	Baseline End	Actual Start	Actual End	% Comp
└ M4.1.1	Q1: Background IP report	▼	12/19/2017	12/19/2017	10/2/2017	12/31/2017	100%
└ M4.2.1	Q4: Presentation / Publication	▼	9/19/2018	9/19/2018	3/13/2018	6/30/2019	90%
└ M4.1.2	Q4: IP Update	▼	9/19/2018	9/19/2018		6/30/2019	100%
└ M4.1.3	Q13: IP Update	▼	12/19/2020	12/19/2020			90%
└ M4.2.1	Q4: Presentation/Publication	▼	9/19/2018	9/19/2018			100%
└ M4.2.2	Q13:Presentation /Publication	▼	12/19/2020	12/19/2020			70%
5	Collaboration Work		9/20/2019	12/19/2020	9/20/2019		60%
└ 5.1	Epi-layer growthfor a drift layer		3/20/2020	9/19/2020	2/20/2020		70%
└ 5.2	Doping processfor a drift layer		3/20/2020	9/19/2020	3/12/2020		70%
└ 5.3	Vertical GaNdevice creation		3/20/2020	12/19/2020			30%
└ 5.4	Determineirradiationparameters forcarbon behaviorstudy		6/20/2019	3/19/2020			70%
└ 5.5	Irradiation ofcarbon behaviorstudy		9/20/2019	3/19/2020	9/20/2019		80%
└ 5.6	ElectricalCharacterizationof the carbonbehavior study		9/20/2019	6/19/2020	9/20/2019		60%
└ M5.2.1	Q13: Creation ofdoped layers forFinFET Devices	▼	12/19/2020	12/19/2020			70%
└ M5.6.1	Q10:Characterization of Cdoping in GaN	▼	3/19/2020	3/19/2020	1/3/2020		90%

Additional Performance Updates

A) ISSUES, RISKS, AND MITIGATION

We ran out of the research fund before the end of the extended project period, and have discussed this matter with the program director.

Contains protected data: Protected Rights Data SBIR/STTR Data No Protected Data

B) CHANGES IN APPROACH

N/A

C) CHANGES IN PROJECT PERSONNEL

N/A

Technology To Market (T2M)

A. PUBLICATIONS

Conference Presentation

- Selective Neutron Transmutation Doping of GaN , Jeongwoo Kim, Matthias D. Frontzek, Lowell Crow Jr, and Jae. W. Kwon, *ARPA-E Summit*, Denver CO (2022)

B. OTHER PROJECT OUTPUT

N/A

C. FOLLOW-ON FUNDING

N/A

Administrative and Legal Updates

DISCLOSURES

N/A

DE-AR0000874 : University of Missouri - Kwon
 Q3 of FY 2022: April 1, 2022 - June 30, 2022

Cost Updates - LEAD: University of Missouri (DE-AR0000874)

High quality GaN FETs through transmutation doping and low temperature processing

ARPA-E RECORDS ONLY (invoices edited by performer are highlighted)

Invoice #	Date	Total	Federal Share	Performer Share	Shortpays	TT&O	Personnel	Fringe Benefits	Travel	Equipment	Supplies	Contractual	Construction	Other	Indirect
AR0000874-GM00229819	2/27/2018	\$40,310.60	\$40,310.60	\$0.00	\$0.00	\$0.00	\$8,509.26	\$1,309.43	\$1,528.27	\$0.00	\$14,659.84	\$0.00	\$0.00	\$0.00	\$14,303.80
AR0000874-GM00231274	3/27/2018	\$21,222.09	\$5,722.09	\$15,500.00	(\$263.50)	\$0.00	\$2,618.26	\$332.31	\$0.00	\$0.00	\$0.00	\$0.00	\$0.00	\$16,431.45	\$1,840.07
AR0000874-GM00232388	4/30/2018	\$9,422.99	\$9,422.99	\$0.00	\$0.00	\$0.00	\$3,168.69	\$374.41	\$0.00	\$0.00	\$374.91	\$0.00	\$0.00	\$2,161.32	\$3,343.66
AR0000874-GM00233996	6/7/2018	\$8,724.82	\$8,724.82	\$0.00	\$0.00	\$2,085.77	\$3,168.71	\$374.42	\$0.00	\$0.00	\$0.00	\$0.00	\$0.00	\$2,085.77	\$3,095.92
AR0000874-GM00235448	7/20/2018	\$9,089.15	\$9,089.15	\$0.00	\$0.00	\$1,937.57	\$3,127.61	\$425.93	\$0.00	\$0.00	\$372.86	\$0.00	\$0.00	\$1,937.57	\$3,225.18
AR0000874-GM00236640	8/14/2018	\$45,587.09	\$45,587.09	\$0.00	\$0.00	\$48.00	\$16,502.64	\$4,881.20	\$0.00	\$10,282.15	\$0.00	\$0.00	\$0.00	\$2,160.00	\$11,761.10
AR0000874-GM00237640	8/29/2018	\$34,932.69	\$34,932.69	\$0.00	\$0.00	\$0.00	\$2,381.86	\$299.67	\$0.00	\$0.00	\$19,855.69	\$0.00	\$0.00	\$0.00	\$12,395.47
AR0000874-GM00238852	10/8/2018	\$6,732.34	\$6,732.34	\$0.00	\$0.00	\$0.00	\$3,230.04	\$385.75	\$0.00	\$0.00	\$727.65	\$0.00	\$0.00	\$0.00	\$2,388.90
AR0000874-GM00240232	10/22/2018	\$5,755.26	\$5,755.26	\$0.00	(\$168.95)	\$0.00	\$2,386.43	\$143.71	\$1,149.17	\$0.00	(\$198.50)	\$0.00	\$0.00	\$360.00	\$1,914.45
AR0000874-GM00243994	1/31/2019	\$43,861.54	\$43,861.54	\$0.00	\$0.00	\$0.00	\$10,112.04	\$701.38	\$1,121.71	\$0.00	\$16,222.20	\$0.00	\$0.00	\$140.42	\$15,563.79
AR0000874-GM00244762	2/26/2019	\$6,964.77	\$6,964.77	\$0.00	\$0.00	\$0.00	\$2,992.78	\$190.10	\$0.00	\$0.00	\$1,310.51	\$0.00	\$0.00	\$0.00	\$2,471.38
AR0000874-GM00246042	3/28/2019	\$27,134.98	\$27,134.98	\$0.00	\$0.00	\$0.00	\$2,993.04	\$190.19	\$0.00	\$0.00	\$12,663.07	\$0.00	\$0.00	\$2,573.20	\$8,715.48
AR0000874-GM00248162	5/3/2019	\$4,934.46	\$4,934.46	\$0.00	\$0.00	\$0.00	\$2,993.27	\$190.25	\$0.00	\$0.00	\$0.00	\$0.00	\$0.00	\$0.00	\$1,750.94
AR0000874-GM00251770	8/27/2019	\$62,855.00	\$62,855.00	\$0.00	\$0.00	\$1,090.00	\$26,984.35	\$8,264.43	\$0.00	\$0.00	\$1,431.81	\$0.00	\$0.00	\$4,784.07	\$21,390.34
AR0000874-00057744NOV2020	12/21/2020	\$838,956.61	\$786,102.23	\$52,854.38	(\$344.10)	\$3,992.55	\$116,872.38	\$33,492.03	\$1,214.35	\$100,400.00	\$62,739.47	\$346,468.11	\$0.00	\$27,118.99	\$150,651.28
AR0000874-00057744DEC2020	2/1/2021	\$41,705.73	\$30,748.04	\$10,957.69	\$0.00	\$0.00	\$7,726.04	\$2,479.27	\$0.00	\$0.00	\$141.08	\$25,668.83	\$0.00	\$0.00	\$5,690.51
AR0000874-00057744FEB2021	3/25/2021	\$120,423.10	\$117,245.21	\$3,177.89	(\$263.50)	\$0.00	\$8,120.20	\$2,500.56	\$0.00	\$0.00	\$3,216.97	\$97,797.85	\$0.00	\$759.20	\$8,028.32
AR0000874-00057744FEB22 (Pending)	5/2/2022	\$629,615.99	\$542,559.18	\$87,056.81	\$0.00	\$0.00	\$86,845.08	\$19,737.11	(\$1,186.00)	\$87,007.00	\$149,013.05	\$116,262.78	\$0.00	\$21,614.19	\$150,322.78

DE-AR0000874 : University of Missouri - Kwon
 Q3 of FY 2022: April 1, 2022 - June 30, 2022

ARPA-E RECORDS ONLY (invoices edited by performer are highlighted)

Invoice #	Date	Total	Federal Share	Performer Share	Shortpays	TT&O	Personnel	Fringe Benefits	Travel	Equipment	Supplies	Contractual	Construction	Other	Indirect
Total:		\$1,958,229.21	\$1,788,682.44	\$169,546.77	(\$1,040.05)	\$9,153.89	\$310,732.68	\$76,272.15	\$3,827.50	\$197,689.15	\$282,530.61	\$586,197.57	\$0.00	\$82,126.18	\$418,853.37
% Expended in Budget Category:		85.00%	82.89%	116.21%		12.35%	115.15%	108.71%	115.98%	98.72%	111.42%	64.55%	0.00%	46.06%	99.65%
Remaining:		\$345,620.79	\$369,266.56	(\$23,645.77)		\$64,983.08	(\$40,887.68)	(\$6,111.15)	(\$527.50)	\$2,571.85	(\$28,963.61)	\$321,878.43	\$0.00	\$96,189.82	\$1,470.63

Overall Proposed Cost Share: 6.33 % Invoiced Cost Share to Date: 8.66 % Proposed TT&O to Federal Share: 3.44 % Actual TT&O to Federal Share: 0.51 %

Agree that the information provided is accurate and correct: Yes No

DE-AR0000874 : University of Missouri - Kwon
Q3 of FY 2022: April 1, 2022 - June 30, 2022

Cost Updates - SUB: Argonne National Laboratory (18/CJ000/01/05)

High Quality GaN FETs through transmutation doping and low temperature processing

N/A

Certification of Compliance

I certify that I have the authority to make the following certification and to submit this Research Performance Progress Report on behalf of the Prime Recipient. On behalf of the Prime Recipient, I further certify that the information provided in this Research Performance Progress Report is accurate and complete as of the date shown below. I understand that false statements or misrepresentations may result in civil and/or criminal penalties under 18 U.S.C. § 1001.

Signature: Jae W Kwon

Submitted by: Prof. Jae Kwon (kwonj@missouri.edu), University of Missouri

Submitted Date: 7/31/2022 10:14:13 PM

II Bulleted list summarizing milestones due:

Milestones DUE Q1FY22

2.6 Masking Scoping Experiments

- **[In Progress: Due 9/19/21]** The collaboration with Oak Ridge National Laboratory has been significantly delayed due to overload caused by COVID.

2.7 Doping of mono-isotope GaN

- **[In Progress: Due 12/19/21]** ^{69}GaN material was shipped to UCSB in August 2021. UCSB is working on fabricating ^{69}GaN .

3.3.3 Q11: Consistent p-type behavior

- **[In Progress: Due 6/19/21]** We believe the Yttrium is the good Schottky contact metal for Zn-doped p-type GaN. After new irradiation, the Yttrium will be deposited on the Zn-doped GaN. This helps study the properties of Zn-doped GaN as a p-type dopant.

5.4 Determine irradiation parameters for carbon behavior study

- **[In progress: Due 3/19/21]** Low doped GaN and GaN with epilayers from manufacture 3 will be irradiated in May. More carbon may be able to be produced.

M5.2.1 Q13: Creation of doped layers for FinFET Devices

- **[In Progress: Due 12/19/21]** Argonne National Laboratory fabricated a high-Z mask for selective doping and will start new irradiation in June. This time, we also try a mass production of Zn-doped GaN.

M5.6.1 Q10: Characterization of C doping in GaN

- **[In Progress: Due 3/19/21]** The ^{14}C behavior is indirectly studied by various measurements such as the analysis of electrical characteristics.

III Major risks to future milestones

A) ISSUES, RISKS, AND MITIGATION

The main issue this quarter came from the permission to measure our radioactive samples in the other facilities such as Electron Microscopy Core (EMC) facility in UMC. Although GaN irradiated by neutron has very weak radioactivity caused by ^{14}C , the facility does not want to allow the samples to be measured in their space. The cryostat of our DLTS equipment has some problems, so it was shipped to the manufacturer for repair. This leads to a setback for studying carbon behavior and neutron defects.

B) CHANGES IN APPROACH

For better optical imaging and study of crystal defects, scanning electron microscopy (SEM) measurements will be performed after one of the SEM instruments in UMC is moved to MU Research Reactor (MURR). Normally, it would take 2 months to repair the cryostat. To save time, a new cryostat of the DLTS equipment was purchased and will be shipped soon.

ARPA-E SUMMIT Poster with Oak Ridge National Laboratory

For the 2022 ARPA-E Energy Innovation SUMMIT conference, UMC prepared the poster in collaboration with Oak Ridge National Laboratory (ORNL), as shown in Figure 1. The title is ‘selective neutron transmutation doping of GaN’. The main content is to show the achievement of the selective neutron doping with optical images by Scanning Electron Microscopy (SEM), explain how to accomplish the selective doping in ORNL, and compare the electrical characteristics between the exposed area and unexposed area.

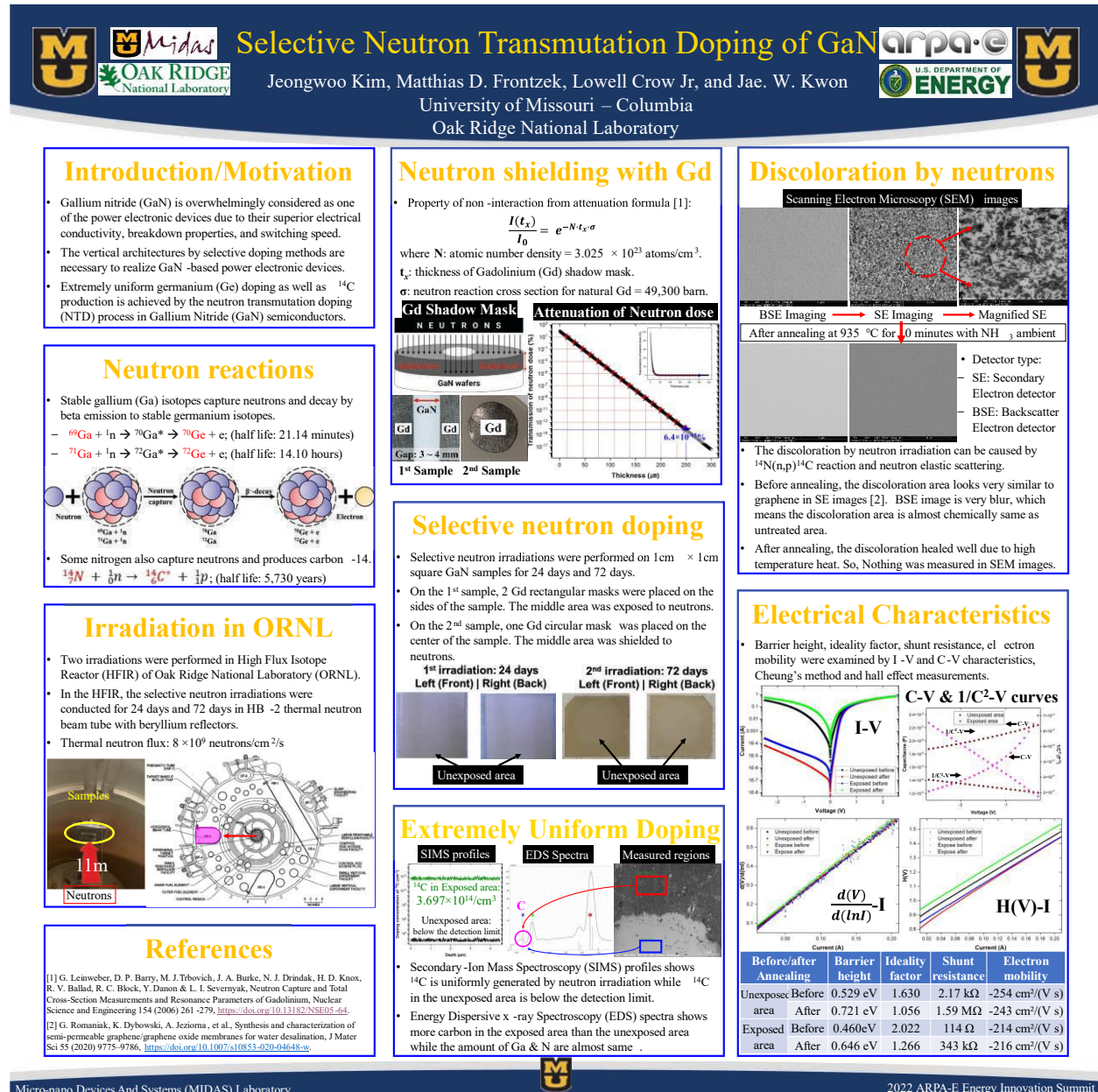


Figure 1. Poster for 2022 ARPA-E Energy Innovation SUMMIT conference.

Neutron shielding with Gd

The attenuation of neutron dose by Gadolinium (Gd) shadow mask is calculated by:

$$\frac{I(t_x)}{I_0} = e^{-N \cdot t_x \cdot \sigma}$$

where $I(t_x)$ is the neutron flux when it penetrates the t_x thickness of the Gd mask, I_0 is the initial neutron flux without any attenuation. N is the atomic number density of natural Gd (3.025×10^{23} atoms/cm³), t_x is the thickness of Gd shadow mask, σ is the neutron reaction cross section for natural Gd (49,300 barn). $I(t_x)/I_0$ is the transmission rate of neutron dose through Gd mask and plotted in Figure 2.

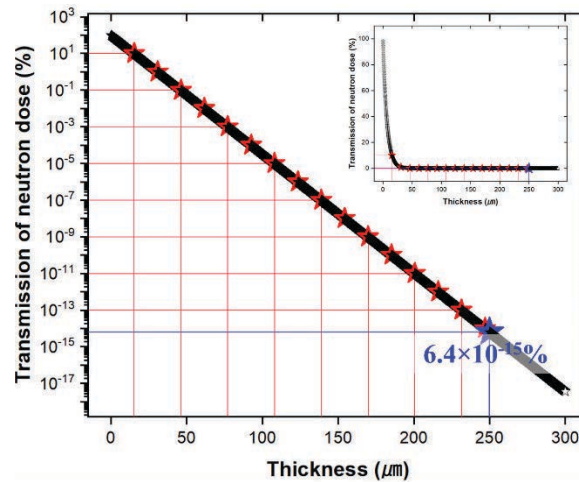


Figure 2. Transmission rate of neutron dose depending on the Gd thickness.

Based on the calculation, over 123 μm thickness of Gd mask can make 10^5 -fold difference. To make a clear difference, we used 250 μm thickness of the Gd mask and guessed the almost perfect neutron shielding.

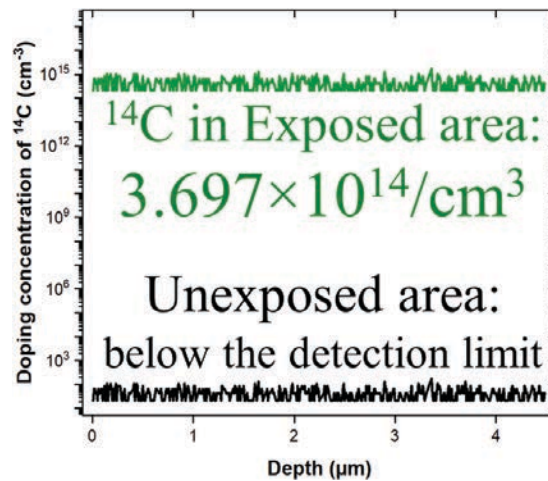


Figure 3. SIMS profile of ¹⁴C in the exposed and the unexposed area.

The Secondary Ion Mass Spectroscopy Mass (SIMS) profile in Figure 3 shows the difference in doping concentration in terms of ^{14}C . The ^{14}C concentration in the exposed area is $3.697 \times 10^{14}/\text{cm}^3$ while the ^{14}C concentration in the unexposed area is below the detection limit.

Scanning Electron Microscopy (SEM) images

The difference between the exposed area and the unexposed area was confirmed by Scanning Electron Microscopy (SEM) images, as shown in Figure 4.

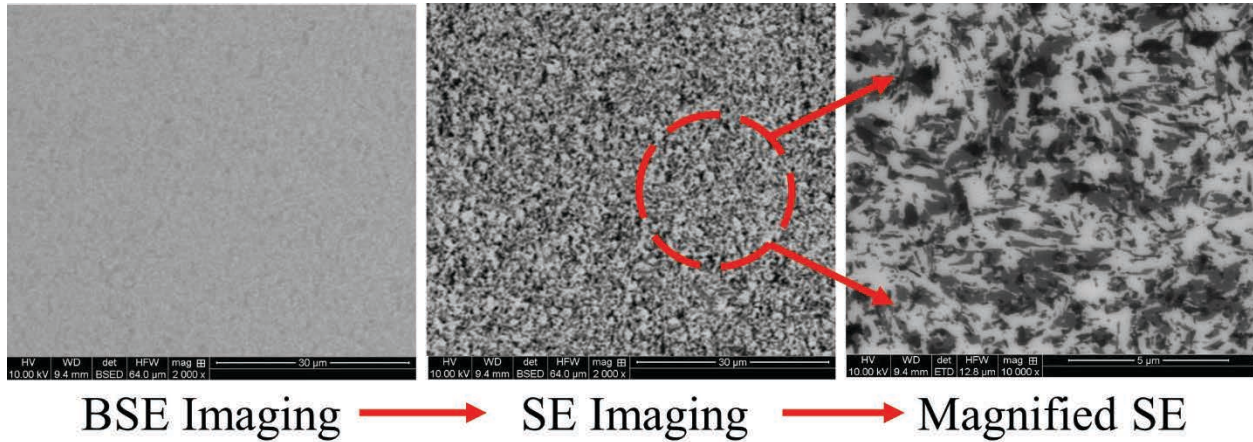


Figure 4. SEM images of the exposed area before annealing.

In the exposed area, some black patterns in Secondary Electron (SE) detector images were detected while nothing was detected in Backscatter Electron (BSE) detector image. The black pattern has very similar chemical properties and is not scratch or organic matter. We guess the pattern is similar to graphene. They may be something related to carbon and neutron defects.

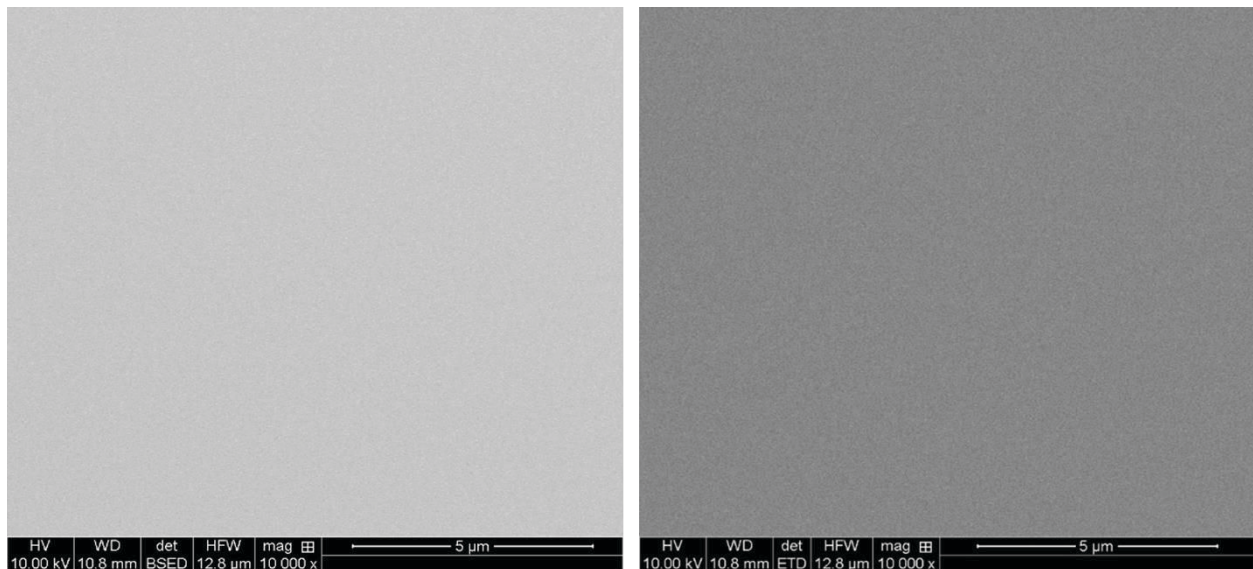


Figure 5. SEM images of the exposed area after annealing. The left is a BSE image, and the right is a SE image. Nothing was detected after annealing.

Interestingly, the black patterns were not detected after annealing, as shown in Figure 5. Needed is a high resolution imaging measurement like Transmission Electron Microscopy (TEM). EMC in UMC is installing a nice TEM now and will run it around June. After the installation, we will try to carry out the TEM measurements on the sample.

Other supportive data that the black pattern relates to carbon is no difference between the SE images regardless of measurement voltage.

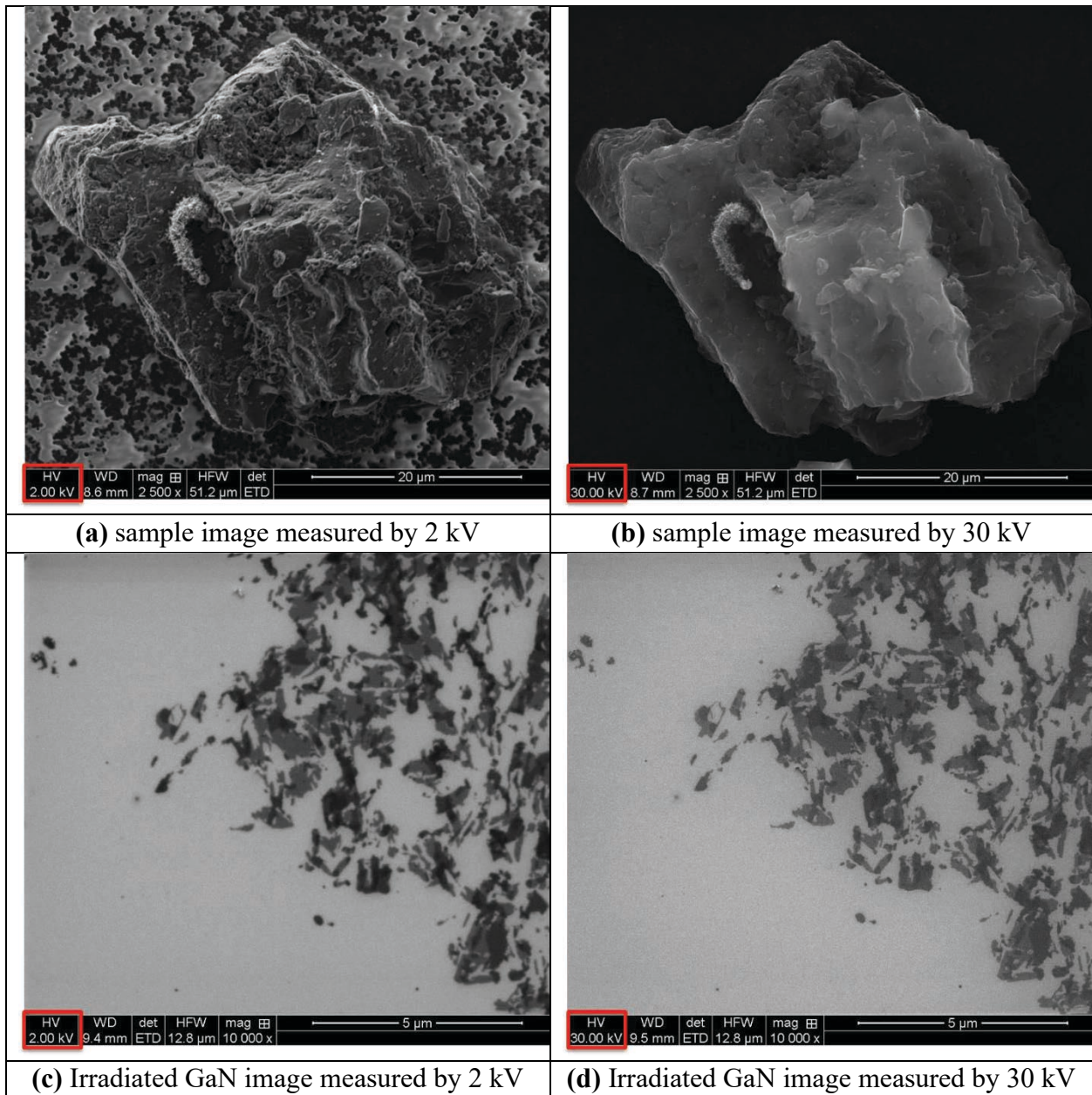


Figure 6. SE images measured with different voltages. (a) and (b) is the sample images to help understand the difference in measurement voltage. (c) and (d) is the images of selectively irradiated GaN.

In Figure 6-(a) and (b), there is a clear difference although (a) and (b) imaged the same material. Based on the mechanism of the SEM technique, high voltage measurement can detect deeper parts of an object. If one object is just a small particle, it will look more transparent with high voltage than low voltage like Figure 6-(b). However, in Figure 6-(c) and (d), there is no difference. That means the black patterns are not just particles but uniformly deposited layers. That is why we suspect that the pattern is ^{14}C uniformly produced by neutrons.

The difference in carbon concentration can be confirmed in Energy Dispersive x-ray Spectroscopy (EDS) spectra, as shown in Figure 7.

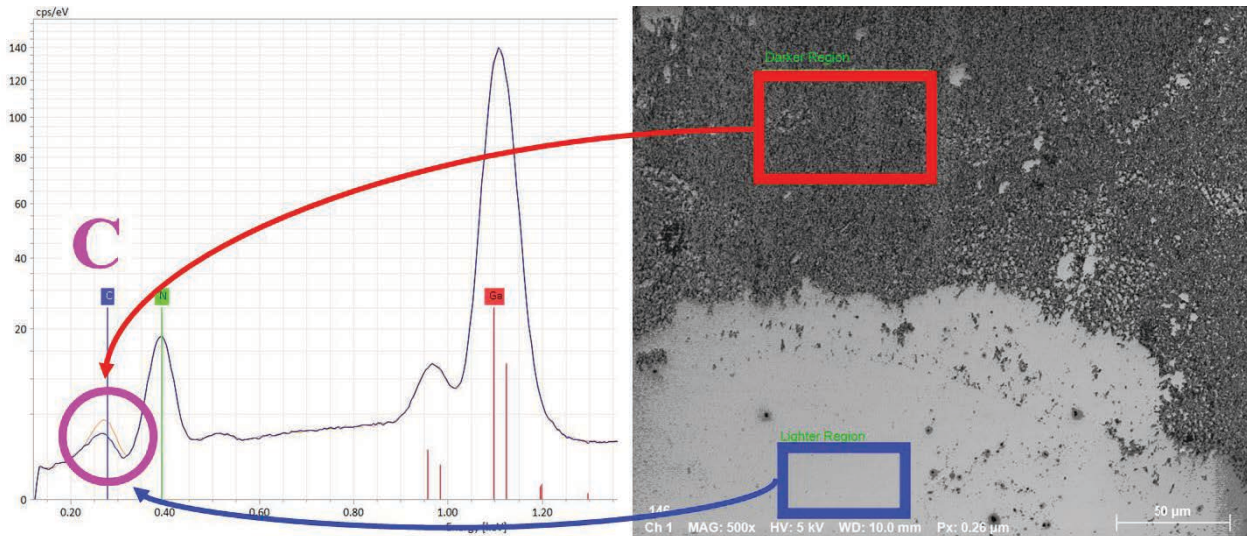


Figure 7. EDS spectra of the exposed and unexposed area. The red box is an exposed area, and the blue box is an unexposed area.

The contents of all materials are almost the same, but there is a difference in carbon concentration. More SEM measurements are needed for long irradiated GaN such as GaN samples irradiated in MURR to confirm which material is the black pattern. If we can compare the difference between SEM images before and after annealing, it will be clear to confirm the material.

Neutron Irradiations in MURR

We completed the mass production of GaN doped by neutron transmutation doping (NTD) process in the reactor of MURR and started measuring the properties of the irradiated from last quarter. The crystal structure and optical properties of the samples were measured by X-Ray Diffraction (XRD) and Photoluminescence (PL) methods. This quarter the electrical properties of the samples were studied with I-V characteristics in terms of Schottky barrier height, ideality factor, and various resistances. For monitoring crystal quality and visualizing defects in annealed GaN, the X-Ray Topography will be performed in collaboration with Stony Brook University.

Annealing and Metal deposition

Samples were irradiated in area C of the reactor in MURR for 5, 25, 75, and 100 hours and are called GR5, GR25, GR75, and GR100. All samples irradiated in area C of the reactor in MURR have no optical and electrical properties before the crystal annealing process. For optical and electrical measurements, the GaN samples irradiated in MURR were annealed for 10 minutes at 935 °C with NH₃ ambient. For the measurements of the electrical characteristics, Pt/Au (80nm/40nm) were deposited on the polished side of samples for Schottky contact, and Ti/Au (30nm/150nm) were deposited on the unpolished side of samples for Ohmic contact. To improve the metal contact, the GaN samples with metal layers were rapidly annealed for 1 minutes at 650°C with N₂ ambient.

Electrical Characteristics: Properties of Schottky Barrier Diode (SBD)

The I-V characteristics of GR5, GR25, GR75, and GR100 were measured on a log scale and linear scale respectively, as shown in Figure 8. In the log scale plot, each sample has a different rectification ratio. As the irradiation time increases, the rectification ratio and leakage current also increase. However, all samples show nice I-V curves in the linear scale plot.

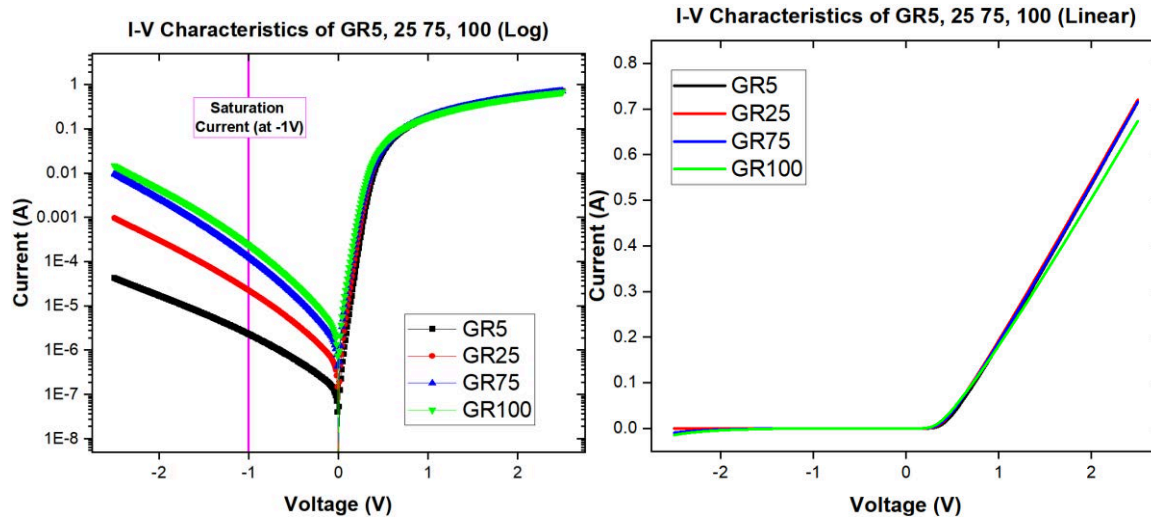


Figure 8. I-V curves of GR5, GR25, GR75, GR100. The left is a log scale I-V curve, and the right is a linear scale I-V curve,

The current through the SBDs at a forward bias ($V \geq 3kT/q$) follows the thermionic emission theory [1] and can be expressed as:

$$I = I_0 \times e^{\frac{qV}{nkT}}$$

$$I_0 = A \times A^{**} \times T^2 \times e^{-\frac{q}{kT}\phi_b}$$

Here, A is the diode area ($5.027 \times 10^{-3} \text{ cm}^2$), A^{**} is the effective Richardson constant ($35 \text{ A}/(\text{cm}^2\text{K}^2)$) [2], T is the absolute room temperature (300 K), q is the charge of an electron ($1.6 \times$

10^{-19} C), k is the Boltzmann's constant (1.381×10^{-23} J/K), ϕ_b is the measured barrier height, n is the ideality factor.

The measured ϕ_b and n are calculated by using the reverse leakage current at -1 V. Shunt resistance (R_{Sh}) of each SBD in Figure 9 was estimated from the junction resistance obtained by $R_j = \frac{\partial V}{\partial i}$ from the I-V characteristics.

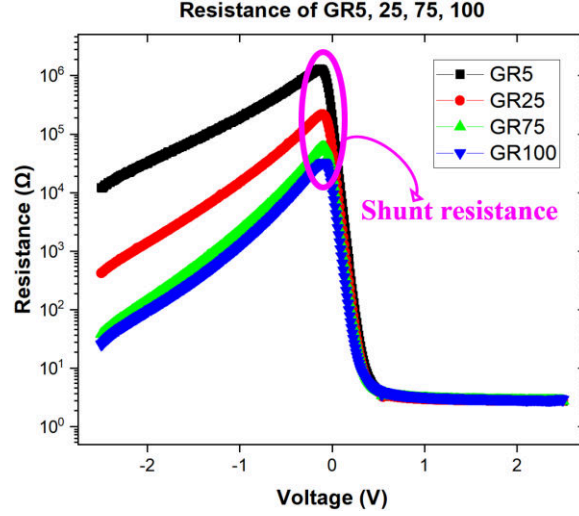


Figure 9. Resistance curves of GR5, GR25, GR75, GR100. The shunt resistance is the peak value of each curve.

The electrical parameters are tabulated in Table 1. The barrier height, ideality factor, and shunt resistance deteriorated as the irradiation time increased. The long irradiation produced more ^{14}C . It is believed that the ^{14}C acts as acceptors and hole traps, which attributes to the increased trap-assisted recombination and the accumulation of holes causing the increased space charge near the junction. The behavior leads to an increase in barrier height and a decrease in ideality factor and shunt resistance.

Table I. Electrical parameters measured or calculated by I-V Characteristics, Cheung's Method, and C-V Characteristics.

Sample	I-V Characteristics With leakage current at -1 V			Cheung's Method			C-V Characteristics From -1 V to 0V	
	Barrier height ϕ_b [eV]	Ideality factor n	Shunt resistance R_{Sh} [Ω]	Barrier height ϕ_b [eV]	Ideality factor n	Series resistance R_s [Ω]	Barrier height ϕ_b [eV]	Carrier Concentration [cm^3]
GR5	0.614	1.466	3.88 M	0.669	1.367	3.912	0.732	-7.447E+17
GR25	0.527	1.744	219 K	0.611	1.400	3.560	0.710	-1.486E+18
GR75	0.488	2.066	65.4 K	0.584	1.433	3.133	0.735	-2.338E+18
GR100	0.474	2.162	37.6 K	0.573	1.524	3.289	0.665	-2.338E+18

Cheung's method was used to determine the barrier height, ideality factor, and series resistance (R_S) of the SBDs in the non-linear forward-bias region of the $\ln I$ -V curve [3]. According to Cheung's functions, each value can be estimated from the following equations:

$$\frac{d(V)}{d(\ln I)} = \frac{kT}{q} \times n + R_S \times I$$

$$H(I) = V - \frac{nkT}{q} \ln\left(\frac{I}{AA^{**}T^2}\right) = I \times R_S + n \times \Phi_b$$

The forward-bias $dV/d(\ln I)$ versus I and $H(I)$ versus I give linear behavior, as presented in Figure 10. The slope and y-axis intercept of $dV/d(\ln I)$ versus I curve give series resistance and ideality factor. Using the ideality factor value calculated from $dV/d(\ln I)$ versus I curve, the barrier height is obtained from the y-axis intercept of $H(I)$ versus I curve. The electrical parameters obtained by Cheung's method are tabulated in Table I.

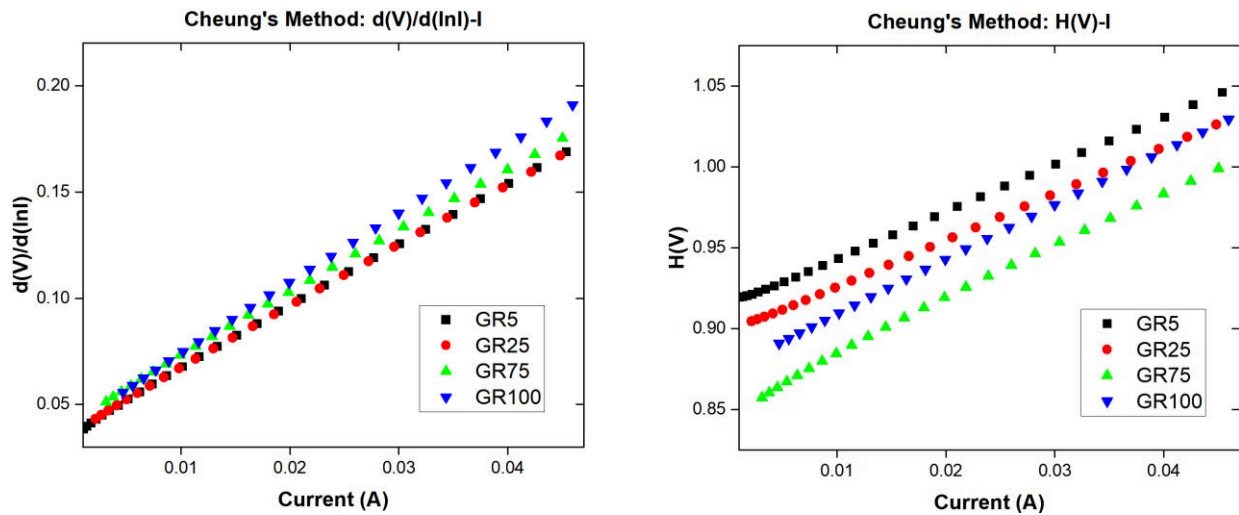


Figure 10. Curves obtained from Cheung's method. The left is a curve of $d(V)/d(\ln I)$ versus I , and the right is a curve of $H(I)$ versus I .

The values of series resistance from both curves are closely matched, implying the consistency and validity of the resistance. The values obtained by Cheung's method are in reasonably good agreement with those obtained by I-V characteristics. The existence of series resistance is considered the main reason. The barrier height and ideality factor obtained by I-V characteristics did not take into account the series resistance. Due to the series resistance, the barrier height and ideality factor calculated by Cheung's functions slightly increased. Like I-V characteristics, the behavior of ^{14}C leads to a higher barrier height and a lower ideality factor. It is speculated that ^{14}C can interfere with the flow of electrons through the recombination of the electron-hole pair.

The capacitance-voltage (C-V) characteristics of the SBDs were measured at a frequency of 1 MHz for barrier height and carrier concentration. Plots of $1/C^2$ -V characteristics for the SBDs are

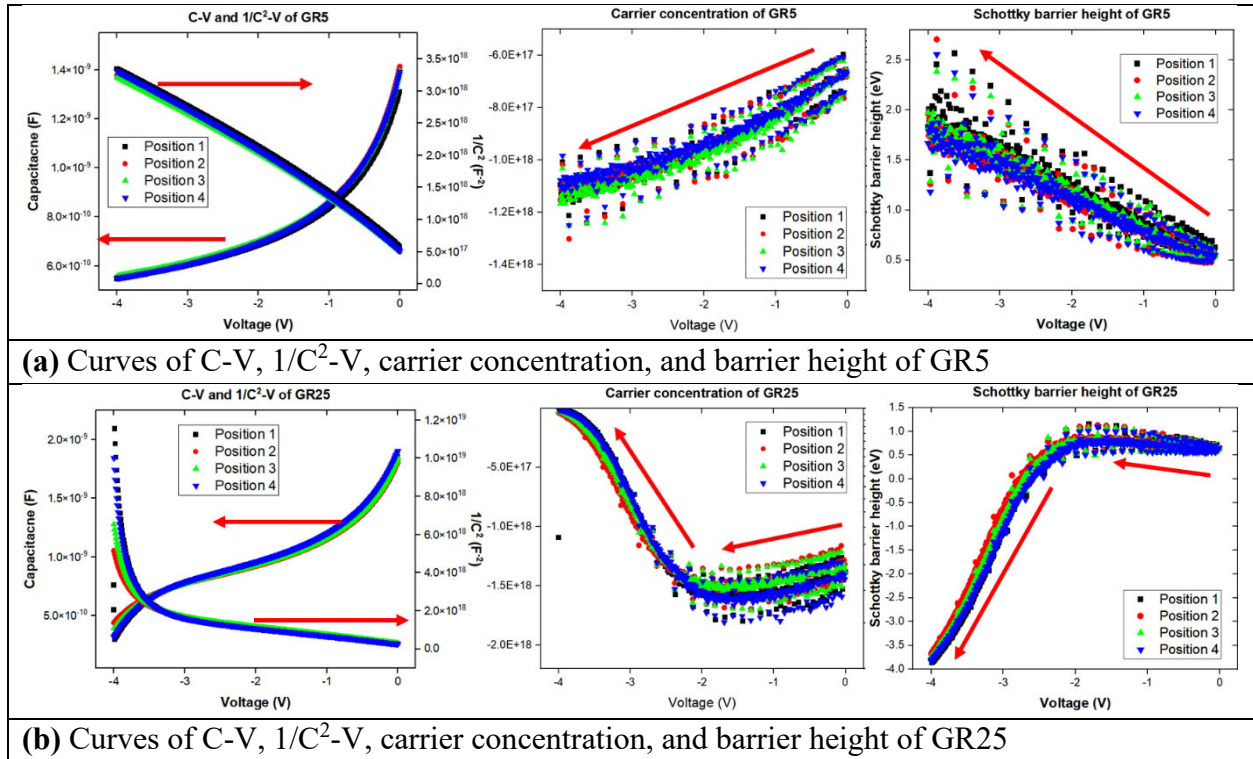
shown in Fig. 11, from which the barrier height and carrier concentration are determined based on the following equations [4]:

$$\Phi_b = V_{bi} + V_P$$

$$\frac{1}{C^2} = \frac{2(V_{bi} - \frac{kT}{q} - V)}{A^2 \times q \times N \times \epsilon_s}$$

$$V_P = \frac{kT}{q} \ln\left(\frac{N_C}{N}\right)$$

where V_{bi} is the built-in potential ($V_{bi} = V_0 + \frac{kT}{q}$), N is the carrier concentration, ϵ_s is the dielectric constant of GaN ($8.9 \epsilon_0 = 7.88 \times 10^{-11} \text{ F}\cdot\text{m}^{-1}$), N_C is the effective conduction band density of states in GaN ($2.3 \times 10^{18} \text{ cm}^{-3}$). V_0 is determined by the x-intercept of the $1/C^2$ versus V curve. Unlike the I-V characteristics and Cheung's method, electrical parameters change with the supplied voltage. Figure 4 shows the C-V, $1/C^2$ -V, carrier concentration, and barrier height of each sample depending on the negative voltage.



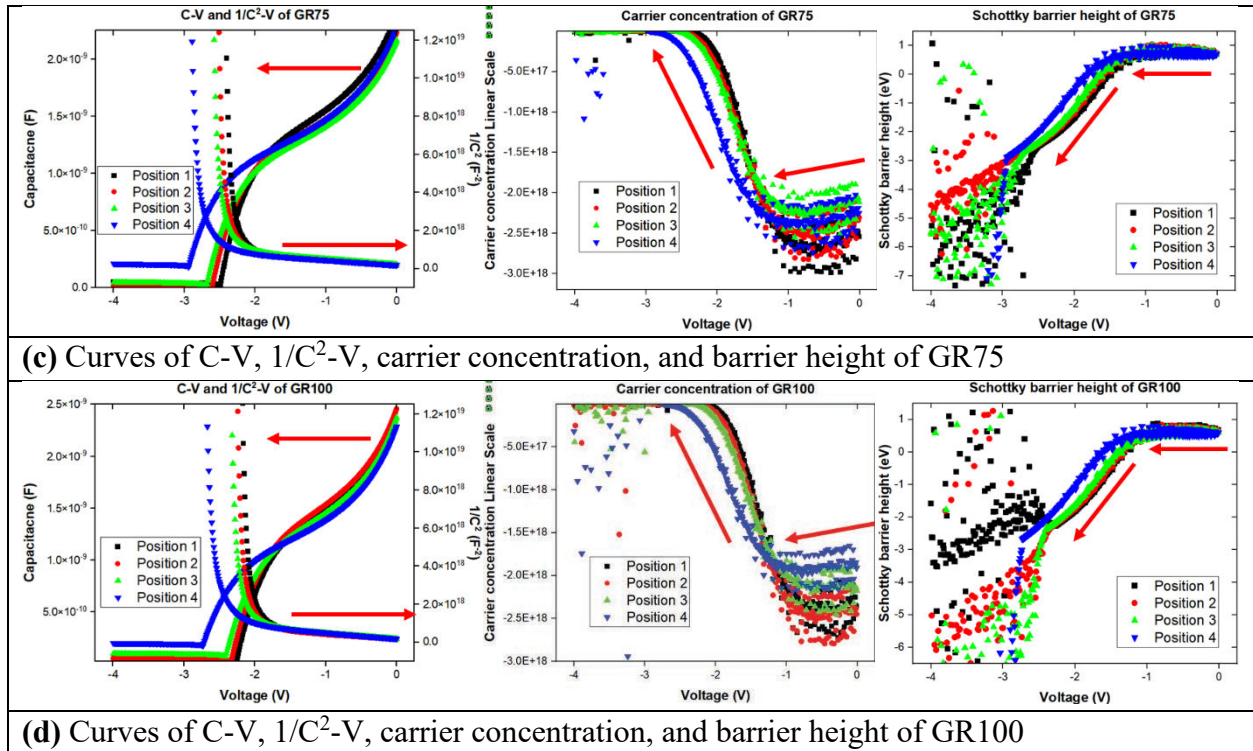


Figure 11. Curves of C-V, $1/C^2$ -V, carrier concentration, and barrier height of GR5, 25, 75, 100.

Except for GR5, the other samples have non-linear $1/C^2$ -V curves. We guess that ^{14}C acts as an acceptor and can be negligible to calculating the doping concentration and barrier height at a high negative voltage. We are working on upgrading the C-V characteristics functions to include the effect of p-type dopants.

If low negative voltage (from 0 to -1V) is only considered, roughly linear $1/C^2$ -V curves can be gained. Within the area, the barrier height values are larger than those calculated by I-V characteristics and Cheung's functions. Some structural, line, or point defects may be produced during neutron irradiation, which contributes to the lateral inhomogeneity at the metal/semiconductor interface.

Directional Photonuclear Irradiations in ANL

New irradiation for high Zn doping concentration

In collaboration with Argonne National Laboratory (ANL), we accomplished to produce Zn in GaN by selective photonuclear transmutation doping (PTD) and found the Schottky metal contact for p-type GaN. However, the Zn concentration was not enough to make sure the Zn properties as a p-type dopant in GaN.

In collaboration with ANL, a more high-power converter and a ring mask were fabricated this quarter. The power improved from 3 kW to 17.5 kW. Also, the distance from the converter was

optimized, and multiple samples will be irradiated together. The production rate and estimated Zn concentration with 40 MeV beam energy is tabulated in Table II.

Table II. PTD irradiation conditions: distance from the converter, beam power, production rate, and estimated concentration.

Mask	Unmasked (new)	Masked (new)	Masked (Last)
Distance from the converter [mm]	12.5	50	Unknown
Beam power [kW]	17.5 kW	17.5 kW	3 kW
Production rate [atoms/cm ³ /sec]	1.925E+11	8.40E+10	1.30E+10
Production rate per hour [/cm ³]	6.93E+14	3.02E+14	4.69E+13
Estimated concentration [/cm ³]	1.66E+17	7.26E+16	1.20E+16

Two new irradiation is scheduled with 6 samples per run. Three will be fully irradiated, and the other will be selectively irradiated. We are working on irradiating more samples together and thinking of coating the samples with metals to prevent contaminations like water or oil. The first irradiation is scheduled for the beginning of June, and second irradiation will be the middle of July.

Publications

“Comparative study on the electrical properties of neutron-irradiated n-GaN Schottky barrier diodes depending on ¹⁴C concentration” is in review.

References

- [1] E.H. Roderick and R.H. Williams, Metal-Semiconductor Contacts (Clarendon: Oxford, 1988), p. 121.
- [2] Kumar, A., Arafin, S., Amann, M.C. et al. Temperature dependence of electrical characteristics of Pt/GaN Schottky diode fabricated by UHV e-beam evaporation. *Nanoscale Res Lett* 8, 481 (2013), <https://doi.org/10.1186/1556-276X-8-481>.
- [3] S.K. Cheung and N.W. Cheung, *Appl. Phys. Lett.* 49, 85 (1986), <https://doi.org/10.1063/1.97359>.
- [4] R.T. Tung, *Phys. Rev. B* 45, 13502 (1992), <https://doi.org/10.1103/PhysRevB.45.13509>.

GaN Doping Through Transmutation Process

Quarterly Project Report

Advanced Research Project Agency – Energy

ARPA-E PNDIODES Program, Program Director: Dr. Isik Kizilyalli

Dec 1, 2021 to April 30, 2022

Date Prepared: 05/01/2022

University of California Santa Barbara (UCSB)

University of Missouri-Columbia (UMC)

Massachusetts Institute of Technology (MIT)



As part of this ARPA-e project, we have worked on developing MBE epitaxy materials and devices for vertical p⁺n GaN diodes. We have achieved progress on epitaxy growth, device development, regrowth studies, as well as transmutation doping of GaN through neutron radiation experiments.

1.1. Vertical GaN Power Devices

(a) Vertical GaN p⁺n Diodes

In this project, we focused on developing vertical GaN p⁺n diodes starting from optimizing epitaxy growth by NH₃MBE and expanding to vertical device fabrication using field management. At first, we aimed to grow high-quality thick epitaxy with low unintentional doping (UID) by performing systematic investigation of growth rate effects on background impurity. The growth rate in NH₃-MBE GaN was varied by changing Ga flux (Ga cell temperature) in Ga-limited growth. We achieved considerably low UID (~low 10¹⁵ cm⁻³) with a high-growth rate (1.4 μm/hr) in NH₃MBE GaN-on-GaN which is promising for high-power vertical GaN power devices (Fig. 1a).

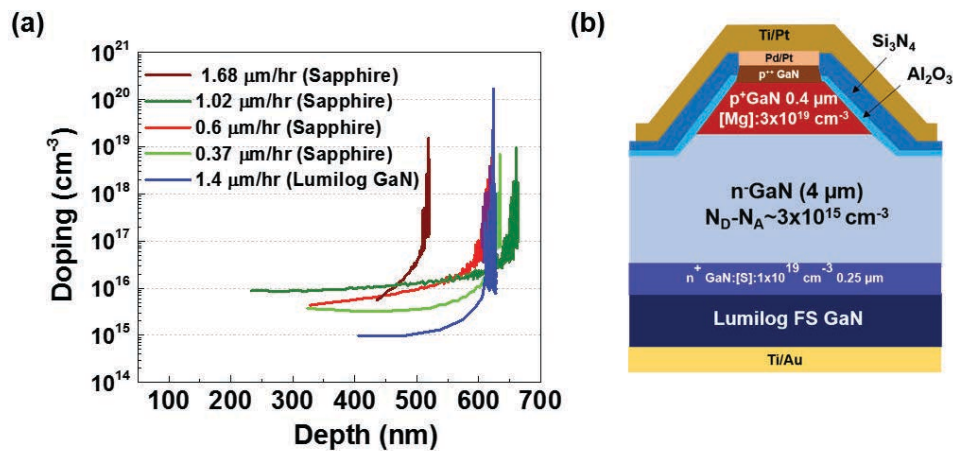


Figure 1. (a) Effects of growth rates on background doping in NH₃MBE GaN (b) Fabricated field-plate vertical GaN p⁺n diode from NH₃-MBE grown epitaxy.

Subsequently, we fabricated vertical p-n GaN diodes using the low UID NH₃-MBE grown epitaxy with field-plates (Fig. 1b). The devices exhibited an outstanding forward J-V behavior with a low specific on-resistance ($R_{on,sp}$) of 0.28 m Ω -cm² and a minimum ideality factor of 1.36. The best diodes also exhibited a breakdown voltage of > 1 kV (equipment limit 1 kV) and a punch-through electric field profile with peak field >2.6 MV/cm. Moreover, these excellent device performance metrics were achieved with a significantly thinner (~4 μ m) drift layer by NH₃MBE compared to the MOCVD GaN p-n diodes of ≥ 8 μ m drift layer thickness that demonstrates the potential of our NH₃ MBE growth for high-voltage p⁺n GaN diode realization.

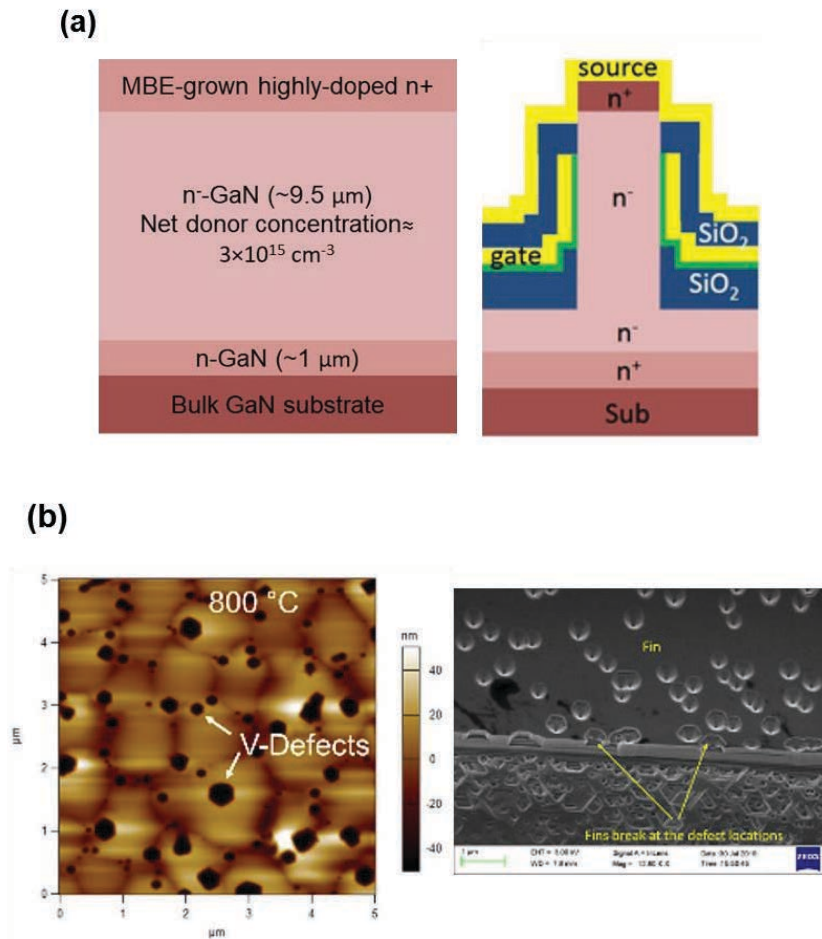


Figure 2. (a) NH₃MBE epitaxy and target Vertical GaN FINFET (b) V-pits observed in the epitaxy

(b) Vertical GaN FinFETs

With collaboration of MIT, we further contributed to the development of advanced vertical GaN FinFETs. Using NH_3 -MBE, we grew $n^+/n^-/n^+$ structures for FinFETs where the n^- GaN drift regions was 10 μm thick UID epitaxy grown at 800 $^\circ\text{C}$ (Fig. 2a). We also performed regrowth n^+ highly-doped MBE GaN to improve source contacts and $R_{\text{on,sp}}$ of the vertical GaN FinFETs. However, the presence of V-defects was observed in the epitaxy (Fig. 2b) that can compromise the device performance.

Through the use of indium as a surfactant, we grew a test structure with a 2 μm thick UID layer with NH_3 flow of 750 sccm, a substrate temperature of 800 $^\circ\text{C}$ and an indium BEP flux of 5×10^{-8} Torr. The schematic and AFM scans for the structures are shown in Figure 3.

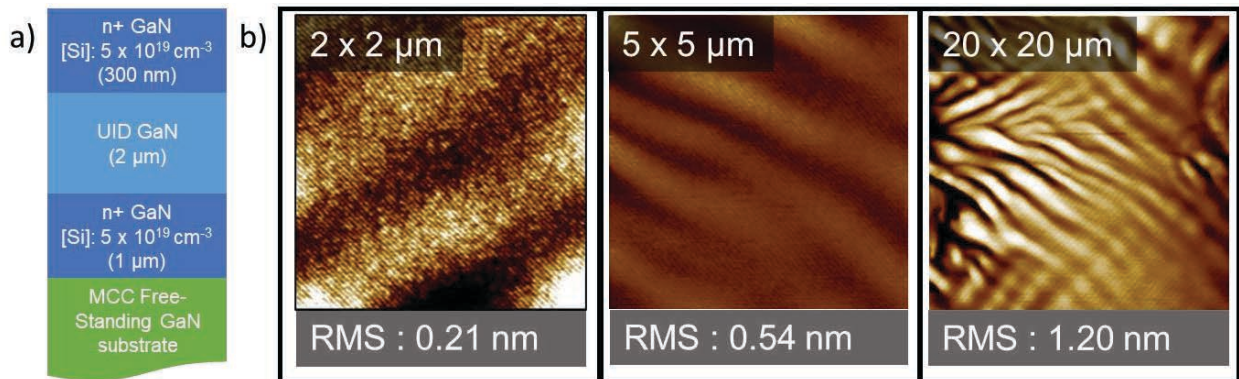


Figure 3. (a) Cross-sectional schematic of the $n^+/n^-/n^+$ vertical FinFET test structure (Sample 5). (b) AFM scans of the surface of the FinFET test structure for different scan sizes, indicating an atomically flat surface.

The AFM data of Figure shows an atomically-flat surface, with a minimum surface RMS roughness of ~ 0.21 nm for small scan sizes. The sample was sent to MIT to be processed into FinFETs for RF.

We then grew the full vertical FinFET structure with the 10 μm thick UID layer using the indium surfactant and optimized conditions. Following the growth, we characterized the film quality using the microscope as well as conducted AFM scans as seen on Figure 4.

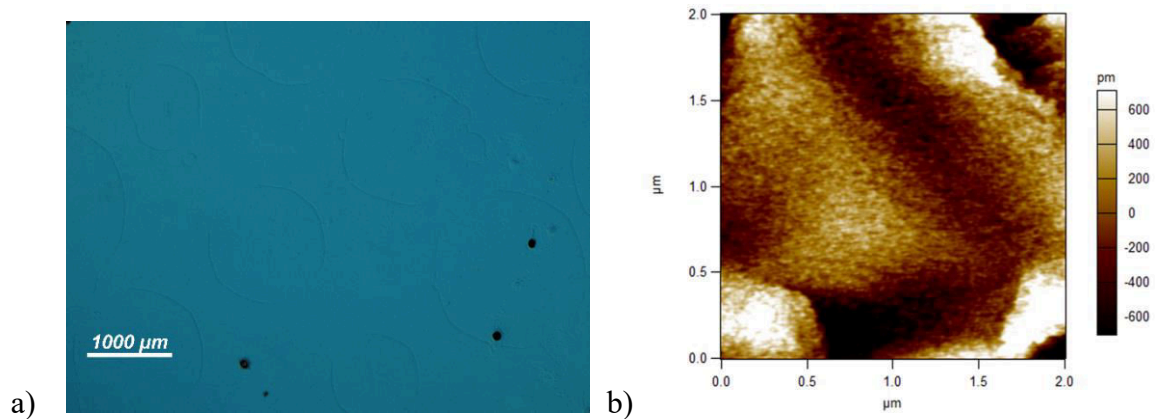


Figure 4 : a) Microscope images and b) AFM scans of the final FinFET structure

Whilst the morphology is slightly degraded when compared to the test structure, we were still able to reduce the V-defect density and improve the surface morphology when compared to the first generation FinFET structure shown in Figure 4. Although the surface was found to be free of cracks, there were circular patterns emerging on the surface. Further studies are required to be determine the origin of these circles. Whilst there were regions that still had some V-defects, there are many regions that were free of them. The sample was then shipped to MIT to be processed into FinFET devices.

1.2. Indium surfactant for morphology and background improvement

For vertical power devices, low unintentional background doping is fundamentally required to achieve high-breakdown voltage. Specially, for punch through p^+n GaN power diodes, low UID is essential to obtain the fully depleted n^- GaN drift layer. Moreover, it is also important to maintain an improved surface morphology during the thick epitaxy growth so that the breakdown voltage is not affected by the leakage current due to poor morphology typically caused by high growth rate.

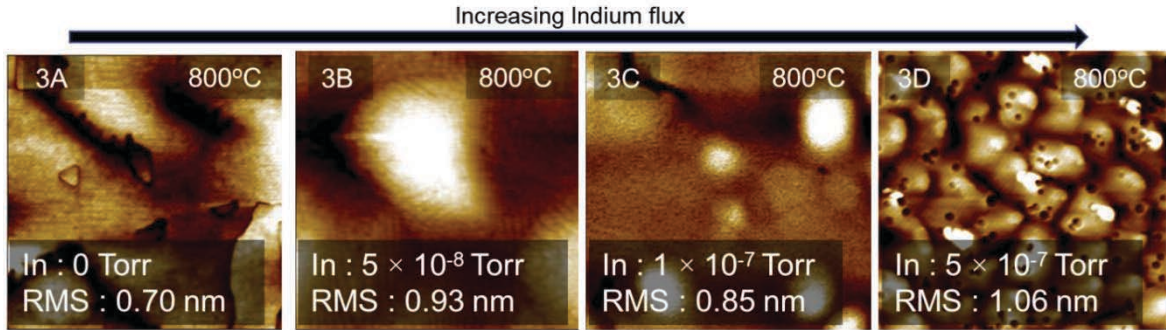


Figure 5. $2 \times 2 \mu\text{m}$ AFM scans for $1 \mu\text{m}$ -thick UID GaN grown under optimized temperature of $800 \text{ }^\circ\text{C}$ and NH_3 flow rate of 750 sccm with indium flux BEPs of (a) 0, (b) 5×10^{-8} Torr, (c) 1×10^{-7} Torr, and (d) 5×10^{-7} Torr.

Toward this goal, we continued to further optimize NH_3MBE growth to achieve both better surface morphology and low unintentional doping using Indium as a surfactant. We performed a systematic study on *c*-plane GaN films growth at high growth rates ($\sim 1 \mu\text{m/hr}$) using a combination of varying V/III ratios, In flux, and growth temperatures. From atomic force microscopy characterization, an optimal condition for surface morphology was achieved for fast growth rates on the order of $1 \mu\text{m/hr}$ and beam equivalent pressure (BEP) on the order of 5×10^{-7} Torr (Fig. 5). However, excessive indium caused the surface morphology to degrade, potentially due to the enhancement of the Ga desorption from the surface as a result of the reaction of indium with ammonia for high indium fluxes.

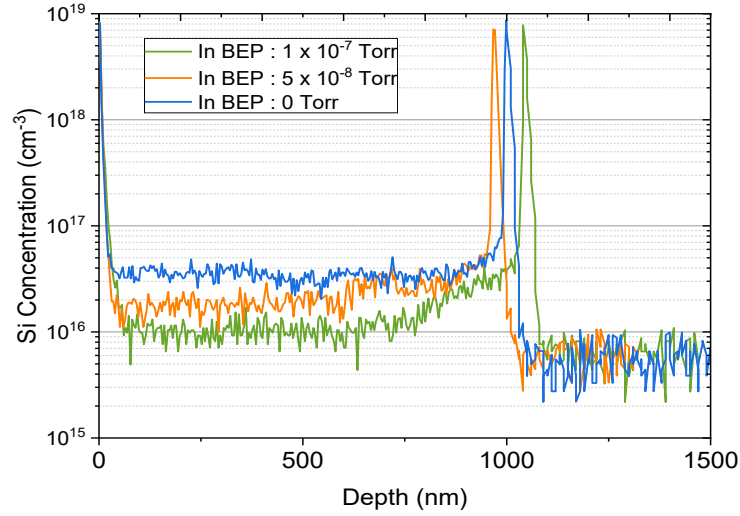


Figure 6. SIMS profiles for (a) Si, (b) In and (c) O for different *In* surfactant flux BEPs of 0, 5×10⁻⁸ and 1×10⁻⁷ Torr.

We also analyzed the effect of unintentional impurity incorporation from Indium surfactant effects using both Secondary ion mass spectrometry (SIMS) and net doping profile from capacitance-voltage measurements. SIMS studies revealed a consistent trend of silicon impurity reduction with Indium surfactant introduction (Fig. 6).

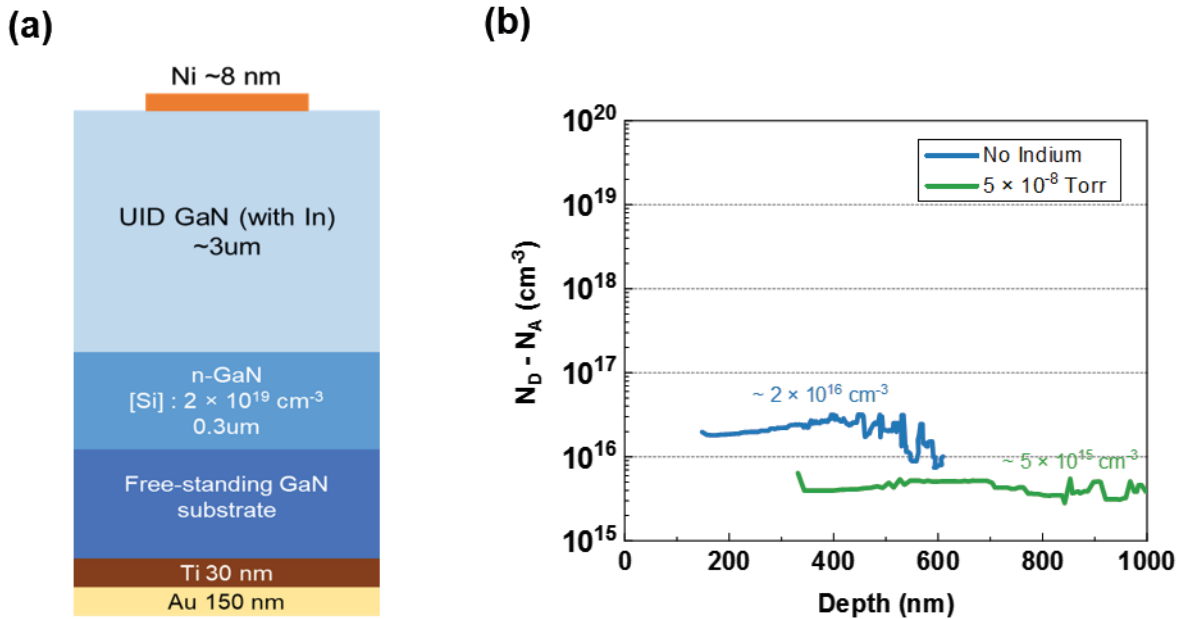


Figure 7. (a) Schematic of the vertical n-GaN diode used for C-V measurements ; (b) dependence of the net doping on depletion depth in the structure to demonstrate the effect of Indium surfactant on unintentional background

Next, to electronically characterize unintentional background doping in these samples, vertical n-GaN Schottky devices were fabricated to perform the capacitance-voltage (C-V) characterization (Fig. 7a). The test structures consisted of a 3 μm layer of UID-GaN followed by 300 nm of n^+ GaN ($[\text{Si}] \sim 5 \times 10^{19} \text{ cm}^{-3}$) on top of a free-standing GaN substrate. The Schottky diodes were fabricated with 8 nm Ni anode contacts and a Ti/Au (30/150 nm) backside ohmic. The 1 MHz C-V measurements also showed a commensurate lower UID in the n-GaN drift layer with Indium surfactant introduction, consistent with the trend of silicon SIMS (Fig. 7b).

1.3. Transmutation doping studies

During this period, we continued our collaboration with University of Missouri on the transmutation doping studies through neutron radiation. For this experiment, two homoepitaxy NH_3 -MBE GaN samples were used that were grown with a 4 μm thick drift layer ($N_D^+ - N_A^-$: $\sim 7 \times 10^{15} \text{ cm}^{-3}$) and 1 μm -thick drift layer on MCC and Lumilog substrates, respectively (Fig. 6). The neutron radiation was performed with multiple time duration to investigate transmutation doping introduction as a function of radiation dose.

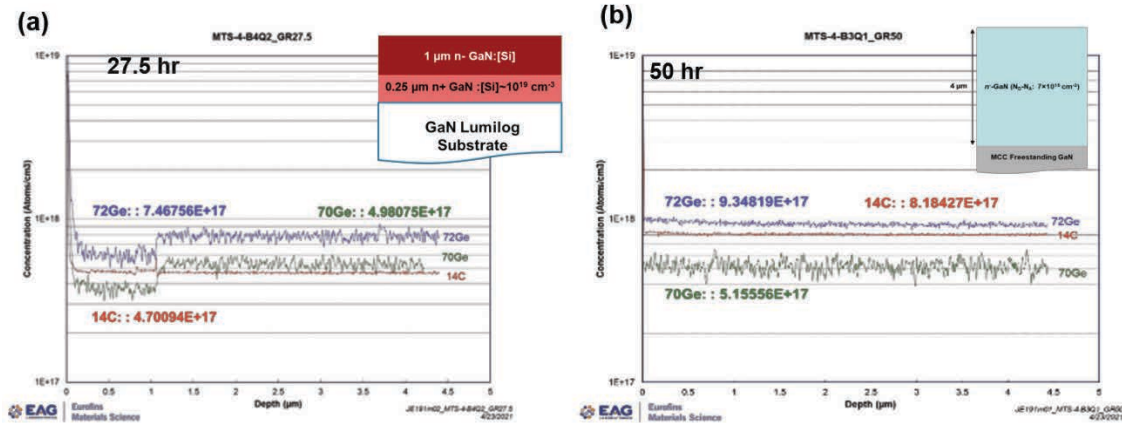


Figure 8. SIMS profile of different elements obtained with neutron exposure of (a) 27.5 hour and (b) 50 hour

From the neutron radiation experiments, we observed a significant increase of ^{14}C and ^{72}Ge isotopes with increasing neutron exposure duration that potentially indicates the N to C and Ga to Ge transmutation. As shown in Fig. 6, the increase of neutron radiation duration from 27.5 hours to 50 hours consistently raised ^{14}C and ^{72}Ge concentration by $3.5 \times 10^{17} \text{cm}^{-3}$ and $1.8 \times 10^{17} \text{cm}^{-3}$, respectively. This also implies that using ^{69}Ga source in GaN growth would not result in such transmutation process from Ga to Ge since the ^{71}Ga source is responsible for ^{72}Ge transmutation.

As the next step to verify this, we planned to pursue growth of GaN using ^{69}Ga source for reducing Ga-to-Ge transmutation by neutron irradiation. For this experiment, we received ^{69}Ga source material with 5N purity (99.999% pure). However, our MBE source material is typically 7N (99.99999%) and contained in double vacuum-sealed to prevent contamination. The as-received ^{69}Ga source has not been compatible to our MBE source purity and preservation requirements. Future efforts will continue to obtain higher purity ^{69}Ga source to satisfy our MBE growth requirements.

1.4. Regrown and Si-dosed experiments

We intended to develop regrowth structures with controllable interface charge density at regrowth interface and resultant increase of background doping from silicon diffusion. To achieve this goal, first, we needed to ensure that we can obtain silicon dosing of similar levels to ambient exposure. Hence, we performed systematic experiments with regrown PA-MBE GaN structures with different intentional Si doses using our dopant Si cell to mimic the silicon contamination of ambient exposure and then moved the sample into the OBS chamber *in situ*. Our results indicate that the interfacial Si comparable to ambient exposure was achieved with controllable Si dosed levels from low- 10^{19} up to 10^{20}cm^{-3} (Fig 7). The intentional Si doses performed with 45 sec, 30

sec, and 15 sec provided a sheet concentration of $8 \times 10^{13} \text{ cm}^{-2}$, $5.3 \times 10^{13} \text{ cm}^{-2}$, and $2.7 \times 10^{13} \text{ cm}^{-2}$, respectively.

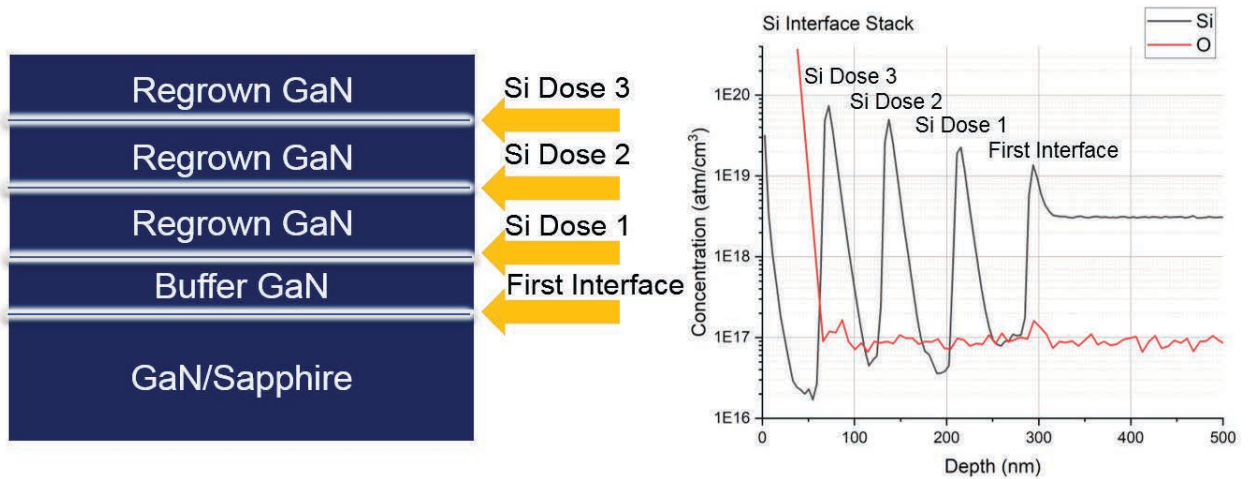


Figure 9. Regrowth structure and SIMS profile for the explored three intentional silicon doses

After obtaining controllable dosing of Si at an interface, it is possible to examine treatment methods at these artificial regrowth interfaces. The current treatment method undergoing exploration is the addition of an oxygen radical source in an effort to form SiO and have the Si desorb from the surface.^{3,4}

To this end, an additional gas treatment chamber was added to the MBE buffer chamber to reduce the risk of contamination of the growth chamber with oxygen. Additionally, an oxygen beam source (OBS) from MBE-Komponenten was installed to supply oxygen radicals to provide active oxygen. This OBS chamber is outfitted with a turbomolecular pump to allow for large gas flows controlled with a leak valve. The sample is heated through a standard Veeco buffer heater system. The maximum temperature of the system is dictated by the maximum heater current of 6 amps, which results in a temperature in excess of 800 °C. However, without cooling, the chamber walls heat up and outgas, so additional fans are fixed on the outside of the chamber to provide some cooling to the system.

The oxidation of Si into either active (SiO) or passive (SiO₂) oxide has been studied extensively and it is understood that higher temperatures and lower oxygen partial pressures favor formation of SiO in an O₂ environment.^{3,4} Starodub et al. show the relevant partial pressure and temperature ranges for these two oxidation states (Fig. 10).

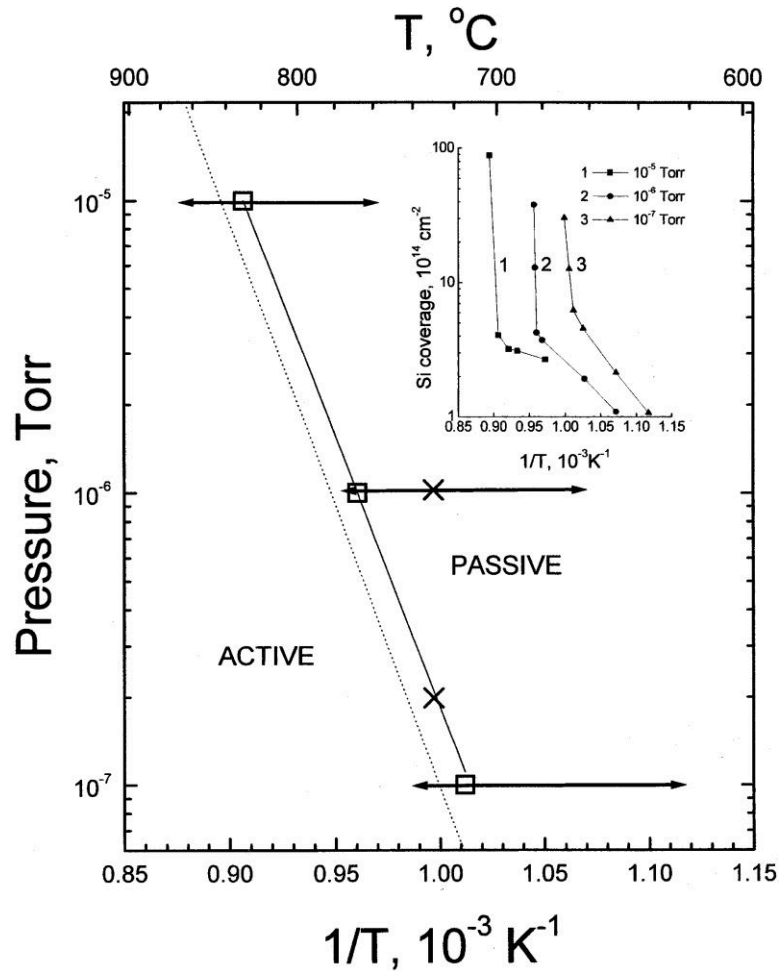


Figure 10. Relevant pressure and temperature ranges for active (SiO) and passive (SiO₂) oxide formation of a Si surface exposed to oxygen.

Naturally, pressure and temperature are the significant parameters when examining the formation of SiO vs. SiO₂. Additionally, the results discussed in Starodub et al. suggest that by decreasing the pressure, the temperature needed for formation of SiO can also be decreased.⁴ As GaN decomposes in vacuum around 720 °C, it is desirable to reduce the temperature to prevent the decomposition of the GaN layer, so pressures on the order of 10⁻⁸ to 10⁻⁷ Torr are desirable.

Although the base pressure of the system was on the order of 5×10^{-10} Torr, the pressure rose to the mid 10^{-8} Torr range due to outgassing from the chamber due to the sample heating. As such, a constant pressure of 1×10^{-7} Torr was chosen with varying sample temperatures and OBS filament temperatures. A summary of the obtained surface concentrations, from SIMS measurements, can be seen in Table 1 below.

Interface Condition	Sheet Concentration (cm ⁻²)	Reference Concentration (cm ⁻²)
650 °C, 1700 °C	3.03×10^{13}	2.95×10^{13}
700 °C, 1700 °C	3.04×10^{13}	2.95×10^{13}
725 °C, 1700 °C	3.66×10^{13}	3.47×10^{13}
750 °C, 1700 °C	2.93×10^{13}	2.63×10^{13}
775 °C, 1700 °C	3.08×10^{13}	2.63×10^{13}
800 °C, 1700 °C	2.70×10^{13}	2.56×10^{13}
800 °C, 1750 °C	2.56×10^{13}	2.54×10^{13}
800 °C, 1800 °C	2.63×10^{13}	2.54×10^{13}

Table 1: Summary of OBS treatment conditions with heater temperature and OBS filament temperature, respectively. Note that all treatments were conducted for 30minutes at a pressure of 1×10^{-7} Torr. The reference concentration was built into the sample and, as such, each value must be compared to its respective reference.

Despite varying temperature of both the OBS source and the sample significantly, it is noted that there was never any decrease in the Si concentration. In fact, in every growth the Si concentration seems to increase for each subsequent interface. As this is a consistent phenomenon, it is expected that there is something affecting either the measurement or the experiment. As SIMS should have depth resolution such that the ~ 100 - 200 nm spacer layers such that the interfaces do not interact, it was considered that there was some other source of Si depositing on the sample surface. In order to investigate this, a sample with no intentional Si

contamination was examined. For this sample, three separate conditions were examined: 1) removing the sample from the growth environment into the OBS chamber for the duration of a treatment step (30 minutes) without any treatment (no O₂ or heat), 2) placing the sample in the OBS chamber for 30 minutes with heat on both the heating stage (800 °C) and the OBS filament (1800 °C) (to simulate proper heating during a treatment) but without O₂ flow, 3) a full treatment step with heat and O₂ flow (1×10^{-7} Torr). The resulting SIMS profile can be seen below (Fig 9).

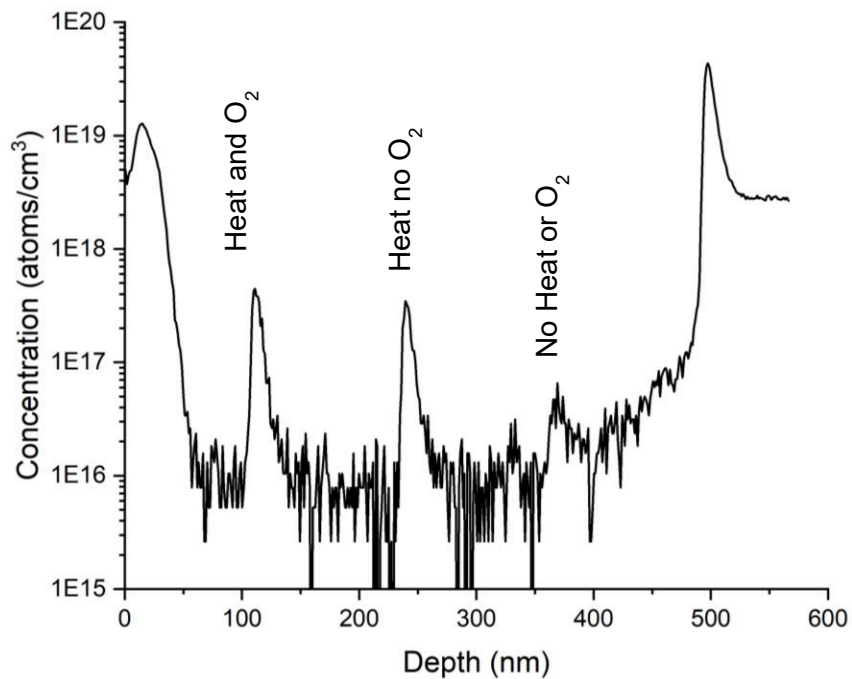


Figure 11. Si profile obtained from SIMS for the Si contamination sample.

It is immediately obvious that there is a significant increase in the sheet concentration for the interfaces included heat on the sample and the OBS as compared to the sample that of the one without any heat or O₂ flow. The sheet concentrations of Si at these peaks were obtained by integrating the peaks and the resulting concentrations are show in Table 2.

Interface Condition	Sheet Concentration (cm ⁻²)
Heat and O ₂	4.38×10 ¹¹
Heat no O ₂	3.25×10 ¹¹
No heat or O ₂	1.05×10 ¹¹

Table 2: Sheet concentrations of Si obtained from peak integration of the SIMS profile of Fig 11.

Again it is apparent that without the heat and O₂ flow, there is significantly less Si observed than in the cases where the sample was heated. Additionally, it is evident that the top interface, the one with heat and O₂ flow has the highest sheet concentration of Si. The natural question, however, is where does this Si come from? The answer is expected to be simple: the plasma assisted MBE samples are often 10×10 mm² samples bonded to a 3" Si carrier wafer with In, as seen below (Fig 12).

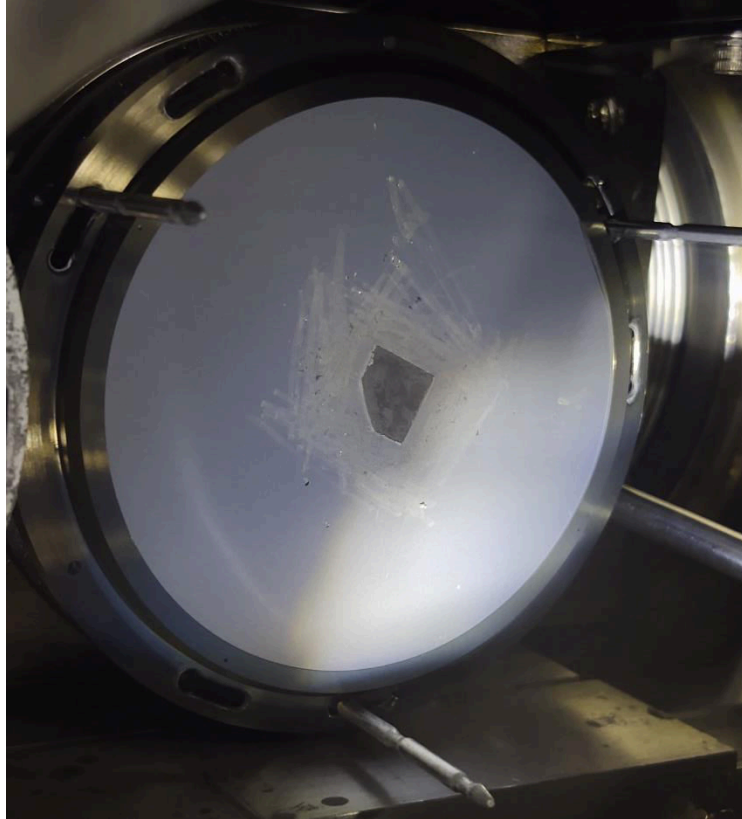


Figure 12. $\sim 10 \times 10 \text{ mm}^2$ sample bonded to a 3in. Si carrier wafer with In bonding for loading in a standard Veeco GEN-II block. Note that the discoloration around the sample is from removing excess In from the bonding process.

It is expected that these unpolished Si wafers still have the standard native SiO_2 on the surface when the samples are loaded into the system. As such, heating them up in vacuum to temperatures on the order of $800 \text{ }^\circ\text{C}$ is expected to produce some SiO_2 decomposition into SiO .³ So, the samples that were heated saw the SiO desorb off the surface of the Si wafer, but then be redirected toward the sample surface by the heated OBS source. As such, it is expected that removing this Si wafer may result in removal of the unintentional Si contamination of all the experiments thus far. Additionally, these results suggest that Si is successfully moving from one surface to another under these conditions. As such, it may be possible to see movement of Si from the intentionally contaminated surfaces, provided that the unintended additional Si contamination is dealt with.

References

- [1] J. Wang, K. Jorgensen et al. *APL Mater.* **9**, 081118 (2021)
- [2] E. Farzana et al, *IEEE Electron Device Lett.* **41 (12)**, 1806 (2020).
- [3] M. P. D'Evelyn et. al. *Surf. Sci.* **186**, 75-114. (1987).
- [4] D. Starodub et al. *Surf. Rev. Lett.* **6**, 45 (1999).

Schedule - Updates

WBS	Task Name	Mile-stone	Baseline Start	Baseline End	Actual Start	Actual End	% Comp
1	Development of work plan		9/20/2017	12/19/2017			100%
└ M1.1	Q1: Work plan finalized	▼	12/19/2017	12/19/2017			100%
2	Neutron activation of Ge dopants in GaN wafers		9/20/2017	6/19/2018	9/20/2017	4/30/2019	100%
└ 2.1	Establish irradiation protocol		9/20/2017	12/19/2017	9/20/2017	12/31/2017	100%
└ 2.2	Scoping experiments		9/20/2017	6/19/2018	11/12/2017	6/30/2018	100%
└ 2.3	C14 reduction scoping experiments		3/20/2019	12/19/2019	3/20/2019	12/19/2019	100%
└ 2.4	PhotonuclearScopingexperiments		3/20/2019	12/19/2020	10/17/2019		70%
└ 2.5	Development ofmasks fortransmutationdoping		9/20/2019	6/19/2020	10/2/2019		50%
└ 2.6	Masking Scoping Experiments		12/20/2019	9/19/2020	12/20/2019		30%
└ 2.7	Doping of mono-isotope GaN		9/20/2019	12/19/2020	8/15/2019		25%
└ M2.1.1	Q1: Establish wafer supply chain	▼	12/19/2017	12/19/2017	9/20/2017	11/30/2017	100%
└ M2.2.1	Q3: Consistent doping concentration	▼	6/19/2018	6/19/2018	1/2/2018	6/30/2018	100%
└ M2.3.1	Q9: Consistentdopingconcentration	▼	12/19/2019	12/19/2019	8/20/2019	12/19/2019	100%
└ M2.4.1	Q10: Consistentdopingconcentration	▼	6/19/2020	6/19/2020	6/8/2020		80%
└ M2.5.1	Q10: Maskingmaterial fortransmutationdoping.	▼	3/19/2020	3/19/2020	6/8/2020		80%
└ M2.6.1	Q12: Linear selective doped GaN	▼	3/19/2020	9/19/2020	10/8/2019		80%
3	Characterization of GaN wafers doped by neutron transmutation		12/20/2017	12/19/2020	12/11/2017	4/30/2019	100%
└ 3.1	Impurity analysis		12/20/2017	3/19/2020	1/8/2018	12/31/2018	100%
└ 3.2	Crystallinity analysis		12/20/2017	6/19/2020	2/6/2018	12/31/2018	100%
└ 3.3	Electrical analysis		12/20/2017	12/19/2020	12/11/2017	6/30/2019	100%
└ 3.4	Electricalanalysis ofselective doping		12/20/2019	12/19/2020	10/8/2019		60%
└ M3.3.1	Q4: Consistent carrier concentration	▼	9/19/2018	9/19/2018			100%
└ M3.3.2	Q10: Consistent n-type carrier concentration	▼	3/19/2020	3/19/2020	10/2/2019	6/30/2020	100%
└ M3.3.3	Q11: Consistentp-type behavior	▼	6/19/2020	6/19/2020	6/1/2020		65%
└ M3.4.1	Q13: Consistent vertical doping	▼	12/19/2020	12/19/2020	6/1/2020		90%
4	Technology To Market		9/20/2017	12/19/2020	10/2/2017	6/30/2019	100%
└ 4.1	Invention disclosures and patent applications		9/20/2017	12/19/2020	10/2/2017	6/30/2019	100%
└ 4.2	Publications and Presentations		3/20/2018	12/19/2020		6/30/2019	90%

DE-AR0000874 : University of Missouri - Kwon
 Q2 of FY 2022: January 1, 2022 - March 31, 2022

WBS	Task Name	Mile- stone	Baseline Start	Baseline End	Actual Start	Actual End	% Comp
└ M4.1.1	Q1: Background IP report	▼	12/19/2017	12/19/2017	10/2/2017	12/31/2017	100%
└ M4.2.1	Q4: Presentation / Publication	▼	9/19/2018	9/19/2018	3/13/2018	6/30/2019	90%
└ M4.1.2	Q4: IP Update	▼	9/19/2018	9/19/2018		6/30/2019	100%
└ M4.1.3	Q13: IP Update	▼	12/19/2020	12/19/2020			75%
└ M4.2.1	Q4: Presentation/Publication	▼	9/19/2018	9/19/2018			100%
└ M4.2.2	Q13:Presentation /Publication	▼	12/19/2020	12/19/2020			40%
5	Collaboration Work		9/20/2019	12/19/2020	9/20/2019		60%
└ 5.1	Epi-layer growthfor a drift layer		3/20/2020	9/19/2020	2/20/2020		70%
└ 5.2	Doping processfor a drift layer		3/20/2020	9/19/2020	3/12/2020		70%
└ 5.3	Vertical GaNdevice creation		3/20/2020	12/19/2020			30%
└ 5.4	Determineirradiationparameters forcarbon behaviorstudy		6/20/2019	3/19/2020			70%
└ 5.5	Irradiation ofcarbon behaviorstudy		9/20/2019	3/19/2020	9/20/2019		80%
└ 5.6	ElectricalCharacterizationof the carbonbehavior study		9/20/2019	6/19/2020	9/20/2019		60%
└ M5.2.1	Q13: Creation ofdoped layers forFinFET Devices	▼	12/19/2020	12/19/2020			10%
└ M5.6.1	Q10:Characterization of Cdoping in GaN	▼	3/19/2020	3/19/2020	1/3/2020		85%

Additional Performance Updates

A) ISSUES, RISKS, AND MITIGATION

N/A

B) CHANGES IN APPROACH

N/A

C) CHANGES IN PROJECT PERSONNEL

N/A

Technology To Market (T2M)

A. PUBLICATIONS

N/A

B. OTHER PROJECT OUTPUT

N/A

C. FOLLOW-ON FUNDING

N/A

Administrative and Legal Updates

DISCLOSURES

N/A

DE-AR0000874 : University of Missouri - Kwon
Q2 of FY 2022: January 1, 2022 - March 31, 2022

Cost Updates - LEAD: University of Missouri (DE-AR0000874)

High quality GaN FETs through transmutation doping and low temperature processing

ARPA-E RECORDS ONLY (invoices edited by performer are highlighted)

Invoice #	Date	Total	Federal Share	Performer Share	Shortpays	TT&O	Personnel	Fringe Benefits	Travel	Equipment	Supplies	Contractual	Construction	Other	Indirect
AR0000874-GM00229819	2/27/2018	\$40,310.60	\$40,310.60	\$0.00	\$0.00	\$0.00	\$8,509.26	\$1,309.43	\$1,528.27	\$0.00	\$14,659.84	\$0.00	\$0.00	\$0.00	\$14,303.80
AR0000874-GM00231274	3/27/2018	\$21,222.09	\$5,722.09	\$15,500.00	(\$263.50)	\$0.00	\$2,618.26	\$332.31	\$0.00	\$0.00	\$0.00	\$0.00	\$0.00	\$16,431.45	\$1,840.07
AR0000874-GM00232388	4/30/2018	\$9,422.99	\$9,422.99	\$0.00	\$0.00	\$0.00	\$3,168.69	\$374.41	\$0.00	\$0.00	\$374.91	\$0.00	\$0.00	\$2,161.32	\$3,343.66
AR0000874-GM00233996	6/7/2018	\$8,724.82	\$8,724.82	\$0.00	\$0.00	\$2,085.77	\$3,168.71	\$374.42	\$0.00	\$0.00	\$0.00	\$0.00	\$0.00	\$2,085.77	\$3,095.92
AR0000874-GM00235448	7/20/2018	\$9,089.15	\$9,089.15	\$0.00	\$0.00	\$1,937.57	\$3,127.61	\$425.93	\$0.00	\$0.00	\$372.86	\$0.00	\$0.00	\$1,937.57	\$3,225.18
AR0000874-GM00236640	8/14/2018	\$45,587.09	\$45,587.09	\$0.00	\$0.00	\$48.00	\$16,502.64	\$4,881.20	\$0.00	\$10,282.15	\$0.00	\$0.00	\$0.00	\$2,160.00	\$11,761.10
AR0000874-GM00237640	8/29/2018	\$34,932.69	\$34,932.69	\$0.00	\$0.00	\$0.00	\$2,381.86	\$299.67	\$0.00	\$0.00	\$19,855.69	\$0.00	\$0.00	\$0.00	\$12,395.47
AR0000874-GM00238852	10/8/2018	\$6,732.34	\$6,732.34	\$0.00	\$0.00	\$0.00	\$3,230.04	\$385.75	\$0.00	\$0.00	\$727.65	\$0.00	\$0.00	\$0.00	\$2,388.90
AR0000874-GM00240232	10/22/2018	\$5,755.26	\$5,755.26	\$0.00	(\$168.95)	\$0.00	\$2,386.43	\$143.71	\$1,149.17	\$0.00	(\$198.50)	\$0.00	\$0.00	\$360.00	\$1,914.45
AR0000874-GM00243994	1/31/2019	\$43,861.54	\$43,861.54	\$0.00	\$0.00	\$0.00	\$10,112.04	\$701.38	\$1,121.71	\$0.00	\$16,222.20	\$0.00	\$0.00	\$140.42	\$15,563.79
AR0000874-GM00244762	2/26/2019	\$6,964.77	\$6,964.77	\$0.00	\$0.00	\$0.00	\$2,992.78	\$190.10	\$0.00	\$0.00	\$1,310.51	\$0.00	\$0.00	\$0.00	\$2,471.38
AR0000874-GM00246042	3/28/2019	\$27,134.98	\$27,134.98	\$0.00	\$0.00	\$0.00	\$2,993.04	\$190.19	\$0.00	\$0.00	\$12,663.07	\$0.00	\$0.00	\$2,573.20	\$8,715.48
AR0000874-GM00248162	5/3/2019	\$4,934.46	\$4,934.46	\$0.00	\$0.00	\$0.00	\$2,993.27	\$190.25	\$0.00	\$0.00	\$0.00	\$0.00	\$0.00	\$0.00	\$1,750.94
AR0000874-GM00251770	8/27/2019	\$62,855.00	\$62,855.00	\$0.00	\$0.00	\$1,090.00	\$26,984.35	\$8,264.43	\$0.00	\$0.00	\$1,431.81	\$0.00	\$0.00	\$4,784.07	\$21,390.34
AR0000874-00057744NOV2020	12/21/2020	\$838,956.61	\$786,102.23	\$52,854.38	(\$344.10)	\$3,992.55	\$116,872.38	\$33,492.03	\$1,214.35	\$100,400.00	\$62,739.47	\$346,468.11	\$0.00	\$27,118.99	\$150,651.28
AR0000874-00057744DEC2020	2/1/2021	\$41,705.73	\$30,748.04	\$10,957.69	\$0.00	\$0.00	\$7,726.04	\$2,479.27	\$0.00	\$0.00	\$141.08	\$25,668.83	\$0.00	\$0.00	\$5,690.51
AR0000874-00057744FEB2021	3/25/2021	\$120,423.10	\$117,245.21	\$3,177.89	(\$263.50)	\$0.00	\$8,120.20	\$2,500.56	\$0.00	\$0.00	\$3,216.97	\$97,797.85	\$0.00	\$759.20	\$8,028.32

DE-AR0000874 : University of Missouri - Kwon
 Q2 of FY 2022: January 1, 2022 - March 31, 2022

ARPA-E RECORDS ONLY (invoices edited by performer are highlighted)

Invoice #	Date	Total	Federal Share	Performer Share	Shortpays	TT&O	Personnel	Fringe Benefits	Travel	Equipment	Supplies	Contractual	Construction	Other	Indirect
Total:		\$1,328,613.22	\$1,246,123.26	\$82,489.96	(\$1,040.05)	\$9,153.89	\$223,887.60	\$56,535.04	\$5,013.50	\$110,682.15	\$133,517.56	\$469,934.79	\$0.00	\$60,511.99	\$268,530.59
% Expended in Budget Category:		57.67%	57.75%	56.54%		12.35%	82.97%	80.58%	151.92%	55.27%	52.66%	51.75%	0.00%	33.94%	63.89%
Remaining:		\$975,236.78	\$911,825.74	\$63,411.04		\$64,983.08	\$45,957.40	\$13,625.96	(\$1,713.50)	\$89,578.85	\$120,049.44	\$438,141.21	\$0.00	\$117,804.01	\$151,793.41

Overall Proposed Cost Share: 6.33 % Invoiced Cost Share to Date: 6.21 % Proposed TT&O to Federal Share: 3.44 % Actual TT&O to Federal Share: 0.73 %

Agree that the information provided is accurate and correct: Yes No

DE-AR0000874 : University of Missouri - Kwon
Q2 of FY 2022: January 1, 2022 - March 31, 2022

Cost Updates - SUB: Argonne National Laboratory (18/CJ000/01/05)

High Quality GaN FETs through transmutation doping and low temperature processing

N/A

Certification of Compliance

I certify that I have the authority to make the following certification and to submit this Research Performance Progress Report on behalf of the Prime Recipient. On behalf of the Prime Recipient, I further certify that the information provided in this Research Performance Progress Report is accurate and complete as of the date shown below. I understand that false statements or misrepresentations may result in civil and/or criminal penalties under 18 U.S.C. § 1001.

Signature: Jae W Kwon

Submitted by: Prof. Jae Kwon (kwonj@missouri.edu), University of Missouri

Submitted Date: 5/2/2022 3:25:43 PM

II Bulleted list summarizing milestones due:

Milestones DUE Q4FY21

2.6 Masking Scoping Experiments

- **[In Progress: Due 9/19/21]** The collaboration with Oak Ridge National Laboratory has been significantly delayed due to the overload caused by COVID.

2.7 Doping of mono-isotope GaN

- **[In Progress: Due 12/19/21]** ^{69}GaN material was shipped to UCSB last quarter. UCSB is working on fabricating ^{69}GaN .

3.3.3 Q11: Consistent p-type behavior

- **[In Progress: Due 6/19/21]** The good Schottky contact metal for Zn-doped p-type GaN was finally found. Through Deep-Level transient spectroscopy, energy diagram analysis like activation energy will be performed on the Zn doped p-type GaN.

5.4 Determine irradiation parameters for carbon behavior study

- **[In progress: Due 3/19/21]** This milestone has received delays due to the busy situation at Oak Ridge National Laboratory. We purchased new GaN wafers with low-conductivity epitaxial layers. The wafers will be irradiated in the MU reactor soon.

M5.2.1 Q13: Creation of doped layers for FinFET Devices

- **[In Progress: Due 12/19/21]** Argonne National Laboratory is working on fabricating a high-Z mask and expects to get the mask in mid-February.

M5.6.1 Q10: Characterization of C doping in GaN

- **[In Progress: Due 3/19/21]** GaN samples with Si-doped epitaxial layers from UCSB and n-type GaN samples with very low Ge doped epitaxial layers from manufacture 3 are irradiated in MURR. The ^{14}C behavior is indirectly characterized by various measurements.

III Major risks to future milestones

A) ISSUES, RISKS, AND MITIGATION

The main issue this quarter came from the delay in the collaboration with Oak Ridge National Laboratory due to their busy schedules. New irradiations, XRD measurements, neutron shadow mask with Gd, and new irradiation position testing were postponed. This leads to a setback for the study of carbon behavior and neutron crystal defect.

B) CHANGES IN APPROACH

GaN samples with Si-doped epitaxial layers fabricated from UCSB were irradiated in the MU reactor and will be shipped to MU very soon. Furthermore, GaN samples with low-conductivity epitaxial layers are in the process of irradiation in the MU reactor.

Neutron Irradiations in MURR

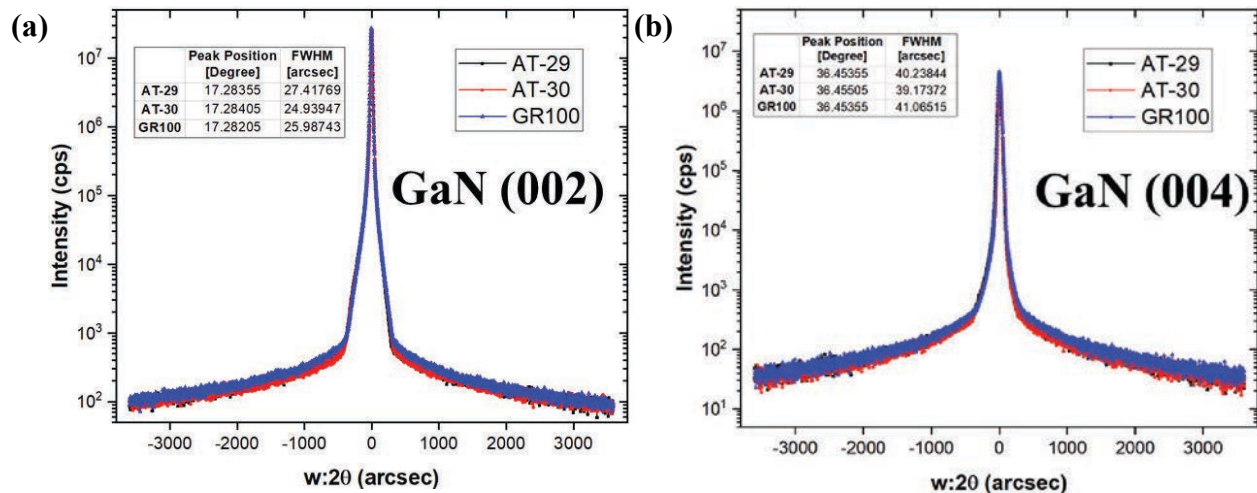
Last quarter, 68 samples were irradiated together and doubled the irradiation time from 50 to 100 hours. We accomplished to prove the mass production of neutron irradiation in MURR. Each batch (17 samples) was irradiated for 5 (GR5), 25 (GR25), 75 (GR75), 100 hours (GR100). Considering the size of Al sample holders, it is predicted that about 30 samples (1cm² size) would be irradiated simultaneously.

Crystal analysis: XRD

GR5, GR25, GR75, and GR100 were measured for X-Ray Diffraction (XRD) measurements at Missouri University of Science and Technology (MST). The measurement conditions are as follows:

- Type of monochromators: 2-bounce
- Step size: 0.0005°
- Angular range of GaN (002): 17.0813° ~ 17.4308°
- Angular range of GaN (004): 36.3593° ~ 36.5478°
- Time per step: 1 second
- X-ray wavelength $K_{\alpha} = 1.54 \text{ \AA}$

There was no big difference after neutron irradiation regardless of irradiation, as shown in Figure 1. The XRD profiles are tabulated in Table 1.



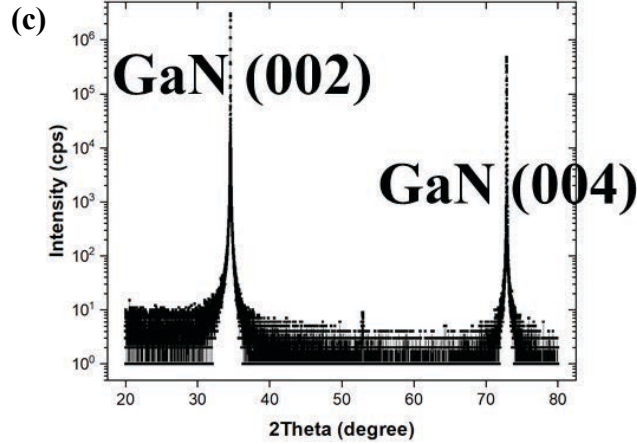


Figure 1. XRD profiles of GR100 for GaN (002), GaN (004), and broad scan. (a) is the profile of GaN (002), (b) is the profile of GaN (004), and (c) is the broad scan between 20° and 80°.

Table I. Peak position and FWHM of untreated samples from the different wafers (AT-29 and AT-30) and irradiated samples (GR5, GR25, GR75, GR100).

GaN (002)	Untreated AT-29	Untreated AT-30	AT-36 GR5	AT-36 GR25	AT-36 GR75	AT-36 GR100
Peak Position (°)	17.28355	17.28405	17.28105	17.28105	17.28155	17.28205
FWHM (arcsec)	27.41769	24.93947	25.4114	25.12177	24.7525	25.98743
<hr/>						
GaN (004)	AT-29	AT-30	GR5	GR25	GR75	GR100
Peak Position (°)	36.45355	40.23844	36.45455	36.45555	36.45405	36.45355
FWHM (arcsec)	40.23844	39.17372	38.01741	38.13147	41.66093	41.06515

It is acceptable that all irradiated samples were irradiated with similar neutron flux based on the gamma-ray spectroscopy results and the same irradiation position. The big difference among them is the irradiation time. Depending on the irradiation time, FWHM (Full Width at Half Maximum) was expected to increase linearly with a similar peak position. Considering 1 arcsec is 2.77×10^{-4} degrees, there is almost no change before and after irradiation at GaN (002) and GaN (004). As expected, there are no other peaks except for GaN peaks. A very small change is also checked in XRT (X-Ray Topography) measurements.

Crystal analysis: XRT and XRCT

In collaboration with SBU (Stony Brook University), GR5, GR25, GR75, and GR100 samples were measured before and after irradiation. Topographs are shown in Figures 2 and 3.

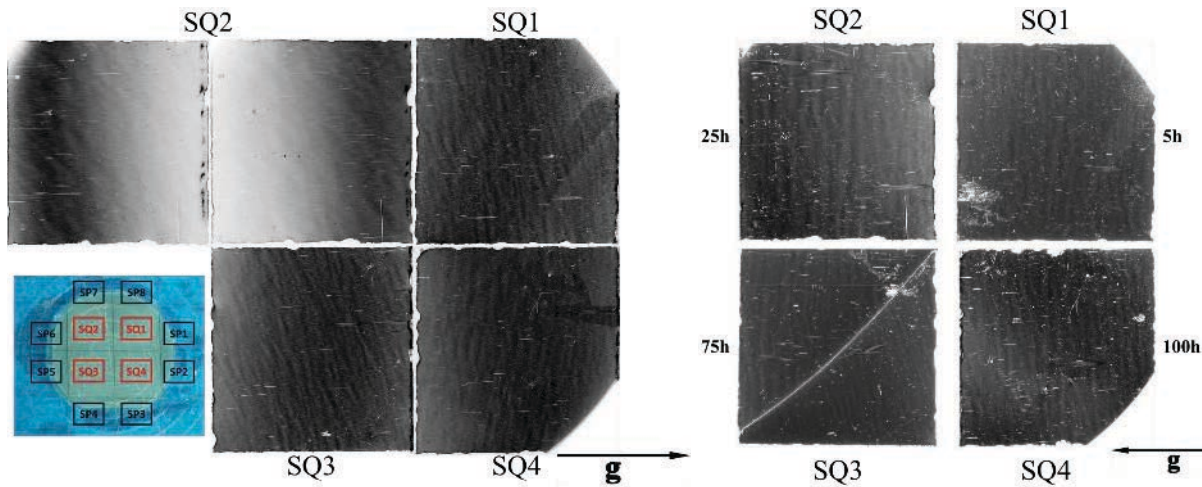
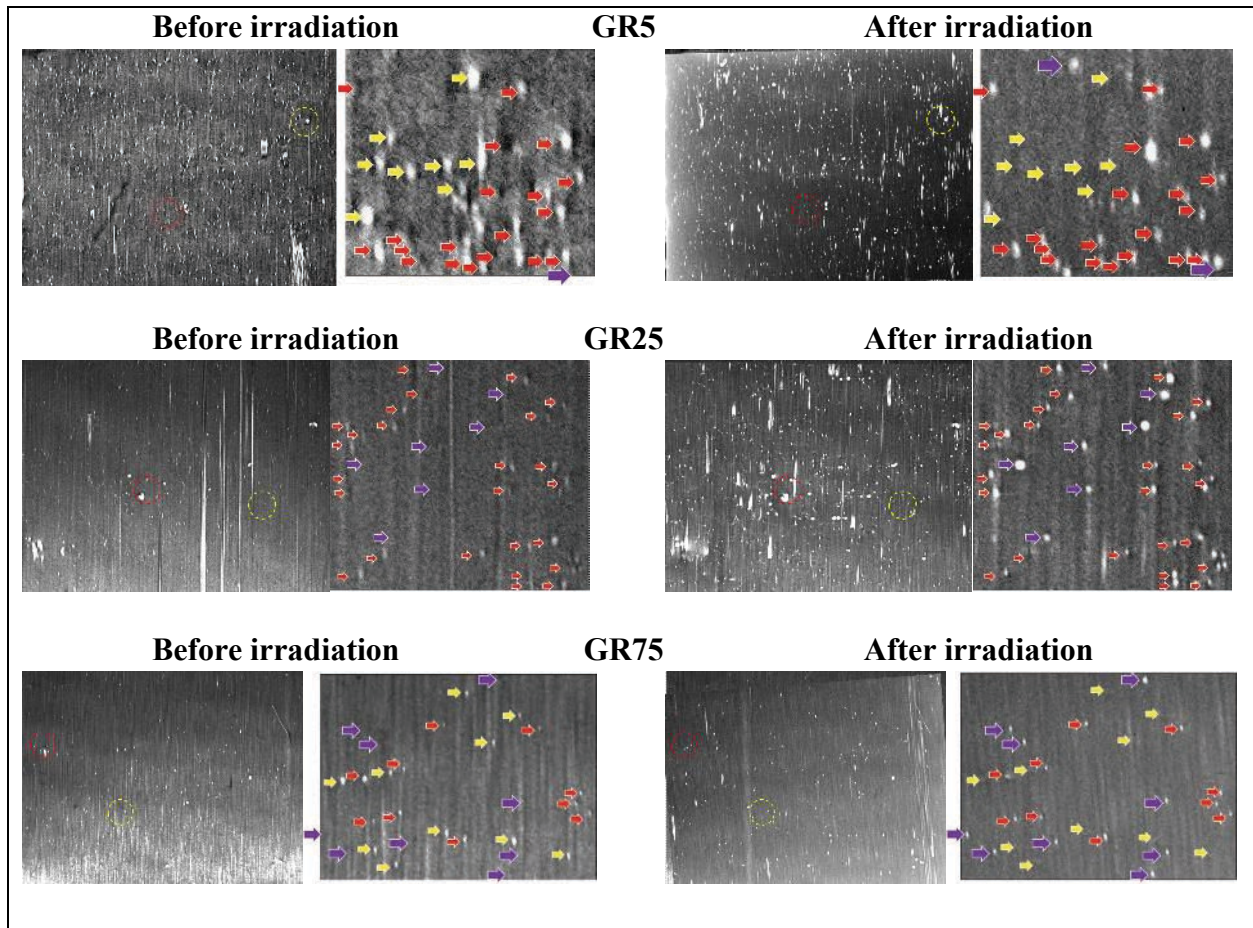


Figure 2. Topographs of GR5, GR25, GR75, and GR100. The left is topographs of untreated samples, and the right is topographs of irradiated samples. GR75 (SQ3) was broken during the measurements.



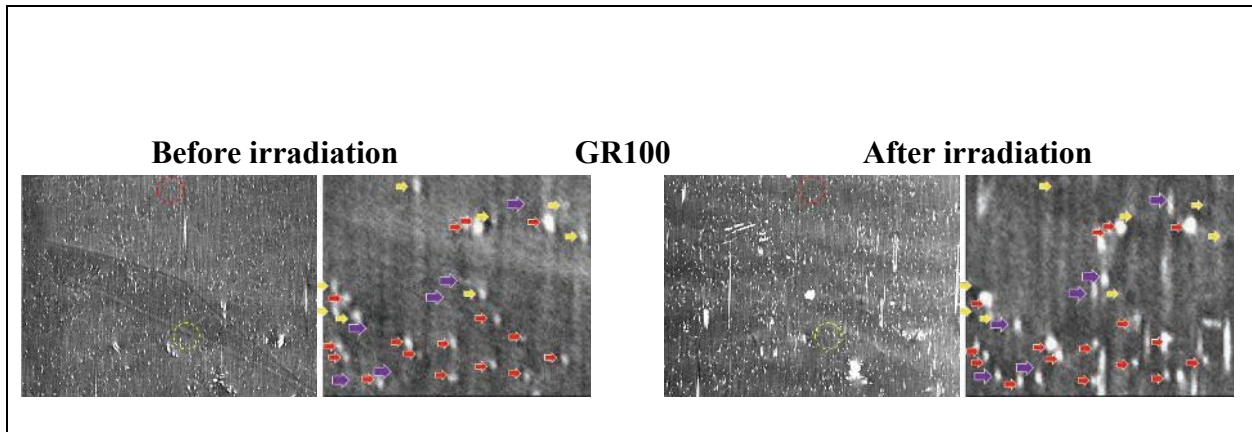
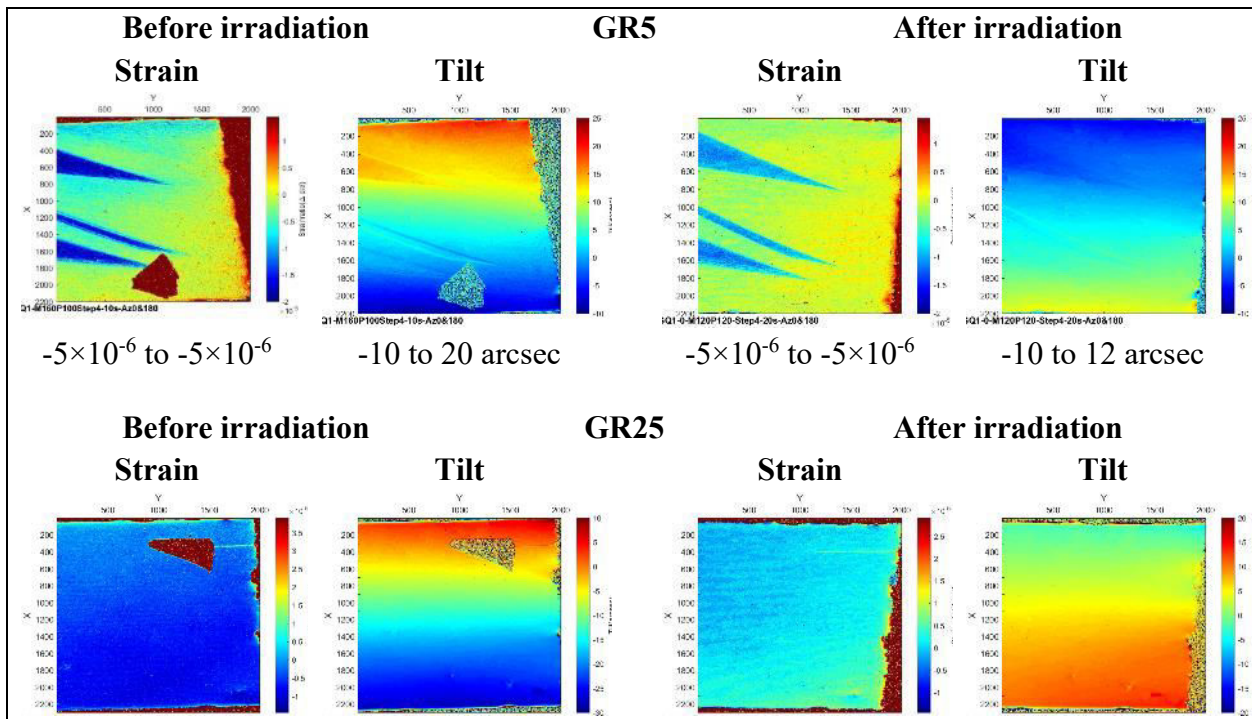


Figure 3. High magnification x-ray grazing incidence topograph from boxes in Fig. 2 showing threading dislocation contrasts as bright or dark dot shapes of various dimensions. Red arrows are the same defects before and after irradiation, purple arrows are new defects after irradiation, and yellow arrows are disappeared defects after irradiation.

Interestingly, some defects disappeared after irradiation. For GR5, there were more disappeared defects than new ones. However, the number of new defects is not proportional to the irradiation time. Only some of the dislocations might be able to be correlated. Dislocation density is not changed ($10^4/\text{cm}^2$ estimated). It is plausible that there would be a certain irradiation time to generate new defects, and the number of new defects would not correlate significantly with the irradiation time. With XRCT (X-ray Rocking Curve Topography), the strain and tilt of each sample were measured, as shown in Figure 4. The strain range and tilt range are tabulated in Table II.



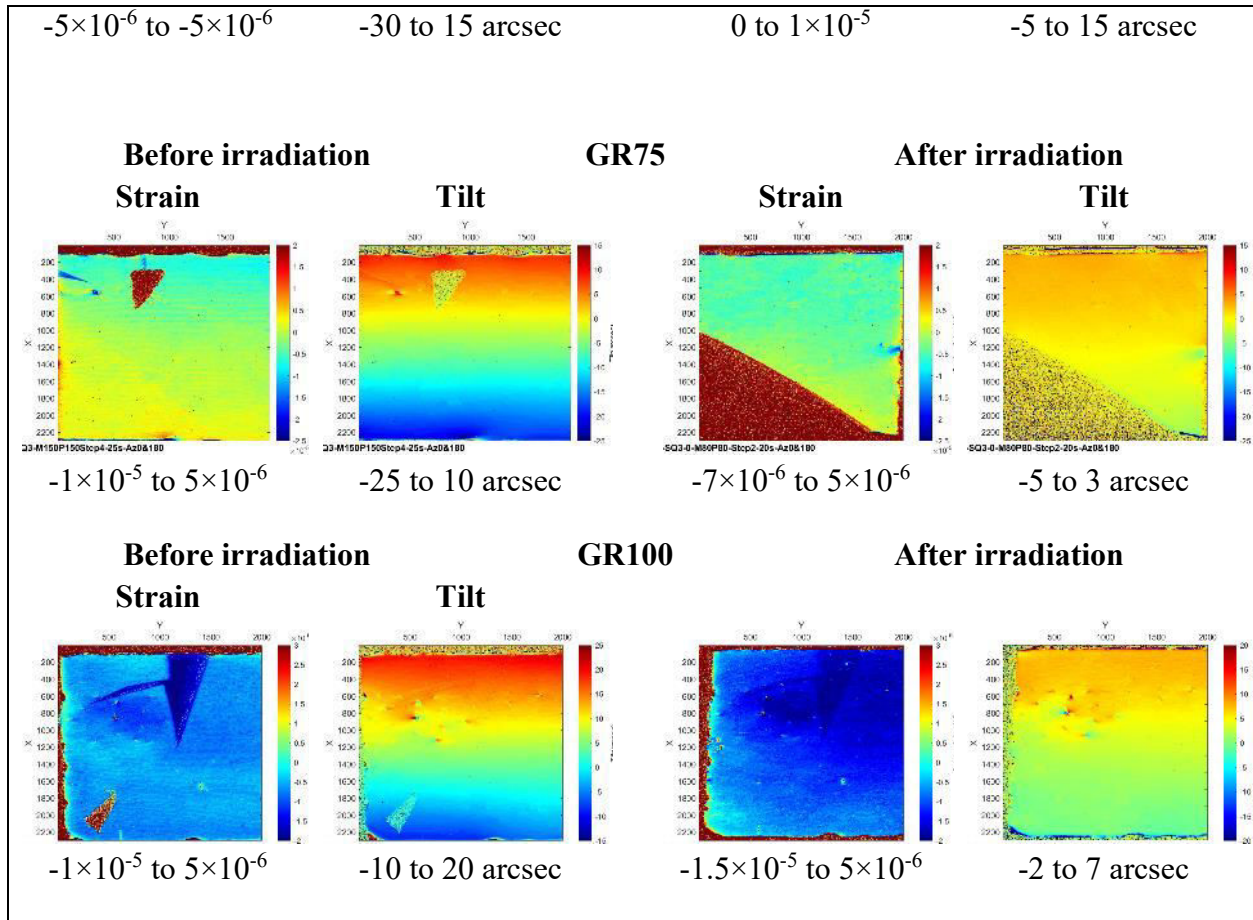


Figure 4. Strain and tilt of GR5, GR25, GR75, and GR100 before and after irradiation. The values of strain and tilt increase when the color changes from blue to red.

Table II. The range of strain and tilt of GR5, GR25, GR75, and GR100 before and after irradiation.

	Strain Range		Tilt Range	
	Before	After	Before	After
GR5	1×10^{-5}	1×10^{-5}	30 arcsec	22 arcsec
GR25	1×10^{-5}	1×10^{-5}	40 arcsec	20 arcsec
GR75	1.5×10^{-5}	1.2×10^{-5}	35 arcsec	8 arcsec
GR100	1.5×10^{-5}	2×10^{-5}	30 arcsec	9 arcsec

Strain ranges are not changed by irradiation, but tilt ranges reduce after irradiation. Longer irradiation times give a more significant decrease in tilt ranges. We guess neutrons hit the samples from all directions, which helps tilts decrease. All samples measured for XRD and XRT were annealed at 935 °C for 10 minutes with ambient Ammonia gas (NH₃). The XRD and XRT

measurements on the samples will be resumed very soon. It is expected that annealed samples show narrower FWHM and fewer defects.

Crystal annealing process

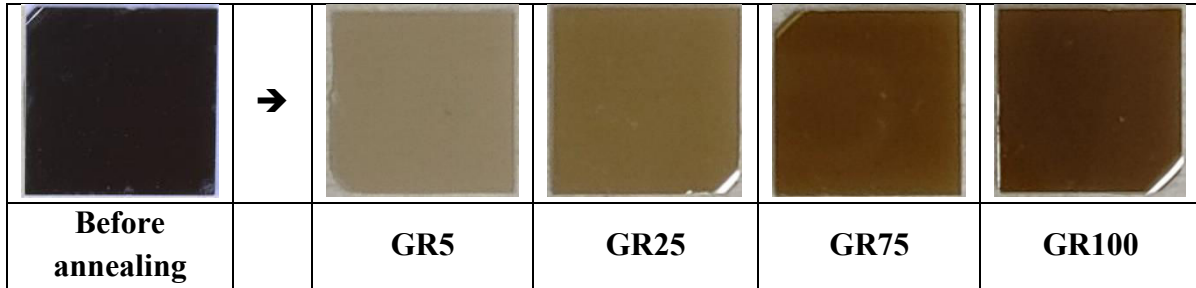


Figure 5. Images of GR5, GR25, GR75, GR100 before and after annealing

With our upgraded crystal annealing system, GR5, GR25, GR75, and GR100 samples were annealed at 935 °C for 10 minutes with ambient Ammonia gas (NH₃). The discoloration was reversed and regained their optical and electrical properties. Although the dislocation defects of irradiated samples measured by XRT are similar, the degree to which discoloration is healed is related to the irradiation time in Figure 5. The longer the irradiation time, the darker the color of each sample after annealing. The optical properties were studied in more detail with photoluminescence (PL) measurements.

Optical properties: PL spectroscopy

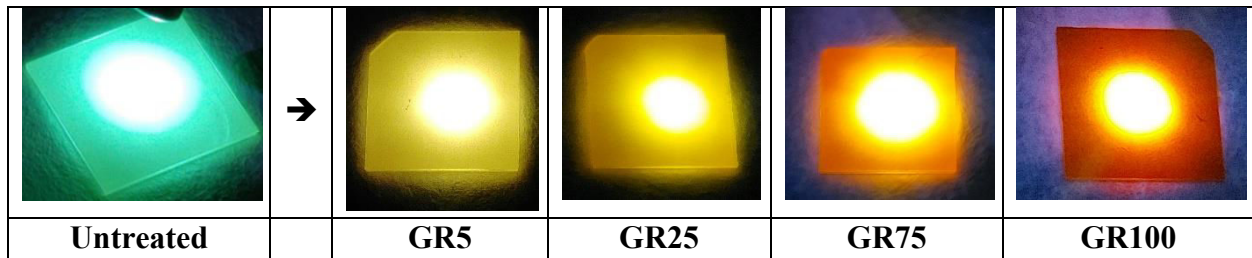


Figure 6. Color of untreated, GR5, GR25, GR75, and GR100 samples when exposed to a laser source with 325 nm excitation. Irradiated samples were annealed. Before annealing, all irradiated samples do not have any optical properties.

For the study of carbon behavior, each sample was irradiated 325 nm excitation laser source at room temperature. Before annealing, untreated samples from manufacture 3 take on a green color when exposed to the laser source, as shown in Figure 6. After irradiation and annealing, the samples take on a yellowish color, which is mainly related to carbon. Longer irradiation produces more carbon. That is why GR100 has a more orange color.

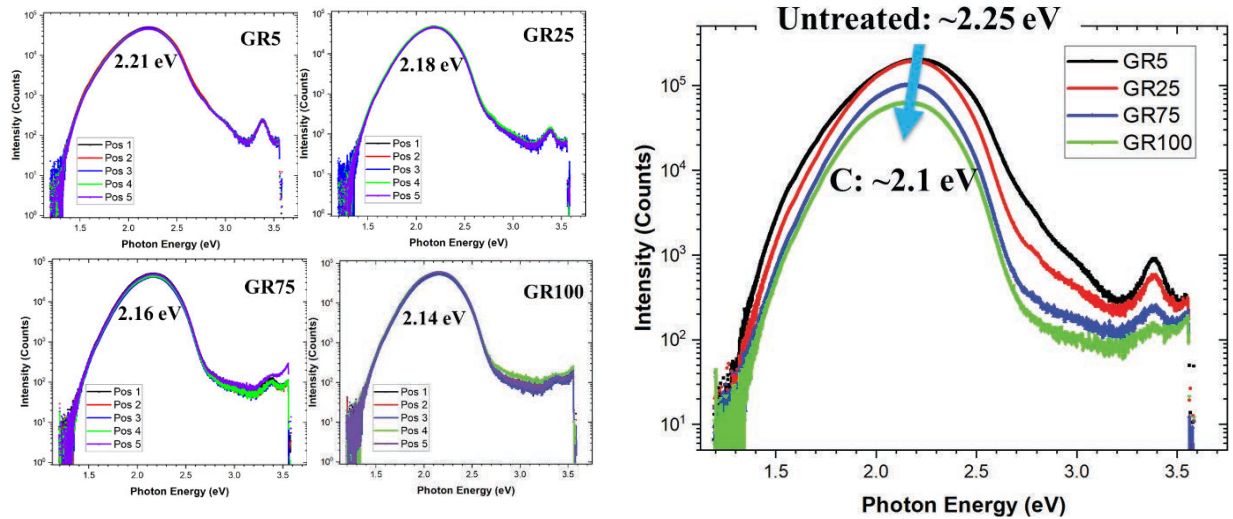


Figure 7. PL spectra of GR5, GR25, GR75, and GR100. The left side consists of 4 plots of GR5, GR25, GR75, and GR100. Each plot was measured at 5 different positions. The right side is the combined PL spectra.

In Figure 7, PL spectra show that the peak position and intensity of each PL spectrum decreases as the irradiation time increases. This result supports the carbon behavior as a p-type dopant. Furthermore, the peak intensity caused by GaN decreases as the irradiation time increases. It is guessed that longer irradiation produces more Ge and carbon, which leads to the reduction of GaN and more defects that might affect the optical properties. The hypothesis will be studied by Deep-Level Transient Spectroscopy (DLTS).

Electrical properties: J-V and I-V curves

For current (density) characteristics, Pt/Au (80nm/40nm) was deposited on the samples for Schottky contact. The J-V (Current Density-Voltage) curves were measured from -3 V to 3 V for overall current density properties. I-V (Current-Voltage) curves were measured 0.15 V to 0.75 V for turn-on voltage.

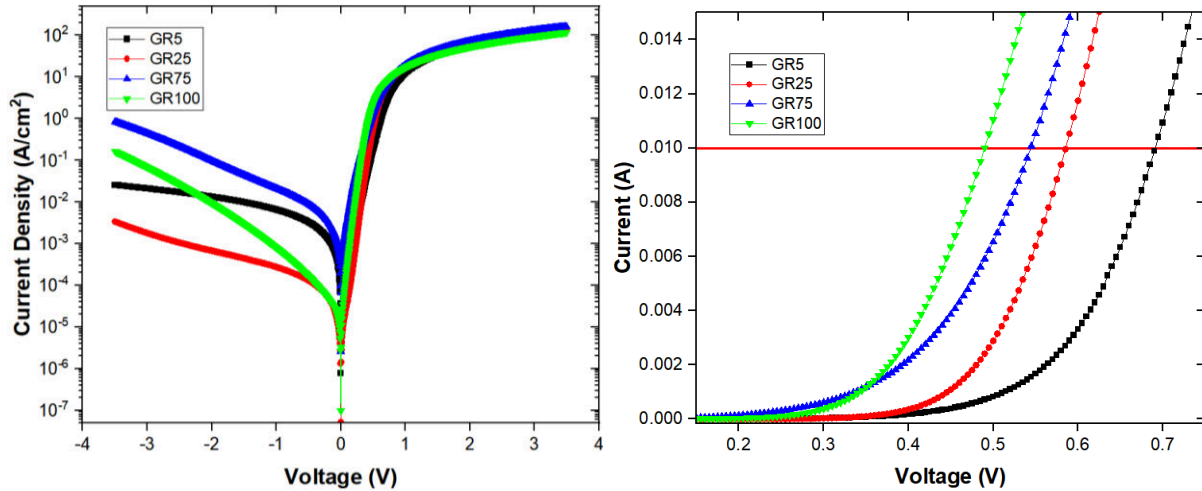


Figure 8. J-V and I-V curves of GR5, GR25, GR75, GR100. The left is J-V curves measured from -3 V to 3 V. The right is I-V curves measured from 0.15 V to 0.75 V.

It makes no sense to compare the curves with each other on that rectification ratio (RR) because each sample has different doping concentrations of Ge and ^{14}C . However, it makes sense to compare the slope in reverse bias voltage. The slope is proportional to the produced ^{14}C concentration, as shown in Figure 8. In other words, ^{14}C acts as a p-type dopant and causes leakage current when they are included in n-type GaN diodes. The turn-on voltage of GR5, GR25, GR75, GR100, if the criterion is 10 mA, is 0.69 V, 0.585 V, 0.545 V, 0.49 V, respectively. The turn-on voltage is mainly related to the Ge doping concentration and would be smaller when more Ge doping is produced. This is the first step to mathematizing the Schottky diode current. The final equation is as follows:

$$I = I_S \left(e^{\frac{eV}{k_B T}} - 1 \right)$$

With neutron flux information and SIMS profiles, we expect it will be possible to complete the well-known equation, which helps control the properties of the Schottky diode based on the equation.

Specific Contact resistance of Ohmic contacts:

We also presented before/after rapid thermal annealing (RTA) data to compare the RTA effect in order to enhance the electrical properties of metal contact. Figure 9 shows the schematic layout of the TLM patterns that have been used.

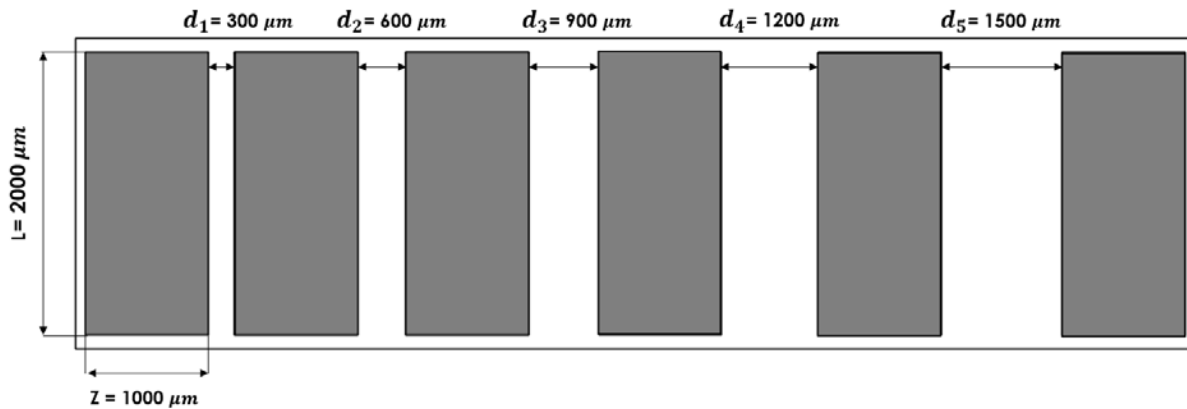


Figure 9. Schematic layout of the TLM patterns used for the experiment, array of rectangular pads was used with a spacing distance between the adjacent pads as $300 \mu\text{m}$, $600 \mu\text{m}$, $900 \mu\text{m}$, $1200 \mu\text{m}$, and $1500 \mu\text{m}$.

Bare AT-37- Sq 1: we used bare AT – Sq1, untreated GaN wafer, The sample was well cleaned using acetone, methanol, and DI water thoroughly and a Ti/Au (30 nm/ 150 nm) metal layer patterns as shown in Fig 9. were deposited using RF sputtering, the TLM measurement was carried by probing a pair of contact pads at a time. Voltage was applied and the resulting current was measured, the path of the current is through the first probe, into the metal contact, through the metal-semiconductor junction and contact, and into the second probe. For extracting the resistance information, we performed an I-V measurement using Keithley SMU 4100. The respective Total Resistance data were collected from each pair of the pads (separated by a spacing in consecutive increment order), the resistance measured for each pair of pads were plotted as distance/length between the contacts as the plot in Fig.10. In order to compare the Rapid thermal Annealing's influence on the resistance data, we compared the sample's TLM data before and after RTA treatment, the recipe used for the RTA of the samples was to anneal at 650°C under 200 Torr Nitrogen environment for 1 minute and 30 seconds duration.

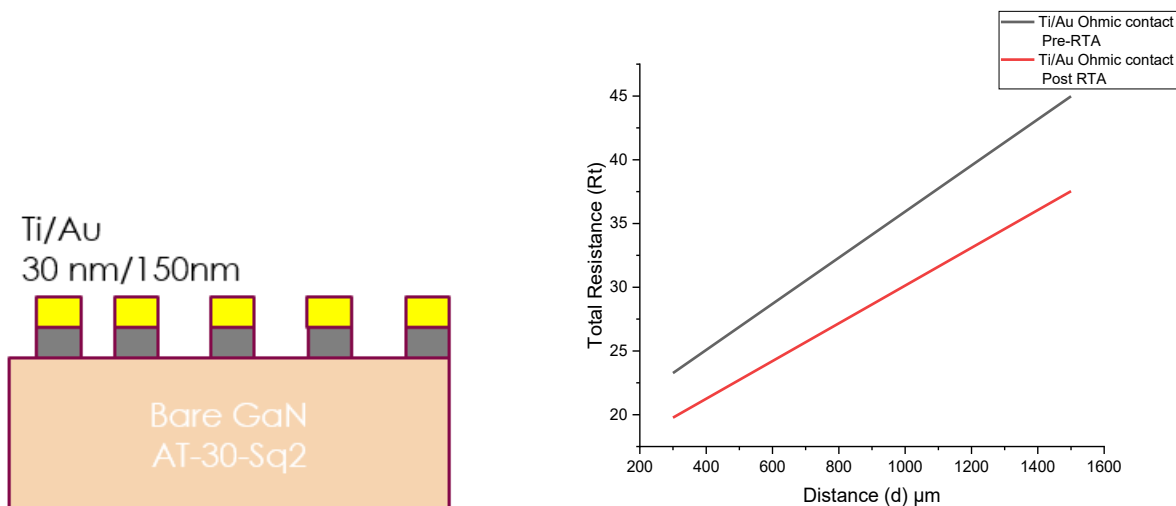


Figure 10. (a). The schematic representation of the sputter-deposited thin metal film layers on GaN substrate. (b). The Total resistance vs TLM distance plot for pre and post-RTA of Ti/Au Ohmic metal contact.

From the above linear plot using the Total resistance vs distance data points, the plot can be compared to the $Y = mX+C$ as a generic linear 2D equation, extracting the parameters like m and C can help us determine the specific contact resistance. The calculated values as shown in the table below.

Table III. The TLM parameters of Bare GaN wafer pre and post-RTA

At-30- Sq2 sample condition	Slope m ($\Omega/\mu m$)	C (Y-intercept) (Ω)	Contact Resistance (Ω)	Transfer Length (μm)	Specific contact resistance ($\Omega. cm^2$)
Pre-RTA	0.0181	17.833	8.916	477	4.40×10^{-2}
Post RTA	0.0148	15.33	7.665	517.90	3.969×10^{-2}

So, from the above data, it is evident that Rapid thermal Annealing has a great effect on improving the ohmic contact between metal /semiconductors as there is a 16% decrement of specific contact resistance when there is RTA carried. From the Fig.10 (b), in the case of the post-RTA sample the decrement in the slope of resistance vs distance plot (compared to pre-RTA condition) indicates the decrement in the resistance between the ohmic contact/semiconductor, RTA process reduces the resistivity, thus increasing the conductivity, RTA process modifies the structural properties of metal by removing the mechanical stress in the metal film layer, thus making a great contact on the surface of semiconductor with enhanced electrical properties. We believe we can achieve an ohmic contact with even smaller specific contact resistance by changing the RTA parameters and ohmic metal layer construction using sandwich layers of metal layers with lower work-function to bring down the barrier height between metal/semiconductor.

Directional Photonuclear Irradiations in ANL

Zn-doped P-type GaN

In collaboration with Argonne National Laboratory (ANL), we accomplished to prove that Zn-doped GaN by selective photonuclear transmutation doping (PTD) is a p-type GaN last quarter. Although the samples irradiated with 40 MeV were broken during SIMS measurements at EAG, XRD measurements for the broken samples were performed at Missouri S&T. The result in Figure 11 is totally opposite to our expectations.

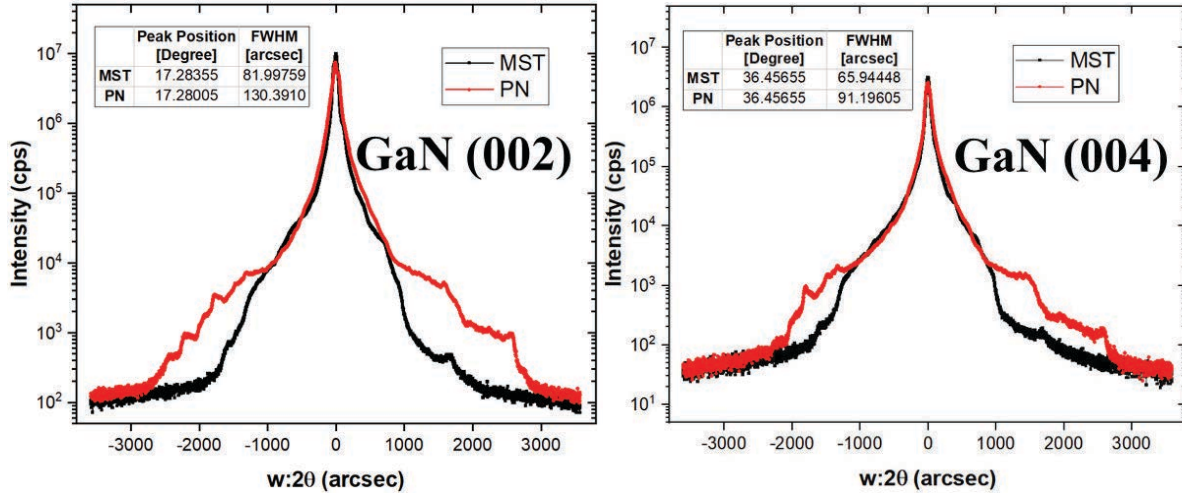


Figure 11. XRD profiles of Zn-doped GaN irradiated with 40 MeV.

At GaN (002) and GaN (004), the FWHM drastically increased after irradiation. Comparing the neutron irradiation in Figure 1, the main parameter to cause bigger FWHM is beam energy. This quarter we irradiated two samples with 20 MeV beam energy for 240 hours at 2 kW. One sample was fully irradiated, and the other was selectively irradiated. The fully doped sample with the samples, it is expected that irradiation time would be considered as a main parameter for the broader FWHM.

Some metals (Ti, Pt, Pd) were deposited on the Zn-doped samples, but they did not show a good Schottky barrier due to their high work function. We finally found metal with low work function and accomplished to prove the Schottky contact of Yttrium through J-V curves, as shown in Figure 12. The rectification ratio (RR) at ± 3 V, ± 5 V, ± 10 V is 4330, 2820, and 1257. A good RR is necessary to measure the difference of capacitance, particularly DLTS, which helps find new defects by photonuclear irradiations and determine the activation energy.

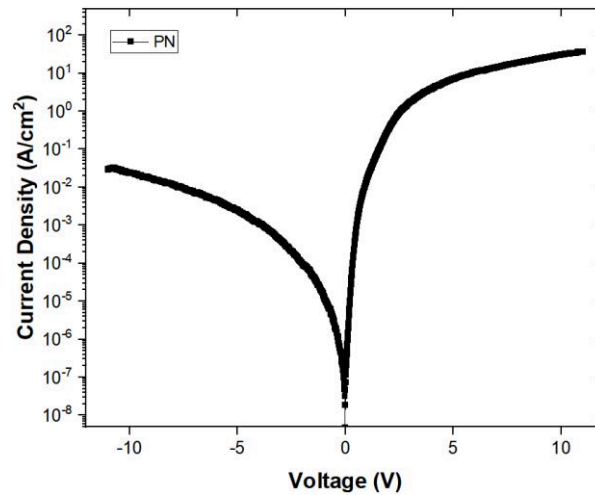


Figure 12. J-V curves of Zn-doped samples irradiated with 20 MeV.

Publications

“Enhanced electrical properties of n-GaN doped by a neutron transmutation doping process with high epithermal neutron flux” is in review. We are writing a paper on the zinc behavior as a p-type dopant: “p-type GaN doped by ^{68}Zn through photonuclear transmutation doping process.

ARPA-E PNDIODES

GaN vertical power FinFETs

Period covered by report:

November 1, 2021 – January 26, 2022

Principal Investigator:

Prof. Tomás Palacios

Email: tpalacios@mit.edu

Phone: (617) 324-2395 Fax: (617) 258-7393

Institution: Massachusetts Institute of Technology

Department: Electrical Engineering and Computer Science

Institution Address:

77 Massachusetts Avenue, Cambridge, MA 02139

February 1, 2022

Executive Summary

Vertical GaN power transistors offer improved performance over lateral GaN transistors in terms of current rating per unit area, thermal management, and reliability. Thanks to the generous support of ARPA-E SWITCHES, we have demonstrated GaN Power FinFETs with record 5 A current rating and 1200V BV with a device footprint of 0.45 mm². Under the PNDIODES program, we have focused on pushing the performance limits of vertical GaN power FinFETs.

This past quarter we have continued to characterize the previously fabricated vertical GaN FinFET devices including measurements of recent medium size devices. These devices exhibited currents on the order of 1 A, a high $I_{on}/I_{off} > 10^8$, and near zero threshold voltage. We have also began the first positive bias temperature instability (PIBT) measurements on vertical GaN finFETs to assess device reliability. These tests suggest our gate stack remains stable with bias stresses up to 6 V above V_T .

For device fabrication, we have designed an entirely new process flow to allow for annealed ohmic contacts, a thicker, self-aligned gate metal, and a far more uniform field oxide. Initial results with this process looks promising and we are attempting it on actual power finFET substrates. In the previous quarter, we began experiments to fabricate vertical finFETs with superjunction trenches filled with sputtered NiO as a wide bandgap p-type semiconductor. We are in the process of optimizing this deposition and are trying to acquire a new NiO target for use in our more advanced sputterer.

Major risks for future milestone

- Obtaining a quality interface between GaN trenches and the sputtered nickel oxide that is free of detrimental interface oxides and charges.
- Optimizing the sputtering of NiO_x to fill large aspect ratio trenches to enable vertical GaN FinFET superjunctions
- Optimizing deep, self-aligned trenches in GaN

Details of technical progress

GaN vertical devices have recently shown better V_B and specific R_{on} than GaN lateral devices, especially above 600 V. GaN power FinFET is one of the most promising device architectures among the vertical GaN transistors demonstrated by different groups. Thanks to the ARPA-E SWITCHES program, our team has previously demonstrated 1200 V, 0.2 mΩ·cm², 5A and 800V, 10A GaN vertical fin power transistors [1]. These devices also showed record switching figure of merit as shown in Table 4[2].

Table 4. Benchmark of power device technologies with key device metrics

Device Technology	Manufacturer / Maker	R_{on} (mΩ·cm)	BV (V)	I_{on} (A)	Die Size (mm)	V_{on} (V)	C_{on} (pF)	C_{off} (pF)	Q_{on} (nC)	Q_{off} (nC)	Q_{sw} (nC)	Switching FOM $R_{on} \cdot (Q_{on} + Q_{off})$ (ns) $R_{on} \cdot (Q_{on} + Q_{off} + Q_{sw})$ (ns)
Vertical GaN FinFET	MIT	2.1 (0.91 Ω)	1200	5	~0.5	1.3	248.3	42.2	1.07	2.04	~0	2.83 (this device) 2.46 (pad optimized)
SiC MOSFET (CPM2-1200-0160B)	Cree	2.7 [15] (0.16 Ω)	1200	20	6.28	2.5	525	47	34	14	105	7.68 24.48 (include Q_{sw})
SiC JFET Cascode (UJN1208Z)	United SiC	1.7- (0.15 Ω)	1200	18.4	1.13-	4.4	738	58	30	6	63	5.4 14.85 (include Q_{sw})
Si IGBT (NGTB15N120FLWG)	ON Semi	~20 (~0.25 Ω)	1200	15	320	2	3600	110	150	68	1500	15260 120260 (include Q_{sw})
Si CoolMOS (IPD90R1K2C3)	Infineon	~8- (1.2 Ω)	900	5	~23.6	3	710	35	28	12	3700	57.6 4488 (include Q_{sw})
Lateral GaN HEMT (GS66502B)	GaN Systems	~5 [16] (0.2 Ω)	650	7.5	33	1.3	65	17	1.5	0.4	~0	0.38
Vertical GaN MOSFET [4]	TOYODA GOSEI	2.7	1200	23.2	2.25	3.5	N. A.					
Vertical GaN OG-FET [5]	UCDavis UCSB	7.2	320	1	0.2	1						
Vertical GaN CAVET [2]	Avogy	2.2	1500	2.3	0.17	0.5						

Note: *Source: <http://unitedsic.com/cascodes>; **Calculated by using the R_{on} in the data sheet and the R_{on} reported in the aforementioned link; ***Source: Infineon's application note titled "CoolMOS- C7: Mastering the Art of Quickness".

Despite the promising pioneering results, the fabrication technology was not optimized for large-scale device fabrication which can result in low fabrication yield. Previously, we focused on optimizing fabrication modules and developed the capability to control the doping density required for high voltage devices. Fig. 12(Left) shows the schematic diagram of GaN vertical FinFET with 1200 V breakdown voltage[2]. The epitaxial structure of this device consists of 300 nm n⁺ GaN source layer, 9.5 μm n⁻ GaN drift layer and 1 μm n⁺ GaN drain layer grown on bulk GaN substrate. Following a similar methodology as Baliga [3], we can calculate the theoretical breakdown voltage of GaN drift region as a function of doping concentration for a particular drift region thickness. Fig. 12(right) shows that the expected breakdown voltage is around 2100 V for an n-GaN power device with 10 μm thick drift region and 1×10¹⁶ cm⁻³ doping concentration.

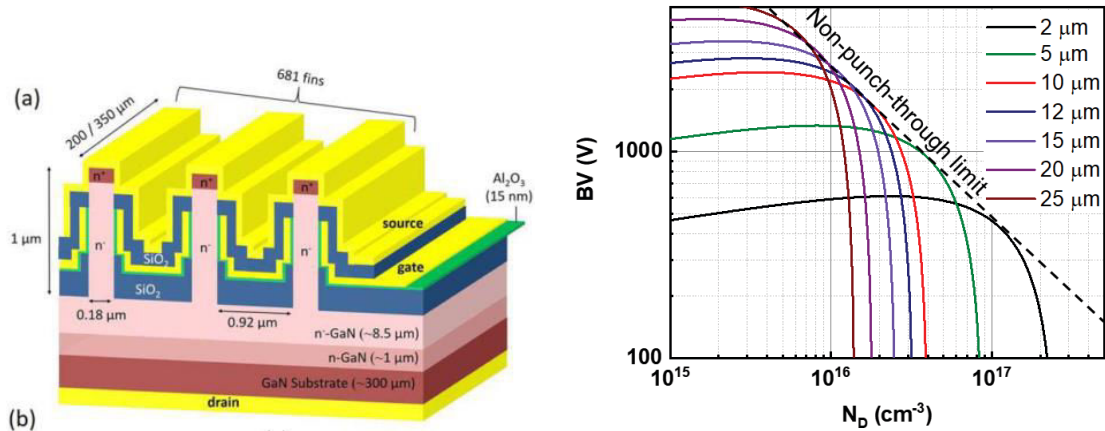


Figure 9. (Left) Schematic diagram of the GaN vertical FinFET. (Right) Design space of the drift region for the GaN power device as a function of the doping concentration for different drift region thickness.

Vertical GaN FinFET Characterization

FinFET Performance

Our most recent finFETs exhibit a very high device yield (>90% functional large devices) with an $I_{on}/I_{off} > 10^8$, $V_{th} \approx 0$ V, a $SS_{av} \approx 130$ mV/decade in large devices. Output and transfer characteristics showing current density greater than 1 A is shown in Fig. 13. A transmission electron micrograph (TEM) cross-section of the measured device is shown in Fig. 14 with an EDS elemental mapping overlay. The TEM image shows the non-ideal field oxide etch profile has resulted in a thicker equivalent oxide thickness (EOT), which explains the higher SS.

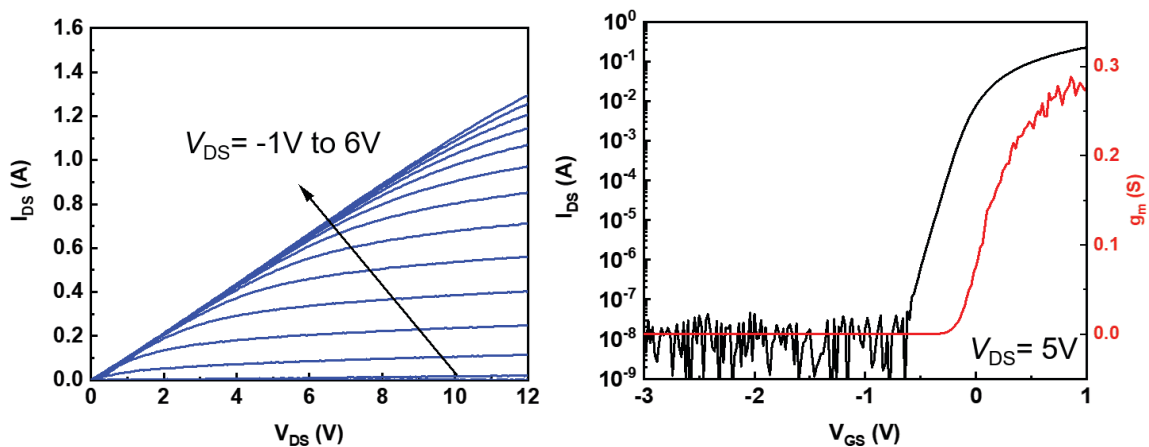


Figure 10. (Left) Output and (right) transfer characteristics of a large-area vertical finFET

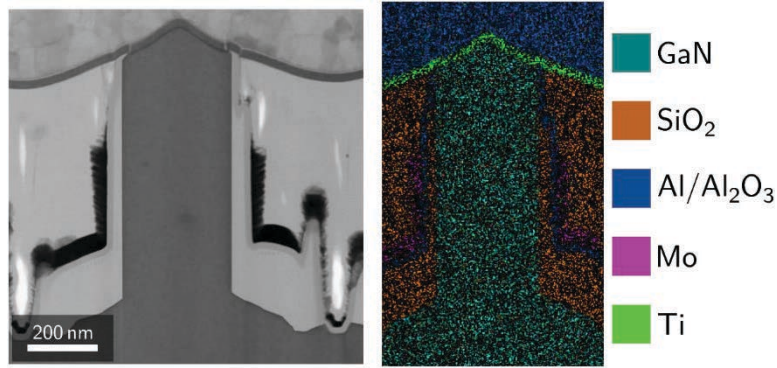


Figure 11. Cross-section transmission electron micrograph and (right) elemental EDS mapping of a vertical FinFET unit cell.

Positive Bias Temperature Instability (PBTI) Measurements

During the last quarter we have started characterizing the threshold voltage stability of vertical FinFETs under positive gate voltage stress. For the preliminary experiments, we have used small ($40\ \mu\text{m} \times 70\ \mu\text{m}$) FinFETs fabricated on engineered substrates. The gate stack of these devices is identical (20 nm Al_2O_3 /125 nm Mo) to our baseline FinFETs fabricated on bulk GaN and the results should represent the threshold voltage stability of FinFETs fabricated on bulk GaN substrates.

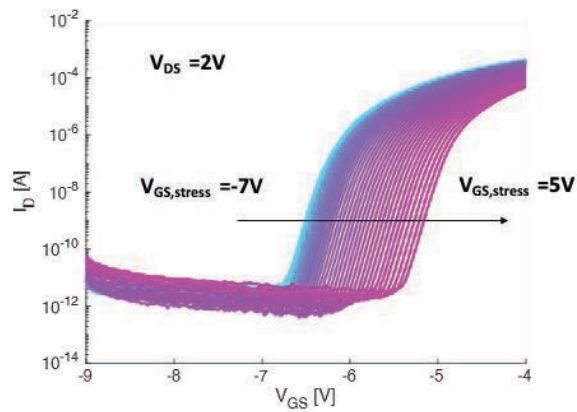


Figure 12. Evolution of FinFET transfer characteristics during measure-stress (100s)-measure cycle.

Fig. 12 shows the evolution of transfer characteristics during measure- $V_{\text{GS, stress}}$ (100 s)-measure cycle where the range of $V_{\text{GS, stress}}$ was selected from 1 V below V_{T} of pristine device (-7 V) to ~ 11 V gate overdrive voltage ($V_{\text{GS}} = 5$ V). The device shows classic PBTI characteristics where V_{T} shows positive shift with increasing stress voltage amplitude.

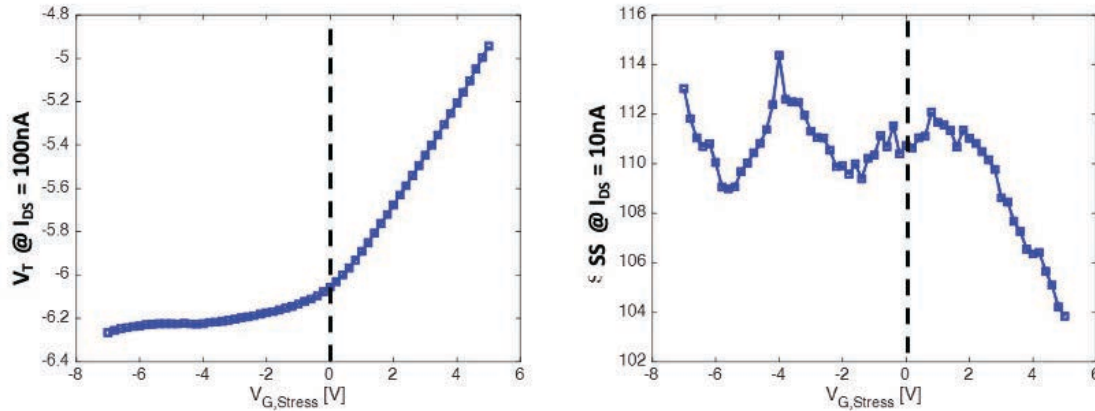


Figure 13. Evolution of (left) threshold voltage and (right) subthreshold swing during measurement-stress (100s)-measurement cycle.

Fig. 13 shows that both V_T and SS show negligible degradation up to 6 V gate overdrive ($V_{GS,Stress} = 0$ V) with $\Delta V_T = 0.2$ V. However, degradation is more prominent at higher positive stress voltages and ΔV_T is around 1.3 V at 11 V gate overdrive.

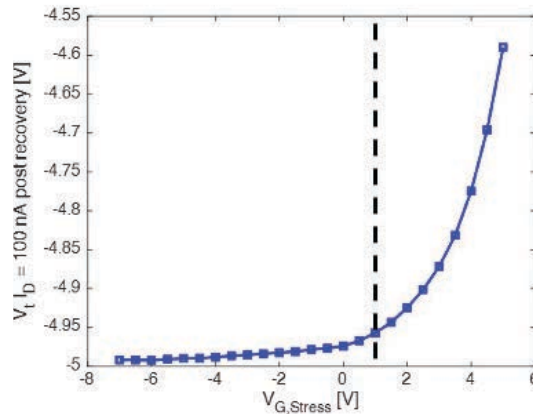


Figure 14. Evolution of threshold voltage during measurement-stress (100s)-recovery (1000s)-measurement cycle.

In the next experiment, to quantify safe operating range, we have added 1000s after stress at each stress voltage and characterized the devices after this recovery period. A different device with $V_T = -5$ V was used for this experiment. Fig. 14 shows that the ΔV_T at 6 V overdrive ($V_{GS,Stress} = 1$ V) is less than 0.05 V after adding a 1000 s recovery after the stress voltage and ΔV_T is less than 0.45 V at 10 V gate overdrive ($V_{GS,Stress} = 5$ V). These results indicate that the gate stack of our FinFETs is very robust under positive gate stress. During next quarter, we will extend these experiments to include higher temperature and UV recovery after permanent degradation on FinFETs fabricated on bulk GaN substrate.

Double Pulse Measurements

Double pulse measurements are a standard technique for measuring the switching performance of a power transistor. However, due to the high-power and high-speed nature of the tests, it is very difficult

to perform on a bare die with a probe station. Instead, it is usually best-practice to isolate and package each device for measurements in a dedicated test fixture.

With our most recent finFETs, we hoped to quantify the switching performance with double pulse tests, met several roadblocks. Within MIT, we have established a collaboration with Professor David Perreault's group who are experts in double pulse measurements. Their system is designed to work with a TO-263-7 package, which is proving challenging to find as a bare package. Alternatively, we can take their PCB design and modify it to accept a new package type, which is the likely route we will take in the future. In the meantime, we were presented with another roadblock in that our device design files were not designed with single device isolation in mind. It would not be possible to use a standard dicing saw without very low device yield. We have reached out to Disco for laser dicing services, but surface metal and narrow dicing lines on our samples would make it difficult. Our masks have been adjusted to prevent this problem in the future and are continuing to explore options for enabling double pulse measurements.

Tesla Probe Station Repairs

Our high voltage Tesla probe station has vacuum issues in the chuck that prevents good contact with the backside drain contact of our finFETs. Currently, for sufficient drain contact, we have to mount the samples on an aluminum coated silicon wafer using silver paint and then probe the silicon wafer. This is clearly non-ideal because the silver paint and silicon wafer adds significant series resistance.

We have had the probe station assed by FormFactor's engineers and repair parts are scheduled to arrive in late February or early March. These parts will be installed by an external vendor which should solve the vacuum problems and allow us to use the chuck bias.

Additionally, our probe manipulator for the high-power SMU is broken and has been sent out for repair with a scheduled return of March 7th. This is the only probe capable of measuring high voltage and currents with good resolution and is essential for high quality auto-probing measurements.

FinFET Fabrication Updates

New Wafer Growth

Recently, our collaborators at UCSB have brought their MBE system back online. They have provided a new quarter of a 2-inch bulk-GaN wafer with $n^+/n^-/n^+$ (0.3 μm / 9.5 μm / 1 μm) epi-layers having doping levels of $\sim 2 \times 10^{19} \text{ cm}^{-3}$ for the n^+ regions and $\sim 1-2 \times 10^{16} \text{ cm}^{-3}$ for the n^- drift region. By adding a surfactant and replacing their NH_3 purifier, they were able to reduce the drift layer doping while maintaining reasonable morphology. This material will be used in our next round of finFET fabrication.

Additionally, Lincoln Laboratory has provided a new standard 1200 V finFET structure grown on two 2-inch bulk-GaN wafers with $n^+/n^-/n$ (0.3 μm / 9.5 μm / 1 μm) epi-layers having doping levels of $\sim 3 \times 10^{19} \text{ cm}^{-3}$ for the n^+ regions and $\sim 2 \times 10^{16} \text{ cm}^{-3}$ for the n^- drift region. A portion of this wafer will be sent out for SIMS characterization to verify the doping density and structure. Standard finFET fabrication with this material is already underway.

Lincoln Laboratory is also growing two 2-inch bulk-GaN wafers with a modified structure for a 1200 V superjunction (SJ) finFET. The proposed structure is a $0.3\ \mu\text{m}$ $\text{n}^+\text{-GaN}$ source doped to $\sim 3 \times 10^{19}\ \text{cm}^{-3}$, a $0.8\ \mu\text{m}$ $\text{n}^-\text{-GaN}$ channel doped to $2 \times 10^{16}\ \text{cm}^{-3}$ (chosen for direct comparison to the standard finFET wafer's channel), a $6\ \mu\text{m}$ $\text{n}^-\text{-GaN}$ drift region doped to $2 \times 10^{16}\ \text{cm}^{-3}$, and an n-GaN seed layer. The drift region is doped higher and is shorter than the standard finFET because we will laterally deplete it with the superjunction techniques described in section 3.

New Process Flow

In our previous reports, we have shown improved yield and uniformity in our fabrication of large-area vertical GaN finFETs. However, a couple shortcomings still exist which can be seen in Fig. 18:

1. Imperfect SiO_2 deposition results in voids that lead to electric field crowding between fins
2. Non-optimized SiO_2 etching results in residual SiO_2 beneath the gate oxide
3. Excessive SiO_2 back etching damages the tops of the fins, sharpening them and requiring a Cl_2 based back-etch
4. Ohmic contacts cannot be annealed, possibly limiting the on-resistance of the device
5. Gate metal thickness is limited by the ability to sputter Mo into deep trenches.
6. The gate metal and source metal are not self-aligned and require carefully timed dry etches

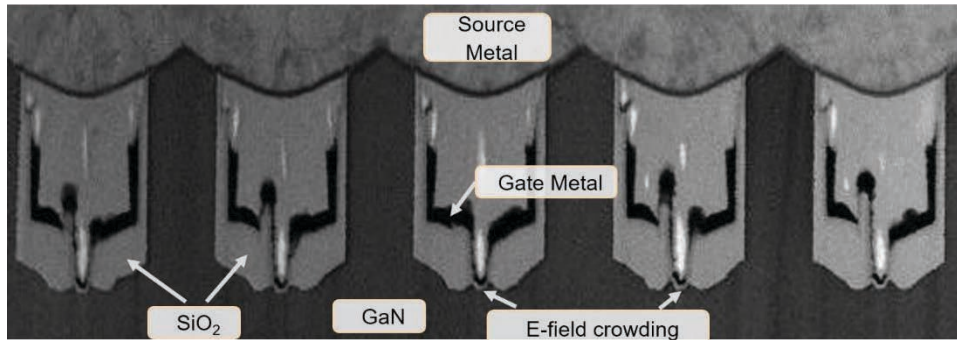


Figure 15. Cross sectional SEM of a vertical GaN finFET with a thin field oxide between fins

To mitigate these fabrication problems and create an even more reliable process, we have developed the process flow shown in Fig. 19. The fabrication techniques rely heavily on the use of a custom-built electron-beam evaporator mount that was machined at the MIT machine shop. This mount allows for electron-beam evaporation at any arbitrary angle. By carefully designing the angles and thicknesses of various metal layers as well as the fin geometry, we can very reliably and accurately pattern vertical structures with no lithography or timed dry etching.

The process flow begins with the patterning of the field oxide. We deposit only 100 nm of SiO_2 , which allows for void-free, uniform deposition. We then pattern the oxide with a novel metal-metal lift-off process. By evaporating aluminum at a steep angle, we can use adjacent fins to act as a shadow mask and only deposit metal at the tops of the fins, which creates a small overhang feature. Then, if we

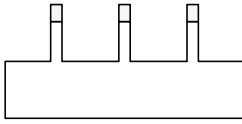
evaporate nickel at a shallower angle, the overhanging aluminum acts as a shadow mask to deposit metal at the base of the fins up to a height determined by the nickel evaporation's angle. Since we used aluminum, we can fully wet etch it in concentrated TMAH, which lifts-off the nickel that was deposited on the tops of the fins. Finally, we developed a high-pressure, high-temperature, and low power isotropic SiO₂ dry etch that gently and chemically removes the oxide from the sidewalls of the fins. During the etch, the nickel preserves the SiO₂ at the bottoms of the trenches. After the etch, we can, we remove the nickel with nickel etchant to leave us with our SiO₂ field oxide.

All previous iterations of our vertical GaN finFETs have used a gate-first process with an Al₂O₃ gate dielectric. Since the Al₂O₃ degrades at high temperatures, this prevented us from annealing our ohmic contacts above 400°C. Our new devices use an ohmic-first process. After patterning the field oxide, the ohmic metal stack is deposited at a very steep angle so that adjacent fins again shadow the deposition and leave metal only on the tops of the fins. Once repeated on both sides, the ohmic metal can be annealed at any temperature since both SiO₂ and GaN are very robust to high temperatures.

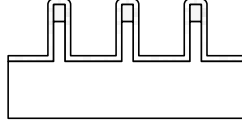
Following the ohmic metal deposition, we once again have an overhang feature at the tops of the fins that can be used as a shadow mask to create a perfectly self-aligned gate with no risk of shorting to the source. After annealing the source, we can use ALD to deposit a conformal Al₂O₃ layer as our gate oxide. Then, we deposit our gate metal at a shallow angle using the source metal as a mask, making this a fully self-aligned process. Moreover, the gate metal can be deposited arbitrarily close to the source metal since the gate oxide beneath it will prevent any risk of shorting. After depositing on both sides of the fins, a third deposition at the standard flat angle can be used to deposit arbitrarily thick gate metal between the fins, which will reduce gate resistance.

Next, we need to isolate the gate and source metals so that probe pads can be connected. To do this, we use our previously developed process for the gate-source spacer. Here, we deposit a thick SiO₂ layer using a conformal deposition that self-planarizes. Then, we use a dry etch to etch back the oxide until the tips are exposed. Unlike previous processes, we now have gate metal and gate oxide on top of the source metal. To remove this, we simply use nickel etchant to remove the gate metal, and then use a dry etch to remove the Al₂O₃. After this, we sputter and pattern our probe pads.

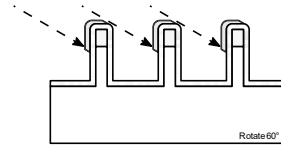
1. Start with standard finFET fins



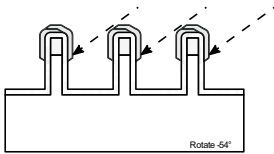
2. Coat with 100 nm of SiO₂



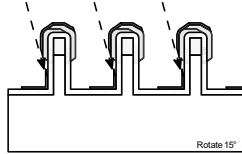
3. Evaporate 100 nm of Al at an angle of 60°



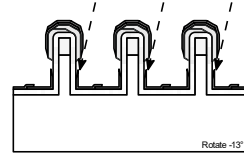
4. Evaporate 100 nm of Al at an angle of -54°



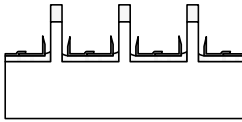
5. Evaporate 50 nm of Ni at an angle of 15°



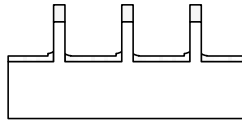
6. Evaporate 50 nm of Ni at an angle of -13°



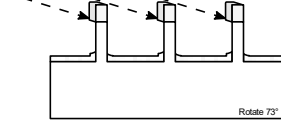
7. Use 25% TMAH to liftoff Ni and Al from the tops of fins, then use an isotropic dry etch to remove the SiO₂ from the fin sidewalls



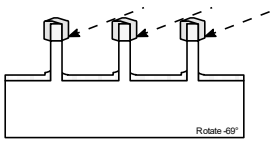
8. Strip the Ni with a wet etch



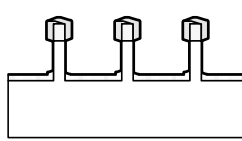
9. Evaporate the ohmic metal stack at an angle of 73°



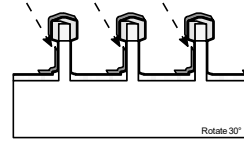
10. Evaporate the ohmic metal stack at an angle of -69° and anneal



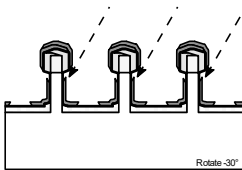
11. Deposit 20 nm of Al₂O₃ with ALD



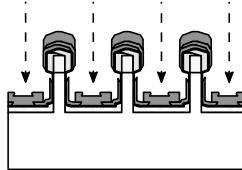
12. Evaporate 50 nm of Ni at an angle of 30°



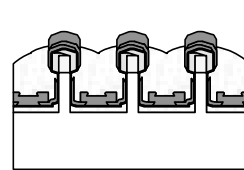
13. Evaporate 50 nm of Ni at an angle of -30°



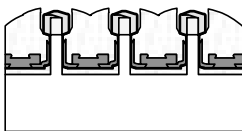
14. Evaporate 100 nm of Ni at an angle of 0°



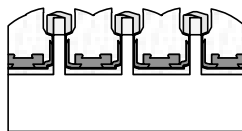
15. Planarize the surface with a thick, conformal coating of SiO₂ and etch back until the tips of the fins are exposed



16. Wet etch away the exposed Ni



17. Wet or dry etch the exposed Al₂O₃



18. Deposit pad metals

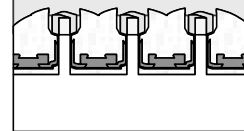


Figure 16. Updated process flow for vertical GaN finFETs

An initial test run was done using GaN-on-sapphire wafers designed for RF transistors with a thin drift region. A cross-sectional SEM of the completed device is shown in Fig. 20 where we demonstrate an almost perfect recreation of the proposed process flow. Here, we see that the field oxide remains highly

uniform along the trenches between fins and ends at the exact same height from the top of the fins, regardless of the trench profile. Also, the isotropic dry etch results in a nicely tapered ending to the field oxide as we transition to the sidewall of the fins. Additionally, the gate oxide is very uniformly spaced below the source metal thanks to the self-aligned process. There is an asymmetry on the right and left side of the fins that we attribute to inaccurate setting of the deposition angle. In our first test runs, we were using an iPhone's level app to set the angle. We have since purchased a digital angle finder that is accurate to 0.1° and designed a 3-D printed jig for repeatable angle finder placement.

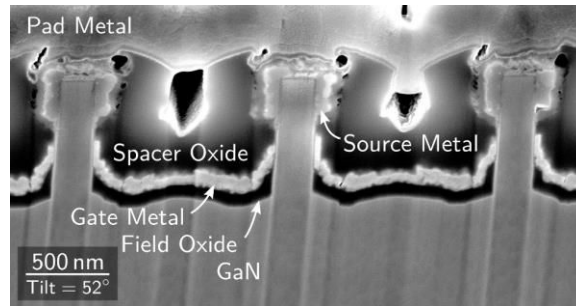


Figure 17. SEM cross-section of a vertical GaN finFET with our new process flow

As can likely be seen, the fabrication flow is much more repeatable, but designing the geometry of the fins, the thickness of the metals, and the angles for each deposition is tedious and difficult. Ideally, a robust process simulation software would greatly ease design efforts and allow for faster prototyping of different designs. We have experimented with both Silvaco's and Sentaurus's process simulation softwares (both of which are readily available at MIT), but have found them unable to reliably simulate angled depositions with shadowing without errors. We are currently in talks Coventor to use their SEMulator3D MEMS simulation software to aid in design since it claims to be far more robust with non-standard fabrication processes such as those used in MEMS fabrication.

In Fig. 21 we show the output characteristics of one of the first finFETs processed with our new techniques, and Fig. 22 shows the TLM data of the source and drain contacts. Two notes should be made that degrade performance: (1) during ohmic metal deposition, the Al crucible ran dry and burned a portion of the carbon crucible, which increases on-resistance as shown in Fig. 22, and (2) the probe pad deposition had poor adhesion and we had to strip the metal and redeposit, which was a harsh process that substantially reduced yield. Additionally, the test substrate was designed for high frequency devices with short gate lengths, so the significant short-channel effects and poor pinch-off are a result of the asymmetric 200 nm gate length.

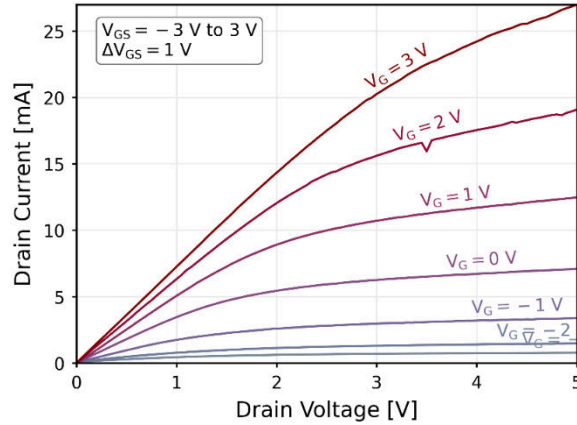


Figure 18. IV Characteristics of a vertical GaN finFET with our new process flow

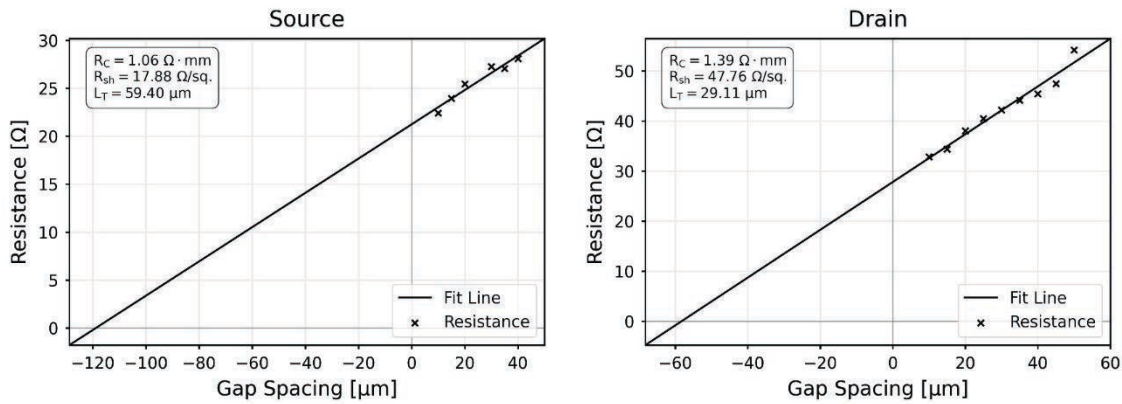


Figure 19. TLM data for the source and drain contacts after annealing with contaminated Al deposition

Edge Termination Study

In our previous report, we discussed our experiments to optimize the edge termination for the vertical finFETs. We had designed several Schottky diodes on bulk GaN substrates and GaN-on-QST[®] material as well as bulk-GaN finFETs. Applied Materials generously provided ion implantation of our samples with five varied conditions summarized in *Table 5. Ion implant conditions for edge termination*. Unfortunately, a processing error in an etch tool ruined the finFET samples, and our bulk GaN diodes exhibited very high reverse leakage – likely due to high defect density. Our only remaining samples are GaN-on-QST[®] diodes, which require substrate removal that is being developed in another program. This process is lengthy with low yield, so fabrication is still underway.

Table 5. Ion implant conditions for edge termination

Sample ID	Device Structure	Ion Species	Implant Condition
A	FinFET and Schottky diodes	N	150 keV, $5 \times 10^{13} \text{ cm}^{-2}$

B	Schottky diodes	Ar	150 keV, $1 \times 10^{13} \text{ cm}^{-2}$
C	Schottky diodes	N	150 keV, $5 \times 10^{15} \text{ cm}^{-2}$
D	Schottky diodes	N	50 keV, $5 \times 10^{13} \text{ cm}^{-2}$ 125 keV, $5 \times 10^{13} \text{ cm}^{-2}$ 200 keV, $5 \times 10^{13} \text{ cm}^{-2}$
E	Schottky diodes	Ar	50 keV, $5 \times 10^{13} \text{ cm}^{-2}$ 125 keV, $5 \times 10^{13} \text{ cm}^{-2}$ 200 keV, $5 \times 10^{13} \text{ cm}^{-2}$

Currently, we have redesigned our finFET mask to allow ion implantation of the three conditions in Fig. 23 where we compare the effects of no edge-termination, edge termination along the device periphery, and ion implantation between fins. SRIM simulations of standard nitrogen and argon implantation into GaN as well as into our mask material for the self-aligned between-fin implantation process are shown in Fig. 24 and 25. In the next quarter, we hope to go through another round of ion implantation (conditions A and B in Table Table 5) to compare nitrogen vs. argon implantation and our various edge-termination patterns in finFETs.

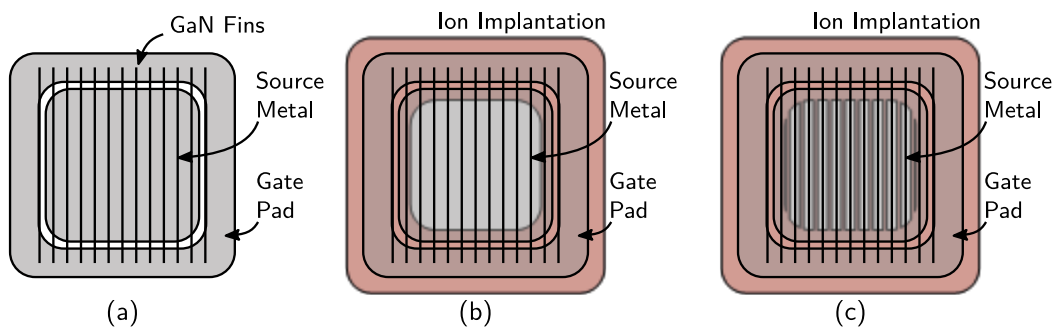


Figure 20. Implantation patterns for FinFETs with (a) no edge termination, (b) implantation along the device periphery (shown in red), and (c) implantation along the device periphery and self-aligned implantation between fins.

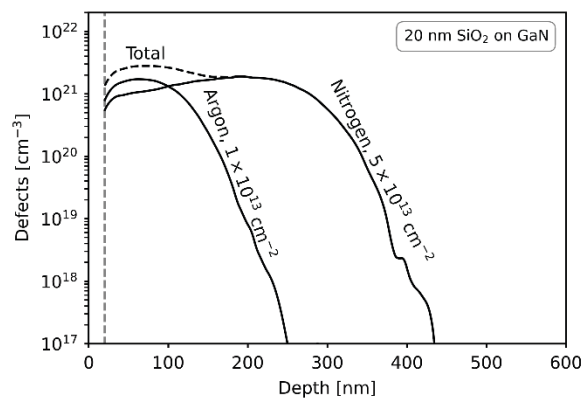


Figure 21. SRIM simulations of nitrogen and argon implantation at 150 keV into GaN with a 20 nm SiO_2 protection layer

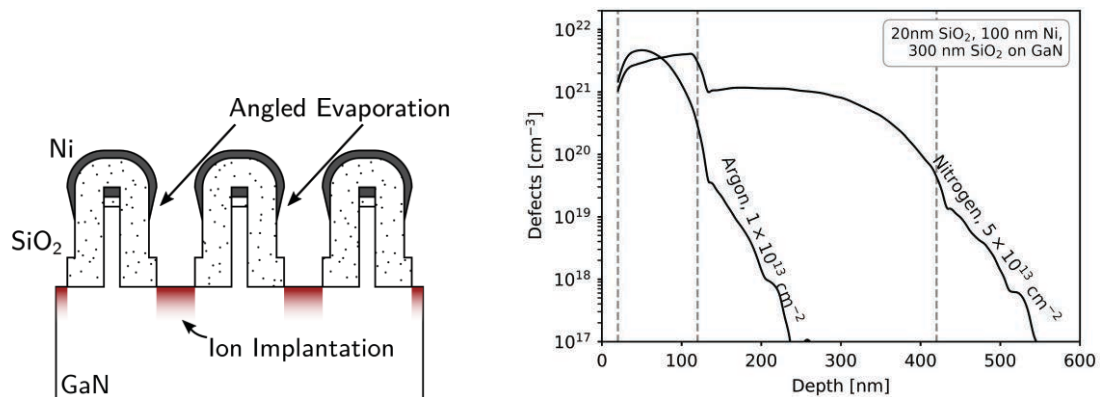


Figure 22. (Left) Schematic of finFETs with ion implantation between fins, and (right) SRIM simulations of the masked fins

Invention Disclosures

In the last few months, several exciting, new technologies have been created by our group at MIT. To date, we have submitted a technology disclosure to the MIT Technology Licensing Office to possibly patent our finFETs with ion implantation between fins to further control the electric field within the device.

Additionally, we are submitting disclosures for the superjunction based devices presented in the next section of this report, as well as for our new finFET design with the conformal, multi-metal annealed source.

NiO_x Superjunction FinFET

New Target Order

In our previous report, we presented the results in Fig. 26 showing an EDS overlay of our process for sputtered NiO liftoff. Unfortunately, we experienced adhesion issues and poor sidewall coverage of the NiO. These initial tests were performed using an old 2-inch NiO target that was provided by MIT for use in our sputterer for (less clean) experimental materials. After these results, we concluded that further deposition optimization is critical to the success of this project, and it made sense to purchase a new NiO target for our newer load-locked sputterer with a 3-inch target. This tool allows for deposition temperatures up to 400°C and high-power deposition for faster rates than the 1.2 nm/min. The improved deposition rates, minimal pumping time from the load-lock, and overall increased availability will drastically improve experiment turn-around in addition to the already improved cleanliness and repeatability.

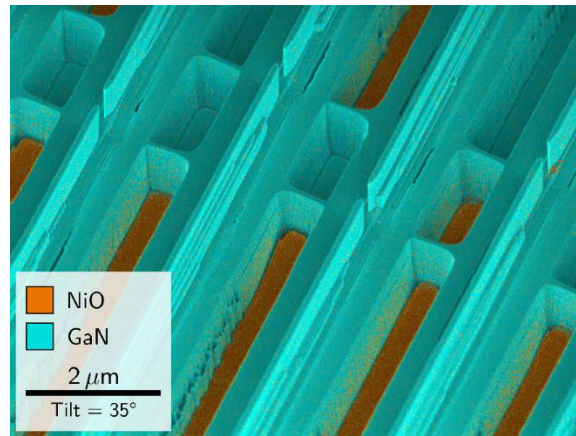


Figure 23. Titled SEM image with EDS overlay showing liftoff of sputtered NiO_x films within trenches patterned between fins

On October 12, 2021, a new NiO sputterer target with 99.995% purity was ordered through Kurt J. Lesker Company with an expected delivery date of mid-January. As of January 14, 2022, we were informed that the NiO target could not be properly made, so our order was cancelled. We were offered a 99.98% purity target, but are unsure of the effects of impurities on the resulting film. Currently, we are collecting quotes and purity information from other vendors and hope to place an order soon.

Summary:

- We have measured medium size vertical bulk GaN FinFET devices with current of ~ 1.3 A, excellent $I_{on}/I_{off} > 10^8$, and near zero threshold voltage. Devices are measured with significant series resistance due to problems with our probe station.
- Initial positive bias temperature instability measurements were performed.
- New wafer growth received from Lincoln Lab and UCSB for baseline finFETs, growth for super-junction devices underway.
- A new process flow is underway to allow for more uniform and repeatable field oxide patterning, a thicker, self-aligned gate metal, and annealed ohmic contacts.
- Most portions for our edge termination for ion implantation failed. Fabrication for the last set of implanted devices is underway. Plans for a next round of implantation to test various edge termination patterns is being planned.
- A new NiO target has been ordered for use in our more advanced sputterer, but was cancelled. New quotes are being collected and an order will be placed soon.
- Several technology disclosures have been filed or will be filed soon for consideration for patent application.

References

- [1] Y. Zhang, M. Sun, D. Piedra, J. Hu, Z. Liu, Y. Lin, *et al.*, "1200 V GaN vertical fin power field-effect transistors," *2017 IEEE International Electron Devices Meeting (IEDM)*, pp. 9.2.1-9.2.4, 2017.
- [2] Y. H. Zhang, M. Sun, J. Perozek, Z. H. Liu, A. Zubair, D. Piedra, *et al.*, "Large-Area 1.2-kV GaN Vertical Power FinFETs With a Record Switching Figure of Merit," *IEEE Electron Device Letters*, vol. 40, pp. 75-78, Jan 2019.
- [3] B. J. Baliga, *Gallium nitride and silicon carbide power devices*: World Scientific Publishing Company, 2016.
- [4] T. Palacios *et al.*, "GaN 2.0: Power FinFETs, Complementary Gate Drivers and Low-Cost Vertical Devices," *2021 33rd International Symposium on Power Semiconductor Devices and ICs (ISPSD)*, 2021, pp. 6-10

Report from UCSB

1.1.NH₃-MBE Maintenance and Growth Updates

In the previous quarter, we spend a significant portion of it bringing the NH₃-MBE system back to previous conditions. We then began a series of growth optimizations that concluded with the growth of the FinFET epitaxial structure.

During our past growths, we ran into several challenges during the process of growing the FinFET structure. As the FinFET required a relatively thick n-region (~9.5 μm), the growth rate required to grow needed to be higher. However, the faster growth rate used both degraded the morphology as well as increased the background doping of the drift region, both of which are detrimental to the FinFET as shown in Figure 24.

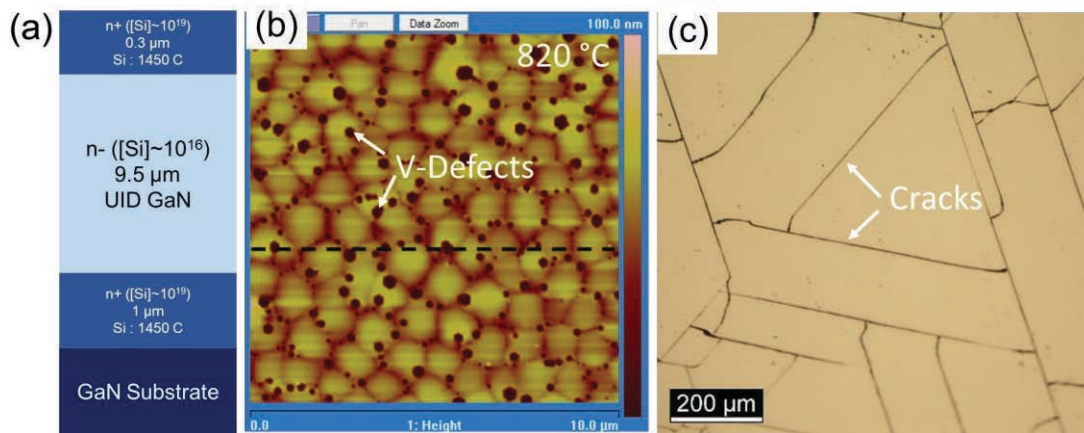


Figure 24: a) Schematic of epitaxial structure for the FinFET device, b) AFM scan c) Microscope picture of first growth attempt. Both show severely degraded morphology, with large cracks forming on the film.

Considering this, we did a growth condition search to optimize the growth of thick UID GaN drift regions. We first used Indium (In) as a surfactant during our growth as it has proven to be effective at improving surface morphology for *p*-GaN in the pastⁱ. At these high growth rates, we also needed to adjust our V-III ratio to ensure we are in a proper growth regimeⁱⁱ. As we had recently opened our chamber, we needed to do a short growth condition search to obtain our previously found optimal condition. This was done by growing a series of test structures similar to the final FinFET structure with a thinner (2 μm) drift region. We would then conduct AFM and SIMS measurements to characterize the quality of the films.

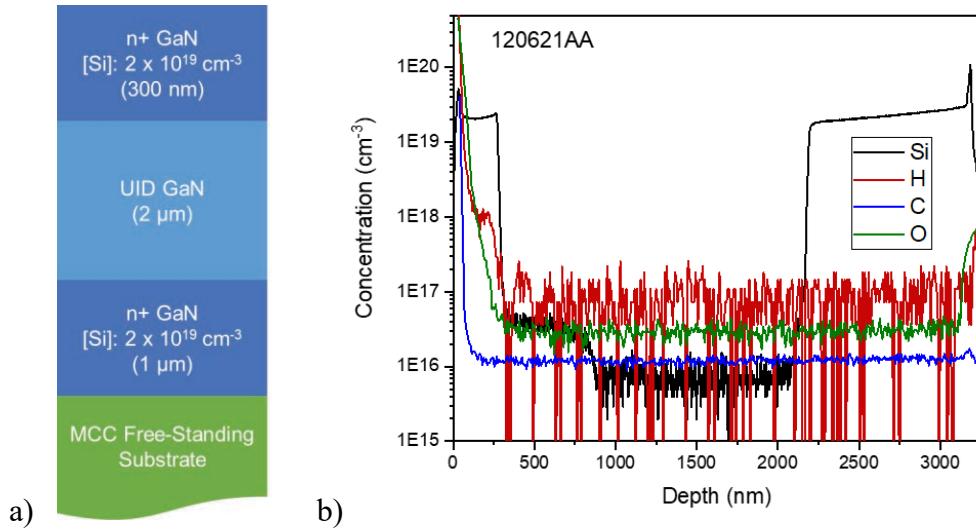


Figure 25: a) Schematic of the FinFET test structure. b) SIMS data for the FinFET test structure

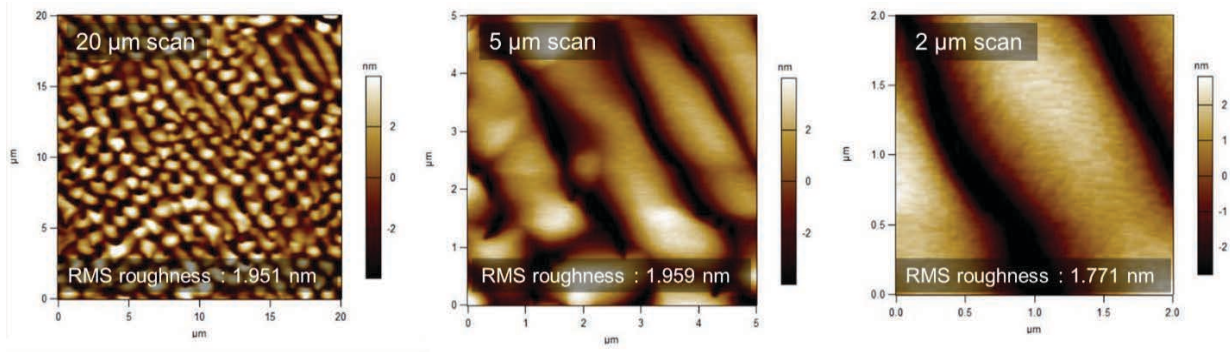


Figure 26: AFM scans labeled with the corresponding scan sizes and RMS roughnesses

It was found that with the right growth conditions, we were able to obtain background Si concentrations of approximately $8 \times 10^{15} \text{ cm}^{-3}$ as seen on Figure 25. With the same conditions, we were also able to reduce the pit density and improve the surface morphology. This structure was grown on Mitsubishi Chemical Corporation (MCC) free-standing GaN templates at $850 \text{ }^\circ\text{C}$ with an ammonia flow rate of 500 sccm. The Ga beam equivalent pressures (BEP) was set at 6.94×10^{-7} Torr with the In surfactant BEP being set at 4.95×10^{-8} Torr.

With these conditions, we then grew the final epitaxial structure to be processed into FinFETs. The structure consists of a 2 μm -thick Si-doped region ($[\text{Si}]: 2 \times 10^{19} \text{ cm}^{-3}$) followed by a 9.5 μm -thick UID GaN drift region ($[\text{Si}]: 8 \times 10^{15} \text{ cm}^{-3}$) before being capped by a 300 nm-thick Si-doped region ($[\text{Si}]: 2 \times 10^{19} \text{ cm}^{-3}$). The schematic of this structure can be seen on Figure 24 a). Following the growth, we characterized the film quality using the microscope as well as conducted AFM scans.

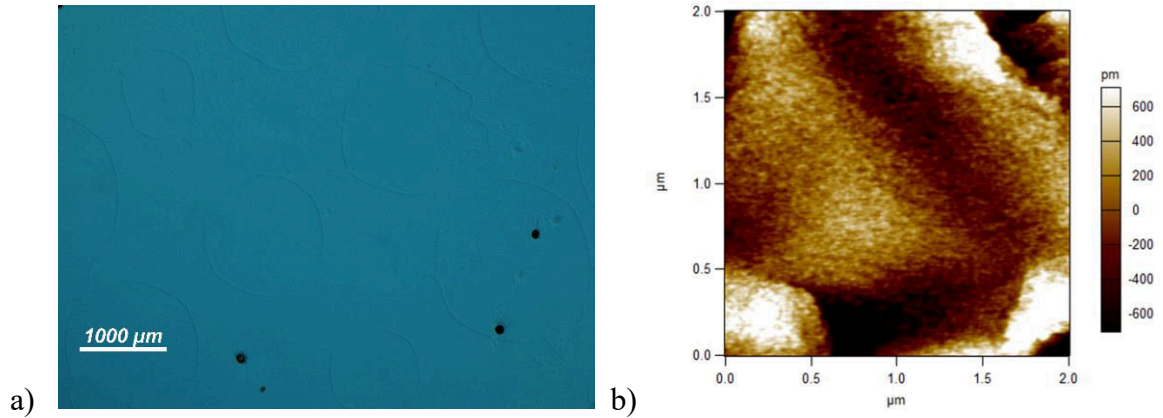


Figure 27 : a) Microscope images and b) AFM scans of the final FinFET structure

While the morphology is slightly degraded when compared to the test structure, we were still able to reduce the V-defect density and improve the surface morphology when compared to the first generation FinFET structure shown in Figure 24. Although the surface was found to be free of cracks, there were circular patterns emerging on the surface. Further studies are required to determine the origin of these circles. That being said, the regions inside and outside the circles were found to be similar in morphology when we did AFM scans on them. Whilst there were regions that still had some V-defects, there are many regions that were free of them as shown on Figure 27b). The sample was then shipped to MIT to be processed into FinFET devices.

1.2.Continuation of Oxygen Radical Treatment

In this past quarter, the experiments to remove unintentional Si impurities at artificial regrowth interfaces has continued. The formation of either SiO or SiO₂ on a pristine Si surface has been extensively studied.^{iii,iv} It has been noted that the temperature of the surface and the pressure of oxygen in the chamber determines the formation of active (SiO) or passive (SiO₂) surfaces. The relevant temperature and pressure regimes can be seen in Figure 28.

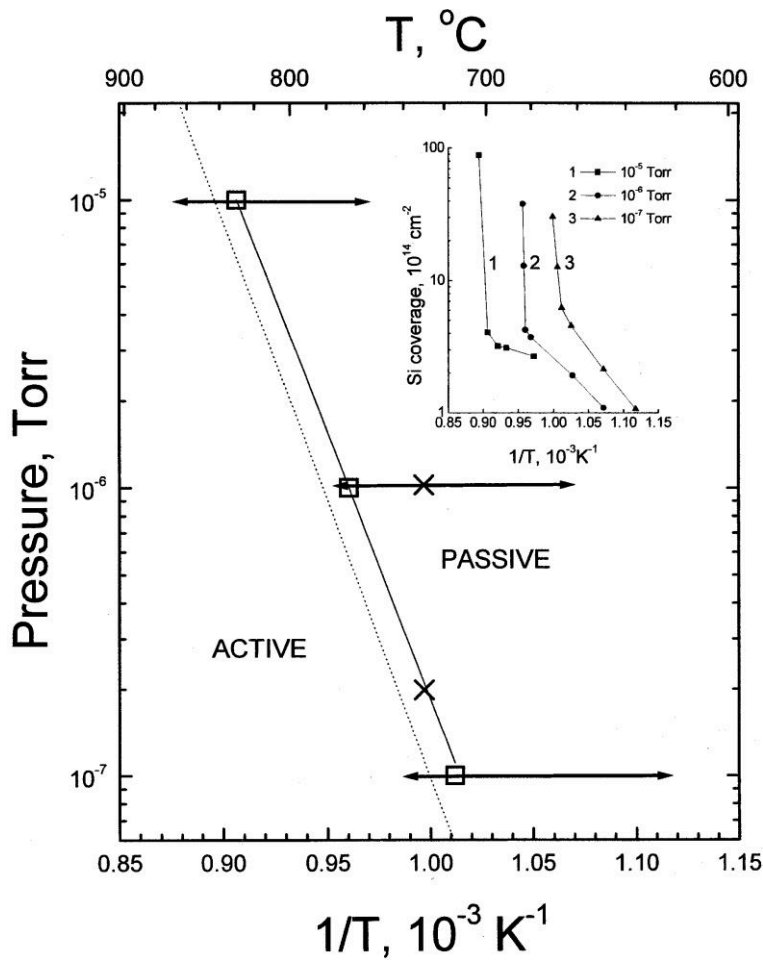


Figure 28: Temperature and pressure regimens for the active (SiO) or passive (SiO₂) oxidation of Si surfaces. Note that increasing the temperature, or decreasing the pressure, leads to active oxidation.^v

Recall that the surface treatment experiments utilize artificially created regrowth interfaces separated by GaN buffer layers. These artificial regrowth interfaces are created by intentionally dosing the surface of the sample with Si. This mimics a regrowth surface after either Ga polishing or GaN thermal decomposition cleaning where the oxygen and carbon are removed from the surface, but the Si remains.^{vi} The resulting structure can be treated in the *in situ* gas phase treatment chamber attached to the plasma assisted MBE (PAMBE) system using the equipped oxygen beam source (OBS). This process can be repeated multiple times and capped to create a stack for examination in SIMS. An example process flow can be seen in Figure 29 below.

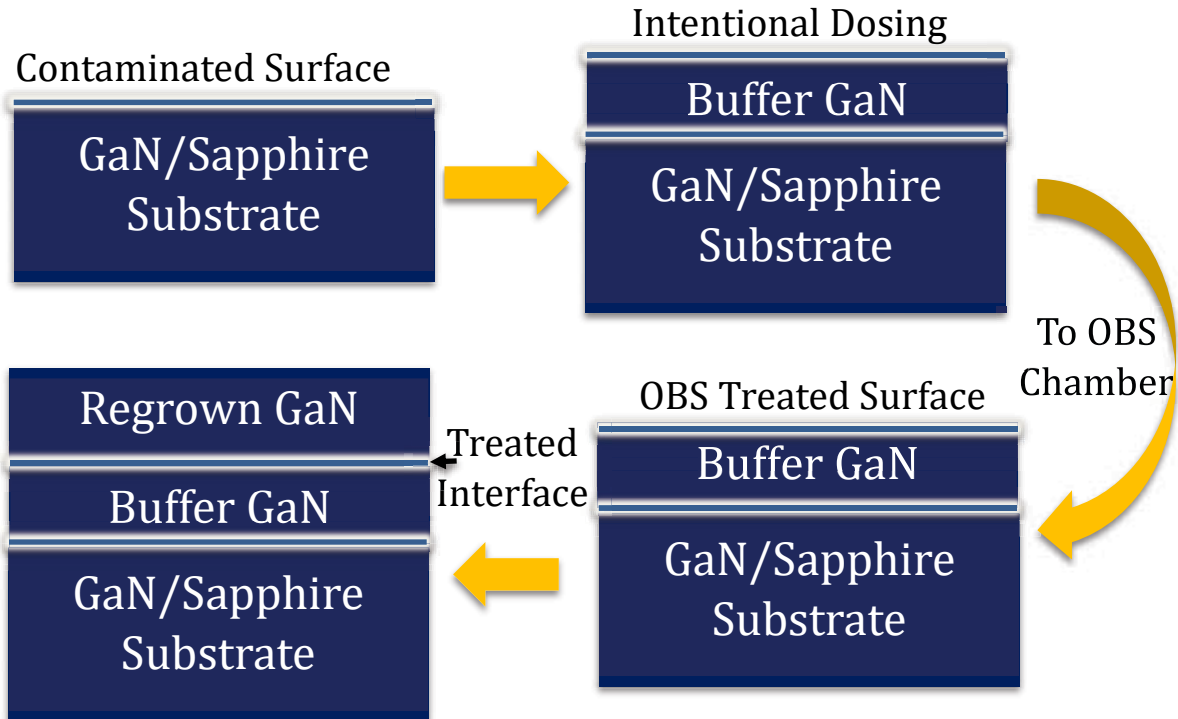


Figure 29: Example process flow for a surface treatment sample.

In the previous quarters, the temperature of the substrate heater was examined up to 775 °C at a pressure of 1×10^{-7} Torr, with no change to the Si concentration at the artificial interface. This suggests that the actual surface temperature may be lower than what is recorded using the heater thermocouple. So, the temperature was further increased, to the maximum of the current calibration on the heater (800 °C). The resulting Si SIMS profile for this sample can be seen in Figure 30 below. This particular sample includes an In polishing step as some results from the NH₃-MBE system suggested a decrease in Si incorporation when growing GaN films with an In surfactant. As such, an In polishing step was explored to see if the In may facilitate Si removal.

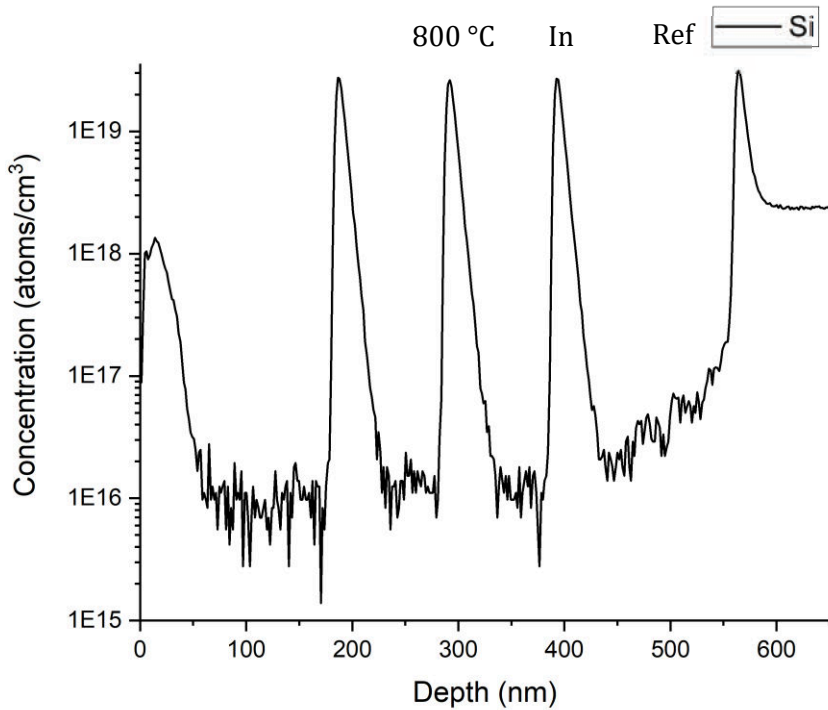


Figure 30: Artificial regrowth interfaces Si profile. This sample increases the heater temperature to 800 °C and includes an In polishing interface.

The Si interfacial concentration can be obtained through numerical integration of each of these “spikes” and is reported in Table 6 below.

Table 6: Si interfacial concentrations for sample in Figure 30.

Treatment	Sheet Concentration (cm ⁻²)
800 °C	2.70×10 ¹³
In Polish	2.64×10 ¹³
Ref	2.56×10 ¹³

The 800 °C treatment maxed out the current calibration for the sample heater in the surface treatment chamber. As such, other avenues were explored prior to updating the calibration to increase the temperature of the heater. As the pressure of the system is limited by the components when at temperature, it cannot be decreased much below the 1×10⁻⁷ Torr value. As mentioned prior, increasing the temperature is unlikely to facilitate active oxidation. So, the OBS operating temperature was examined. The filament temperature of the OBS determines the cracking efficiency of the oxygen gas, as show in Figure 31 below.

Measured degree of dissociation of the OBS and derived total atomic flux and flux density at distance of 100mm from the cell:

O ₂ Gas flow [sccm]	Cell temperature [°C]	Dissociation [%]	Total flux [O-atoms/s]	Flux density [O-atoms/cm ² s]
0.0016	1880	22.8	3.3*10 ¹⁴	1.1*10 ¹³
	1760	17.3	2.5*10 ¹⁴	8.3*10 ¹²
	1630	10.0	1.4*10 ¹⁴	4.7*10 ¹²
0.02	1880	19.0	3.4*10 ¹⁵	1.1*10 ¹⁴
	1760	10.5	1.9*10 ¹⁵	6.3*10 ¹³
	1630	4.8	8.6*10 ¹⁴	2.9*10 ¹³
0.1	1870	15.7	1.4*10 ¹⁶	4.6*10 ¹⁴
	1740	7.3	6.6*10 ¹⁵	2.2*10 ¹⁴
	1610	3.0	2.7*10 ¹⁵	9.0*10 ¹³
0.3	1860	9.6	2.7*10 ¹⁶	9.0*10 ¹⁴

Typical applications for the OBS are low temperature surface cleaning, surface oxidation and low growth rate oxide deposition. A flux density of about 1×10^{15} atoms/cm²s corresponds to a typical growth rate of 1ML/s.

OBS 40-2206530

page 35 of 40

Figure 31: Oxygen dissociation percentage for the OBS source based on gas flow and filament temperature from the OBS user manual.

For all the previous conditions, the OBS temperature was fixed at 1700 °C, which is the minimum recommended value. As such, it is possible to increase the temperature of the OBS to increase the percentage of atomic oxygen. For this set, the heater temperature was fixed at 800 °C while the OBS temperature was adjusted. The obtained Si concentration profile can be seen in Figure 32 below.

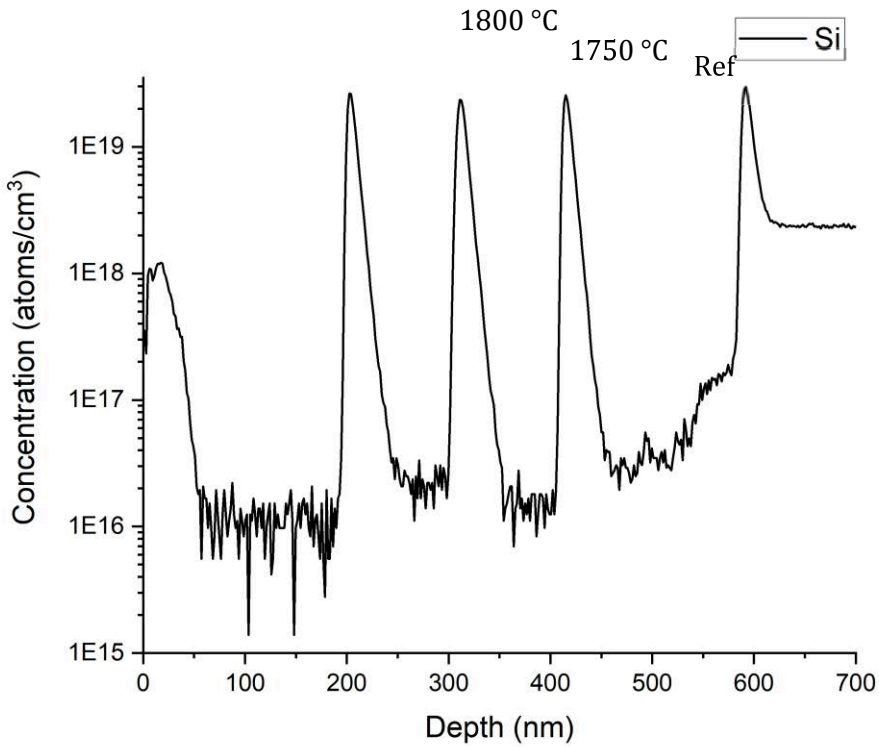


Figure 32: OBS filament series Si SIMS profile.

The Si interfacial concentrations obtained through numerical integration can be seen in Table 7 below.

Table 7: Si sheet concentrations for the profile in Figure 32

Treatment	Sheet Concentration (cm ⁻²)
1800 °C	2.63×10^{13}
1750 °C	2.56×10^{13}
Ref	2.54×10^{13}

In both sets of samples, the interfacial Si concentrations remain unchanged from the reference values, suggesting that the current conditions fail to remove the Si. Continued work is scheduled to further increase the heater temperature (after recalibration at higher current values for the heater) as well as reducing the overall pressure in the chamber when the components are at high temperature. A new turbomolecular pump with a much higher throughput is currently being installed on the system, which should dramatically reduce the operating pressures. If, however,

these options do not aid in removing the Si, other gas phase treatments can be explored including: hydrogen radicals and more typical Si etchants like XeF₂.^{vii}

ⁱ E.C.H. Kyle, S.W. Kaun, E.C. Young, and J.S. Speck, *Appl. Phys. Lett.* **106**, 222103 (2015).

ⁱⁱ A.L. Corrion, F. Wu, and J.S. Speck, *Journal of Applied Physics* **112**, 054903 (2012).

ⁱⁱⁱ M. P. D'Evelyn, M. M. Nelson, and T. Engel. *Surf. Sci.* **186**, 75-114, (1987).

^{iv} Y. Enta, S. Osanai, T. Ogasawara. *Surf. Sci.* **656**, 96-100 (2017).

^v D. Starodub *et. al.* *Surf. Rev. and Lett.* Vol. 6, No 1., 45-52 (1999).

^{vi} G. Koblmüller *et. al.* *J. Appl. Phys.*, **107**, 043527, (2010).

^{vii} D. E. Ibbotson *et. al.* *Appl. Phys. Lett.* **44**, 1129 (1984).

DE-AR0000874 : University of Missouri - Kwon
Q1 of FY 2022: October 1, 2021 - December 31, 2021

Schedule - Updates

WBS	Task Name	Mile-stone	Baseline Start	Baseline End	Actual Start	Actual End	% Comp
1	Development of work plan		9/20/2017	12/19/2017			100%
└ M1.1	Q1: Work plan finalized	▼	12/19/2017	12/19/2017			100%
2	Neutron activation of Ge dopants in GaN wafers		9/20/2017	6/19/2018	9/20/2017	4/30/2019	100%
└ 2.1	Establish irradiation protocol		9/20/2017	12/19/2017	9/20/2017	12/31/2017	100%
└ 2.2	Scoping experiments		9/20/2017	6/19/2018	11/12/2017	6/30/2018	100%
└ 2.3	C14 reduction scoping experiments		3/20/2019	12/19/2019	3/20/2019	12/19/2019	100%
└ 2.4	PhotonuclearScopingexperiments		3/20/2019	12/19/2020	10/17/2019		70%
└ 2.5	Development of masks for transmutation doping		9/20/2019	6/19/2020	10/2/2019		50%
└ 2.6	Masking Scoping Experiments		12/20/2019	9/19/2020	12/20/2019		30%
└ 2.7	Doping of mono-isotope GaN		9/20/2019	12/19/2020	8/15/2019		25%
└ M2.1.1	Q1: Establish wafer supply chain	▼	12/19/2017	12/19/2017	9/20/2017	11/30/2017	100%
└ M2.2.1	Q3: Consistent doping concentration	▼	6/19/2018	6/19/2018	1/2/2018	6/30/2018	100%
└ M2.3.1	Q9: Consistent doping concentration	▼	12/19/2019	12/19/2019	8/20/2019	12/19/2019	100%
└ M2.4.1	Q10: Consistent doping concentration	▼	6/19/2020	6/19/2020	6/8/2020		80%
└ M2.5.1	Q10: Masking material for transmutation doping.	▼	3/19/2020	3/19/2020	6/8/2020		75%
└ M2.6.1	Q12: Linear selective doped GaN	▼	3/19/2020	9/19/2020	10/8/2019		75%
3	Characterization of GaN wafers doped by neutron transmutation		12/20/2017	12/19/2020	12/11/2017	4/30/2019	100%
└ 3.1	Impurity analysis		12/20/2017	3/19/2020	1/8/2018	12/31/2018	100%
└ 3.2	Crystallinity analysis		12/20/2017	6/19/2020	2/6/2018	12/31/2018	100%
└ 3.3	Electrical analysis		12/20/2017	12/19/2020	12/11/2017	6/30/2019	100%
└ 3.4	Electrical analysis of selective doping		12/20/2019	12/19/2020	10/8/2019		50%
└ M3.3.1	Q4: Consistent carrier concentration	▼	9/19/2018	9/19/2018			100%
└ M3.3.2	Q10: Consistent n-type carrier concentration	▼	3/19/2020	3/19/2020	10/2/2019	6/30/2020	100%
└ M3.3.3	Q11: Consistent p-type behavior	▼	6/19/2020	6/19/2020	6/1/2020		60%
└ M3.4.1	Q13: Consistent vertical doping	▼	12/19/2020	12/19/2020	6/1/2020		90%
4	Technology To Market		9/20/2017	12/19/2020	10/2/2017	6/30/2019	100%
└ 4.1	Invention disclosures and patent applications		9/20/2017	12/19/2020	10/2/2017	6/30/2019	100%
└ 4.2	Publications and Presentations		3/20/2018	12/19/2020		6/30/2019	90%

DE-AR0000874 : University of Missouri - Kwon
 Q1 of FY 2022: October 1, 2021 - December 31, 2021

WBS	Task Name	Mile- stone	Baseline Start	Baseline End	Actual Start	Actual End	% Comp
└ M4.1.1	Q1: Background IP report	▼	12/19/2017	12/19/2017	10/2/2017	12/31/2017	100%
└ M4.2.1	Q4: Presentation / Publication	▼	9/19/2018	9/19/2018	3/13/2018	6/30/2019	90%
└ M4.1.2	Q4: IP Update	▼	9/19/2018	9/19/2018		6/30/2019	100%
└ M4.1.3	Q13: IP Update	▼	12/19/2020	12/19/2020			70%
└ M4.2.1	Q4: Presentation/Publication	▼	9/19/2018	9/19/2018			100%
└ M4.2.2	Q13:Presentation /Publication	▼	12/19/2020	12/19/2020			40%
5	Collaboration Work		9/20/2019	12/19/2020	9/20/2019		60%
└ 5.1	Epi-layer growthfor a drift layer		3/20/2020	9/19/2020	2/20/2020		70%
└ 5.2	Doping processfor a drift layer		3/20/2020	9/19/2020	3/12/2020		70%
└ 5.3	Vertical GaNdevice creation		3/20/2020	12/19/2020			30%
└ 5.4	Determineirradiationparameters forcarbon behaviorstudy		6/20/2019	3/19/2020			70%
└ 5.5	Irradiation ofcarbon behaviorstudy		9/20/2019	3/19/2020	9/20/2019		80%
└ 5.6	ElectricalCharacterizationof the carbonbehavior study		9/20/2019	6/19/2020	9/20/2019		60%
└ M5.2.1	Q13: Creation ofdoped layers forFinFET Devices	▼	12/19/2020	12/19/2020			10%
└ M5.6.1	Q10:Characterization of Cdoping in GaN	▼	3/19/2020	3/19/2020	1/3/2020		85%

Additional Performance Updates

A) ISSUES, RISKS, AND MITIGATION

N/A

B) CHANGES IN APPROACH

N/A

C) CHANGES IN PROJECT PERSONNEL

N/A

Technology To Market (T2M)

A. PUBLICATIONS

N/A

B. OTHER PROJECT OUTPUT

N/A

C. FOLLOW-ON FUNDING

N/A

Administrative and Legal Updates

DISCLOSURES

N/A

DE-AR0000874 : University of Missouri - Kwon
Q1 of FY 2022: October 1, 2021 - December 31, 2021

Cost Updates - LEAD: University of Missouri (DE-AR0000874)

High quality GaN FETs through transmutation doping and low temperature processing

ARPA-E RECORDS ONLY (invoices edited by performer are highlighted)

Invoice #	Date	Total	Federal Share	Performer Share	Shortpays	TT&O	Personnel	Fringe Benefits	Travel	Equipment	Supplies	Contractual	Construction	Other	Indirect
AR0000874-GM00229819	2/27/2018	\$40,310.60	\$40,310.60	\$0.00	\$0.00	\$0.00	\$8,509.26	\$1,309.43	\$1,528.27	\$0.00	\$14,659.84	\$0.00	\$0.00	\$0.00	\$14,303.80
AR0000874-GM00231274	3/27/2018	\$21,222.09	\$5,722.09	\$15,500.00	(\$263.50)	\$0.00	\$2,618.26	\$332.31	\$0.00	\$0.00	\$0.00	\$0.00	\$0.00	\$16,431.45	\$1,840.07
AR0000874-GM00232388	4/30/2018	\$9,422.99	\$9,422.99	\$0.00	\$0.00	\$0.00	\$3,168.69	\$374.41	\$0.00	\$0.00	\$374.91	\$0.00	\$0.00	\$2,161.32	\$3,343.66
AR0000874-GM00233996	6/7/2018	\$8,724.82	\$8,724.82	\$0.00	\$0.00	\$2,085.77	\$3,168.71	\$374.42	\$0.00	\$0.00	\$0.00	\$0.00	\$0.00	\$2,085.77	\$3,095.92
AR0000874-GM00235448	7/20/2018	\$9,089.15	\$9,089.15	\$0.00	\$0.00	\$1,937.57	\$3,127.61	\$425.93	\$0.00	\$0.00	\$372.86	\$0.00	\$0.00	\$1,937.57	\$3,225.18
AR0000874-GM00236640	8/14/2018	\$45,587.09	\$45,587.09	\$0.00	\$0.00	\$48.00	\$16,502.64	\$4,881.20	\$0.00	\$10,282.15	\$0.00	\$0.00	\$0.00	\$2,160.00	\$11,761.10
AR0000874-GM00237640	8/29/2018	\$34,932.69	\$34,932.69	\$0.00	\$0.00	\$0.00	\$2,381.86	\$299.67	\$0.00	\$0.00	\$19,855.69	\$0.00	\$0.00	\$0.00	\$12,395.47
AR0000874-GM00238852	10/8/2018	\$6,732.34	\$6,732.34	\$0.00	\$0.00	\$0.00	\$3,230.04	\$385.75	\$0.00	\$0.00	\$727.65	\$0.00	\$0.00	\$0.00	\$2,388.90
AR0000874-GM00240232	10/22/2018	\$5,755.26	\$5,755.26	\$0.00	(\$168.95)	\$0.00	\$2,386.43	\$143.71	\$1,149.17	\$0.00	(\$198.50)	\$0.00	\$0.00	\$360.00	\$1,914.45
AR0000874-GM00243994	1/31/2019	\$43,861.54	\$43,861.54	\$0.00	\$0.00	\$0.00	\$10,112.04	\$701.38	\$1,121.71	\$0.00	\$16,222.20	\$0.00	\$0.00	\$140.42	\$15,563.79
AR0000874-GM00244762	2/26/2019	\$6,964.77	\$6,964.77	\$0.00	\$0.00	\$0.00	\$2,992.78	\$190.10	\$0.00	\$0.00	\$1,310.51	\$0.00	\$0.00	\$0.00	\$2,471.38
AR0000874-GM00246042	3/28/2019	\$27,134.98	\$27,134.98	\$0.00	\$0.00	\$0.00	\$2,993.04	\$190.19	\$0.00	\$0.00	\$12,663.07	\$0.00	\$0.00	\$2,573.20	\$8,715.48
AR0000874-GM00248162	5/3/2019	\$4,934.46	\$4,934.46	\$0.00	\$0.00	\$0.00	\$2,993.27	\$190.25	\$0.00	\$0.00	\$0.00	\$0.00	\$0.00	\$0.00	\$1,750.94
AR0000874-GM00251770	8/27/2019	\$62,855.00	\$62,855.00	\$0.00	\$0.00	\$1,090.00	\$26,984.35	\$8,264.43	\$0.00	\$0.00	\$1,431.81	\$0.00	\$0.00	\$4,784.07	\$21,390.34
AR0000874-00057744NOV2020	12/21/2020	\$838,956.61	\$786,102.23	\$52,854.38	(\$344.10)	\$3,992.55	\$116,872.38	\$33,492.03	\$1,214.35	\$100,400.00	\$62,739.47	\$346,468.11	\$0.00	\$27,118.99	\$150,651.28
AR0000874-00057744DEC2020	2/1/2021	\$41,705.73	\$30,748.04	\$10,957.69	\$0.00	\$0.00	\$7,726.04	\$2,479.27	\$0.00	\$0.00	\$141.08	\$25,668.83	\$0.00	\$0.00	\$5,690.51
AR0000874-00057744FEB2021	3/25/2021	\$120,423.10	\$117,245.21	\$3,177.89	(\$263.50)	\$0.00	\$8,120.20	\$2,500.56	\$0.00	\$0.00	\$3,216.97	\$97,797.85	\$0.00	\$759.20	\$8,028.32

DE-AR0000874 : University of Missouri - Kwon
 Q1 of FY 2022: October 1, 2021 - December 31, 2021

ARPA-E RECORDS ONLY (invoices edited by performer are highlighted)

Invoice #	Date	Total	Federal Share	Performer Share	Shortpays	TT&O	Personnel	Fringe Benefits	Travel	Equipment	Supplies	Contractual	Construction	Other	Indirect
Total:		\$1,328,613.22	\$1,246,123.26	\$82,489.96	(\$1,040.05)	\$9,153.89	\$223,887.60	\$56,535.04	\$5,013.50	\$110,682.15	\$133,517.56	\$469,934.79	\$0.00	\$60,511.99	\$268,530.59
% Expended in Budget Category:		57.67%	57.75%	56.54%		12.35%	82.97%	80.58%	151.92%	55.27%	52.66%	51.75%	0.00%	33.94%	63.89%
Remaining:		\$975,236.78	\$911,825.74	\$63,411.04		\$64,983.08	\$45,957.40	\$13,625.96	(\$1,713.50)	\$89,578.85	\$120,049.44	\$438,141.21	\$0.00	\$117,804.01	\$151,793.41

Overall Proposed Cost Share: 6.33 % Invoiced Cost Share to Date: 6.21 % Proposed TT&O to Federal Share: 3.44 % Actual TT&O to Federal Share: 0.73 %

Agree that the information provided is accurate and correct: Yes No

DE-AR0000874 : University of Missouri - Kwon
Q1 of FY 2022: October 1, 2021 - December 31, 2021

Cost Updates - SUB: Argonne National Laboratory (18/CJ000/01/05)

High Quality GaN FETs through transmutation doping and low temperature processing

N/A

Certification of Compliance

I certify that I have the authority to make the following certification and to submit this Research Performance Progress Report on behalf of the Prime Recipient. On behalf of the Prime Recipient, I further certify that the information provided in this Research Performance Progress Report is accurate and complete as of the date shown below. I understand that false statements or misrepresentations may result in civil and/or criminal penalties under 18 U.S.C. § 1001.

Signature: Jae W Kwon

Submitted by: Prof. Jae Kwon (kwonj@missouri.edu), University of Missouri

Submitted Date: 2/1/2022 2:35:36 AM